SINGLE PHOTON AVALANCHE DIODE (SPAD) ARRAY DETECTORS FOR LUMINESCENCE-BASED BIOMEDICAL APPLICATIONS

Von der Fakultät für Ingenieurwissenschaften

Abteilung Elektrotechnik und Informationstechnik

der Universität Duisburg-Essen

zur Erlangung des akademischen Grades

Doktor der Ingenieurwissenschaft

genehmigte Dissertation

von

Alexander Netaev

aus

Bischkek, Kirgisistan

Gutachter: Prof. Dr.-Ing. Karsten Seidl

Gutachter: Prof. Dr. rer. nat. Sven Ingebrandt

Tag der mündlichen Prüfung: 06.12.2022

Zusammenfassung

Single photon avalanche diode (SPAD)-Array-Detektoren mit ihrer Einzelphotonen-Empfindlichkeit und Pikosekunden-Zeitauflösung eignen sich besonders gut für den Nachweis der geringen Photonenanzahl, die bei einer Chemilumineszenzmessung erzeugt werden, sowie für die Bestimmung der Fluoreszenzlebensdauer, die typischerweise im Nanosekundenbereich liegt. In dieser Dissertation wurden die Schlüsselparameter untersucht, die SPAD-Array-Detektoren aufweisen müssen, um für Lumineszenz-basierte biomedizinische Anwendungen eingesetzt werden zu können. Zwei Anwendungsgebiete wurden dabei untersucht, zum einen der Nachweis von Pathogenen in einem kompakten Chemilumineszenz-basierten Messsystem und zum anderen die Fluorophor-Differenzierung mittels Fluoreszenzlebensdauer in einem Durchflusszytometrie-Messsystem.

Anhand von experimentellen Messungen an zwei zu diesem Zweck entwickelten Messaufbauten und mit Hilfe geeigneter Monte Carlo-Simulationen war es möglich SARS-CoV-2 RNA und ssDNA in verschiedenen Konzentrationen nachzuweisen. Dabei konnte gezeigt werden, dass die von der WHO als akzeptabel definierte Nachweisgrenze (10^6 Kopien/ml) mit dem Aufbau und einem geeigneten Assay von $1.8 \cdot 10^5$ Kopien/ml theoretisch erreicht werden kann. Auch wurden die Hauptfaktoren bestimmt, um die Nachweisgrenze weiter zu senken. Mit dem zweiten Messaufbau wurde im nächsten Schritt, die Genauigkeit und Präzision der Fluoreszenz-Lebensdauer-Bestimmung und der Einsatz zur Fluorophor-Differenzierung untersucht. Dazu wurde die Abhängigkeit der Genauigkeit und Präzision der bestimmten Fluoreszenzlebensdauer von der Photonenzahl und der Detektionsrate ermittelt und die erforderlichen Parameter des SPAD-Array-Detektors, wie Pixelzahl und Zeitauflösung, bestimmt. Der auftretende Pile-Up-Effekt, der die Messdauer begrenzt und mit zunehmender Pixelzahl abnimmt, kann schon mit 30 Pixeln verringert werden, sodass die Fluoreszenzlebensdauer bereits in Mikrosekunden-Messdauern bestimmt werden kann.

In Fällen wie beispielsweise der Differenzierung und Charakterisierung von Pathogenen, ist eine Differenzierung einer Vielzahl von Fluorophoren in einem Gemisch

notwendig. Hierbei bietet die Differenzierung durch fraktionierte Beiträge mittels Fluoreszenzlebensdauer einen zusätzlichen Multiplexfaktor, auch wenn das Limit der spektral differenzierbaren Fluorophoren erreicht ist. Dabei konnte gezeigt werden, dass die Anzahl der differenzierbaren Fluorophore hauptsächlich durch die Differenz zwischen den vorliegenden Fluoreszenz-Lebensdauern limitiert ist, die bei zwei Fluorophoren mindestens $0.5\,\mathrm{ns}$ betragen muss. Durch den Einsatz künstlicher neuronaler Netze konnte die Genauigkeit und Präzision der ermittelten fraktionellen Beiträge im Vergleich zur üblich verwendeten LS-Fit-Methode weiter erhöht werden. Zur Verifizierung dieser Methode für den Einsatz in der Durchflusszytometrie wurden einzelne fluoreszierende Mikropartikeln trotz eines hohen Hintergrund-Fluoreszenz-Anteils von etwa $50\,\%$ bei einer Fluoreszenzlebensdauerdifferenz von $0.7\,\mathrm{ns}$ differenziert. Aus diesen Messergebnissen lässt sich schlussfolgern, dass es theoretisch möglich ist, etwa 5000 Zellen oder Partikel pro Sekunde mit dem hier verwendeten SPAD-Array-Detektor zu differenzieren. Für die beiden untersuchten Anwendungen wurden in dieser Dissertation erfolgreich die Anforderungen an den Messaufbau und den SPAD-Array-Detektor ermittelt, was die Entwicklung von maßgeschneiderten SPAD-Array-Detektoren ermöglicht.

Abstract

Single photon avalanche diode (SPAD) array detectors, with their single photon sensitivity and picosecond time resolution, are particularly well suited for detecting the small number of photons produced in a chemiluminescence measurement and for determining fluorescence lifetime, which is typically in the nanosecond range. In this dissertation, the key parameters that SPAD array detectors needs to have in order to be used for luminescence-based biomedical applications were investigated. Two application areas were investigated, one being the detection of pathogens in a compact chemiluminescence-based measurement system and the other being fluorophore differentiation using fluorescence lifetime in a flow cytometry measurement system.

Using experimental measurements on two measurement setups developed for this purpose and suitable Monte Carlo simulations enabled the detection of SARS-CoV-2 RNA and ssDNA at different concentrations. It was shown that the detection limit defined as acceptable by the WHO (10^6 copies/ml) can theoretically be achieved with this setup and a suitable assay of $1.8 \cdot 10^5$ copies/ml. The main factors were also determined to further lower the detection limit. Using the second measurement setup, the next step was to investigate the accuracy and precision of fluorescence lifetime determination and its use for fluorophore differentiation. For this purpose, the relation of the accuracy and precision of the determined fluorescence lifetime to the photon counts and the detection rate were investigated, and the required parameters of the SPAD array detector, such as pixel count and time resolution, were determined. The pile-up effect, which limits measurement duration and decreases with higher pixel number, can be reduced with as few as 30 pixels, so that the fluorescence lifetime can already be determined in microsecond measurement durations.

In cases such as pathogen differentiation and characterization, differentiation of a large number of fluorophores in a mixture is necessary. Here, differentiation by fractional contributions using fluorescence lifetimes provides an additional multiplexing factor, when the limit of spectrally differentiable fluorophores is reached. It

was shown that the number of differentiable fluorophores is mainly limited by the difference between the fluorescence lifetimes present, which must be at least $0.5\ \mathrm{ns}$ for two fluorophores. By using artificial neural networks, the accuracy and precision of the determined fractional contributions could be further increased compared to the conventionally used LS-Fit method. To verify this method for use in flow cytometry, single fluorescent microparticles were differentiated despite high background fluorescence fraction of about $50\ \%$ at a fluorescence lifetimes difference of $0.7\ \mathrm{ns}$. From these measurement results it can be concluded that it is theoretically possible to differentiate about 5000 cells or particles per second with the SPAD array detector used here. The requirements for the measurement setup and the SPAD array detector were successfully determined for both applications investigated in this dissertation, enabling the development of customized SPAD array detectors.

Table of Contents

1 Introduction

Infections caused by pathogens remain one of the leading causes of death today, and the emergence of the currently ongoing SARS-CoV-2 pandemic places particular emphasis on this issue [1,2]. To properly treat patients and to contain the spread, specific identification of the pathogen is necessary. Especially in emergencies, when accurate determination is required quickly, the currently used detection systems are inadequate due to their required laboratory connection [3] and determination time, which in some cases can take several days [4,5], highlighting the need for further research.

One way to detect pathogens is to bind molecules that emit light after a chemical reaction or after excitation with light, which is known as chemiluminescence or fluorescence respectively. The chemiluminescence detection method is used to detect trace concentrations of molecules, in which only a few photons are released. Therefore, a detector with the highest possible sensitivity is required [6] (**Figure 1.1 A**). The single photon avalanche diode (SPAD) array detector investigated here has an extremely high sensitivity, which makes it is possible to detect single photons. Most commercial instruments have a complex and large optical system, thus making a portable operation difficult [7]. For this reason, a compact and simple first setup was developed in this dissertation to detect SARS-CoV-2 RNA and single-stranded (ss)DNA. Optimal design parameters for the measurement setup and SPAD array detector were determined by subsequent simulations.

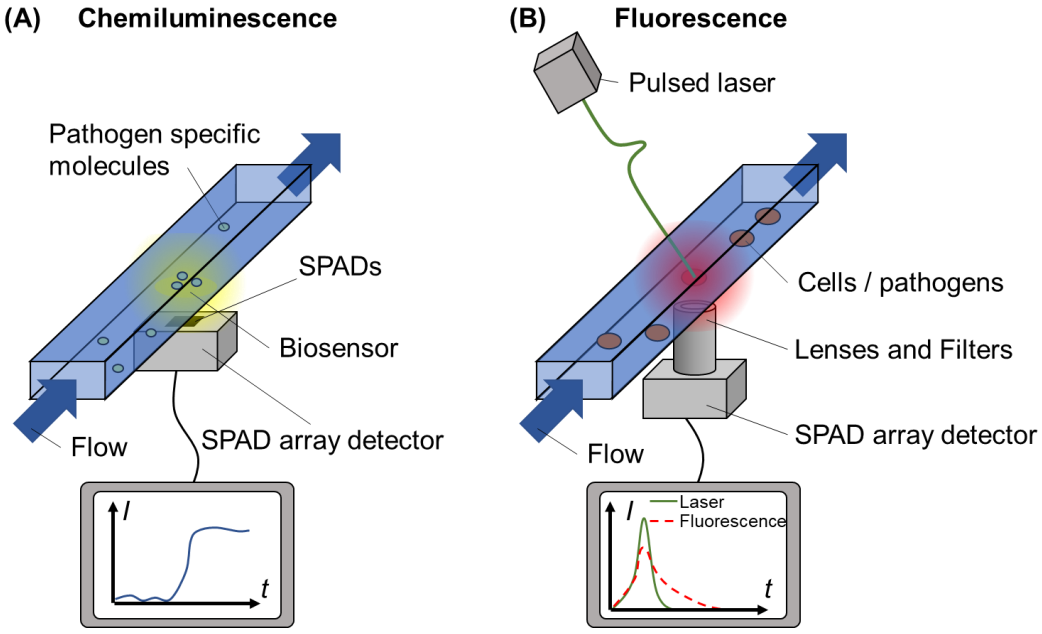

Figure 1.1: Schematic representations of the measurement methods investigated here. **(A) Chemiluminescence:** Pathogen-specific molecules bind on a biosensor as they flow through a fluidic. Depending on the concentration of the pathogen-specific molecules, a chemical reaction with other molecules generates chemiluminescence, which is detected as a signal on the SPAD array detector.
(B) Fluorescence: Excitation of fluorophores within cells with short laser pulses flowing through a fluidic channel. The emitted fluorescence is collected by lenses, then passed through optical filters and detected by the SPAD array detector. The fluorescence lifetime is then determined from the detected decay signals.

In fluorescence, the decay behavior after excitation with a laser pulse can be used as a characteristic parameter, called fluorescence lifetime (FL), to distinguish molecules or certain states from each other [8]. Since these times are in the ns range, a SPAD array detector with a corresponding time resolution is used for the second setup developed in this dissertation. In addition to the design parameters of the SPAD array detector required for FL determination, the possibility of increasing the multiplexing degree to differentiate multiple molecules was investigated and Flow cytometry was selected as a possible application. In this method, suspended cells are analyzed during a flow in a fluidic channel, with only a few microseconds available for the measurement time of each cell [9] (**Figure 1.1 B**). Thus, in this

dissertation, the required design parameters of the SPAD array detector for use in flow cytometers were also investigated.

To enable the detection of pathogens chemiluminescence and fluorescence use specific molecules, *e.g.* antibodies [10], DNA, RNA, or proteins, [11,12] to label the components characteristic of the pathogens, which in turn can be detected by the emission of photons. Detection methods using chemiluminescence use the attached molecule as a catalyst, which drives a chemical reaction that results in the emission of photons. A well-known example of this is the glow of fireflies, which are able to emit photons without the influence of the sun and can be seen in the dark [13]. However, the reactions used for detection of molecules required a catalyst that is bound to the pathogen characteristic molecule. As a result, the number of photons emitted is dependent on the concentration of the targeted pathogen. In order to be able to detect low pathogen concentrations, detectors are therefore required which, in the ideal case, can detect individual photons, as is the case with the SPAD array detector. [14]

When it is necessary to characterize and distinguish between many different pathogens, matching dyes are attached to the pathogen-labeled molecules, which, after being excited with light, also emit light, with the spectral range in which this process takes place being characteristic of the dye used. This process is called fluorescence and the dyes used for it are called fluorophores. Because the spectral range for each fluorophore extends over a certain width, the maximum distinguishable number of fluorophores and thus the number of distinguishable pathogens is limited. One way to distinguish fluorophores despite a spectral overlap is to use the characteristic intensity decay after an excitation, called fluorescence lifetime (FL). A well-known example are glow-in-the-dark stickers, which, after excitation by indoor lighting or sunlight, continue to glow in the dark for an extended period of time [15]. Nevertheless, the process occurring in this example is called phosphorescence and associated lifetimes are in the range of seconds and minutes. The FLs of fluorophores, on the other hand, are in the range of a few nanoseconds and can only be determined using detectors with an appropriate time resolution, as is the case with the SPAD array detector. [8]

The photo multiplier tube (PMT) detector is a component used in many expensive measurement systems. The PMT has a high sensitivity, which allows the detection of weak signals at low pathogen concentrations. They are also used in flow cytometry since they offer a time resolution in the ps range. However, PMTs are not suitable for compact and mobile applications due to their size, the required supply voltage of several hundred volts, their fragility and high cost [16].

SPAD array detectors, based on solid-state technology, which have only become commercially available in recent years, have the potential to compete with PMTs due to their single photon sensitivity and offer time resolution in the ps range [16]. Integrated preprocessing and a pixelated detector design also allow data to be analyzed more rapidly with less spatial requirements. Another advantage of SPAD array detectors is the mass production on wafers, which reduces costs and allows them to be used in the private sector, *e.g.* some commercially available Apple (Apple Inc., USA) products are already equipped with a SPAD array detector [17–19]. Many SPAD array detectors have been developed for applications in the biomedical field, usually with a high number of pixels and also a high time resolution. The resulting high complexity leads to more processing steps required and thus to higher costs. [20]

A particular advantage of SPAD array detectors over PMTs is the pixelated detector design, which allows FLs to be determined in fractions of a second instead of several minutes [8,21]. This opens up further applications that were previously limited, such as the combination of flow cytometry and time-domain determined FL [22]. The FL from fluorophores and its change is used in many applications such as to study molecular interactions [23,24], or for multi-parametric bioassays [25]. However, it is also possible to use the determined FLs to obtain the fractional contributions of the individual fluorophores in a mixture and to allow differentiation when this is not possible due to overlap of the emission spectra [26]. Background fluorescence, generated by unbound fluorophores or autofluorescent molecules in the medium, can make it further difficult to differentiate the desired fluorescence [27], which is why it is also possible here to differentiate the desired fluorescence using the fractional contributions based on the FLs.

To determine the necessary design parameters of the SPAD array detector and the optimal setup for chemiluminescence detection for pathogen detection, a measurement system for SARS-CoV-2 detection was developed in **Chapter 3**. Various SARS-CoV-2 RNA and ss-DNA concentrations were then successfully detected and compared with the sensitivity of a plate reader equipped with a PMT. Monte Carlo simulations were then used to determine the optimal SPAD array detector and measurement system parameters for detecting even lower pathogen concentrations.

In **Chapter 4**, another SPAD array detector measurement system was developed to investigate the necessary system parameters to determine the characteristic FLs. Using Monte Carlo simulations and verified by experiments, it was possible to show how many photons are required for an FL determination and how the respective SPAD parameters affect the measurement time of a FL determination. The results showed that FL determinations are possible at µs measurement durations with only 30 pixel. For the differentiation of fluorophores present in a mixture, in **Chapter 5** the determination of fractional contributions based on FLs was investigated, using fluorophores with overlapping spectra. For this purpose, different fluorophore mixtures were studied at various concentrations. Monte Carlo simulations were then used to determine the maximum possible fluorophore number and required FL differences. By using artificial neural networks (ANN), which have only recently started to be used to determine FLs [28], it was then shown that the determination of fractional contributions could be improved compared to the conventionally used method.

In **Chapter 6**, the SPAD array detector measurement system developed here for FL determination was used to investigate the possibility of differentiating and counting microparticles during a flow cytometric measurement, despite high background fluorescence in the same spectral region. This was accomplished by experiments with different fluorophores in the medium, and Monte Carlo simulations to determine the necessary fractional contributions and photon counts up to which differentiation of microparticles is possible. This was then used to derive the maximum possible flow rate possible with the SPAD array detector utilized. In summary, the investigations performed here made it possible to determine the required

system parameters of SPAD array detectors needed for pathogen detection by chemiluminescence in compact and mobile applications and for differentiation in fluorophore mixtures based on FLs in flow cytometry. The studies performed here provide a basis on which SPAD array detector chips can be designed specifically for these applications.

2 State of the Art

2.1 Luminescence

The term "Luminescenz" was used for the first time by the German physicist Eilhardt Wiedemann in 1888 [29] and describes the emission of light (Latin “Lumen”) from a substance that is in an excited state, where the excitation can occur in a variety of ways, such as a chemical reaction or by absorption of photons [30]. However, even long before this time, people could observe processes in nature in which light is produced by luminescence, such as aurora borealis, fireflies, or even with wood and rotting fish [31].

2.1.1 Chemiluminescence

In the process of chemiluminescence, first described by Radziszewski in 1877 [32], one of the resulting products after a chemical reaction is in an electronically excited state so that it emits light in the visible range ($\lambda = 300 \text{ to } 800 \text{ nm}$ [33]) once the ground state is reached. Chemiluminescence reactions generally use a substrate and an oxidant with some cofactors, allowing two different processes, direct and indirect, by which the reaction can proceed. In a direct chemiluminescence, the product is obtained, which emits photon in the process. In an indirect chemiluminescence, on the other hand, an intermediate product is first obtained, which can either transfer the energy to another molecule to release the photon, or

must first be converted to an excited state product for the emission of the photon. In some cases, a catalyst is also used for these reactions. [6]

One of the best known examples of direct chemiluminescence is the oxidation of luminol (5-aminophthalylhydrazides) as substrate in alkaline medium, using hydrogen peroxide as oxidant and metal ions (such as Fe(II), Cu(II), Co(II)), or enzymes (such as horseradish peroxidase (HRP)) as catalysts (**Figure 2.1**). This reaction is often used to detect the presence of the catalysts. An advantage of this detection principle is that the enzymes used as catalysts can be coupled to any antibody or antigen. To be used in an assay, however, the enzymes must provide a high quantum yield and not interfere with the physicochemical properties of the coupled antibody or antigen. [34]

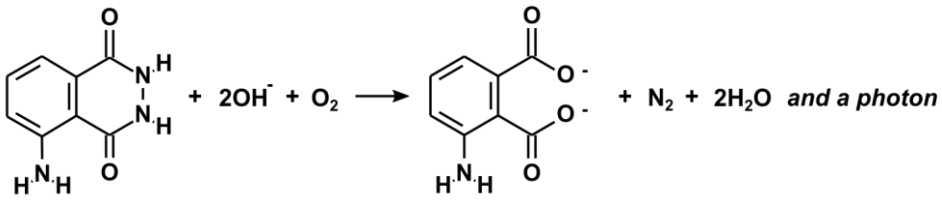

Figure 2.1: Proposed mechanism for the CL reaction. Luminol (left) reacts in an alkaline medium and with an oxygen molecule to 3-aminophthalate (right) with a nitrogen molecule, two water molecules and the emission of a photon (adapted from [34]).

Chemiluminescence is applied in a wide range of analytical chemistry and is often used in biomedical and environmental analysis. One important field is immunoassay methods, which allow quantification of almost all analytes at nano- and picomolar levels [35]. This method is most commonly used in conjunction with standardized multi-well plates on laboratory instruments that allow parallelized analysis, such as plate readers. However, developments in lab-on-chip technology allow these measurements to be performed in microfluidics with much lower use of reagents [36].

2.1.2 Fluorescence and its Lifetime

Another type of luminescence is fluorescence, which describes the emission of a photon from a substance after it has been electronically excited by a photon. A quantum mechanical description (**Figure 2.2**) involves the electron being raised from its ground state S_0 to an S_1 or S_2 state by absorption of a photon. Since this vibrationally and rotationally excited state is thermodynamically unstable, the electron falls back to the ground state S_0. Along the way, the electron falls from S_2 to the S_1 state, however, this state is radiationless and the energy is released as vibrational energy. Whereas during the transition from S_1 to the ground state S_0 a fluorescence photon is emitted. [6,8]

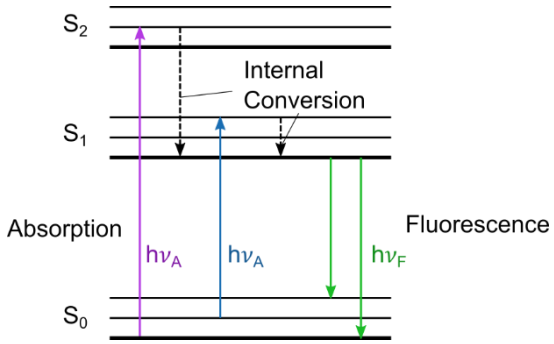

Figure 2.2: One form of a Jablonski diagram showing the occurrence of fluorescence [8] (with permission by Springer Nature).

In addition to the bandgaps between levels in the S_1 state and the ground state S_0, which define the absorption and emission spectra [37], the quantum yield and fluorescence lifetime (FL) τ are among the two most important parameters of a fluorophore. A high quantum yield, such as for rhodamine, is achieved when a large fraction of the absorbed light is also emitted. The FL, meanwhile, is the average time the fluorophore molecule spends in the excited state. However, fluorescence is a random process whose emission probability can be described by a multiexponential decay curve, with α_i as pre-exponential factors determine the emitted intensity I during time t.

$$I = \sum_{\mathrm{i}} \alpha_{\mathrm{i}} e^{-\frac{t}{\tau_{\mathrm{i}}}}. \tag{1}$$

There are many cases where fluorophores exhibit mono-exponential behavior, where 63% of the molecules have released a photon at $t = \tau$ and the remaining 37% are emitted only thereafter, with FLs in the range of 1 to 10 ns for most fluorophores. [8,38]

Fluorophores are used to be attached as labels to specific molecules and thus make them recognizable. If several fluorophores are used on correspondingly different molecules, differences in spectral emission are used to differentiate them, usually by means of optical filters. However, if the spectral differences are too small to achieve a clear differentiation, it is possible to perform a differentiation using the characteristic FL by determining the intensity-related fractional contributions P of each fluorophore

$$P = \frac{\alpha_i \tau_i}{\sum_i \alpha_i \tau_i}. \quad (2)$$

If more than two fluorophores are present in a mixture, the determination of all factors is usually not achievable because multiple possible solutions are available. Although the FL of a fluorophore may change due to its proximity to other molecules, in most cases these changes are very small or predictable [39]. Therefore, in many cases it can be assumed that the FL remains constant even in the mixture, enabling a determination of the fractional contributions (**Equation 2**) even when the fluorophore number is high. [8]

Thousands of fluorescent probes with different properties and applications are known. They allow the study of molecular and cellular dynamics, biological and biomedical imaging, clinical applications, proteomics, genomics and flow cytometry, among others [40]. Research is also being conducted to detect pathogens based on fluorophores for private use [41,42].

2.2 Single Photon Avalanche Diode

In **Section 2.1.1 and 2.1.2** the importance of a high sensitivity and time resolution in luminescence measurements was shown. Conventionally, PMTs are used for this purpose, but they are limited in their application by their disadvantages such as a bulky size and a single pixel area. Single photon avalanche diodes (SPADs) array detectors can be seen as an alternative to this technology, although this technology is still very young with the first one being fabricated only in 2003 [43]. Therefore, developments that address and improve upon the limitations currently encountered are to be expected. For this reason, in the research conducted here, a focus was placed in the customizable aspect of SPAD array detectors, such as the number of pixels and data evaluation, which are independent of the current stage of development.

2.2.1 Operating Principle

SPADs essentially consist of two differently doped silicon layers forming a pn junction, in which free electrons from the n-region recombine with the holes in the p-region, leaving space charges of uncompensated solid ions. Since the space charges face each other, an electric field is built up, which counteracts diffusion and forms a so-called depletion zone at equilibrium. The pn junction is operated in Geiger mode, *i.e.* the applied voltage is higher than the breakdown voltage. If free charge carriers are now generated in the depletion region, *e.g.* by a photon, an avalanche of charge carriers is generated, releasing further charge carriers. This current is then detected as a signal and processed further. Since this process is self-sustaining, the applied voltage of the SPAD must fall below the breakdown voltage to stop the generation of charge carriers, which is called quenching. To become photosensitive again, the voltage must then be raised back above the breakdown voltage. The properties of the SPADs, such as sensitivity, time resolution, or noise are determined by the manufacturing processes used and the underlying design. A distinction is made here between fixed characteristics, which depend on the

SPAD build used, and between design parameters, which can be adapted to the specific application as required. [44,45]

2.2.2 Characteristics

SPAD array detectors have many characteristics that are limited by current advances and the fabrication techniques used, such as lithography scale. This includes the entire setup with SPAD, quenching and evaluation circuitry. The quenching circuit used (active or passive) determines how fast the SPAD is reset and thus specifies over what period of time, called dead time, the SPAD is not sensitive. Passive quenching is implemented using a high impedance resistor, which causes the voltage to drop below the breakdown voltage as soon as the SPAD is activated. Active quenching, on the other hand, uses a variable resistor that has a high value to stop the avalanche current and a low value when the voltage is applied. When using an active quenching circuit, the achievable count rate [46] and the ability to time-gate the SPAD [47], among other things, improve. However, this increases the space required for the circuitry compared to passive quenching, which increases the distance between SPAD pixels. [48]

Another characteristic is the dark count rate (DCR), which also depends on the SPAD build used. The DCR is a detected signal, which is generated without the influence of photons and is detected as uncorrelated noise. Causes are: Carrier diffusion from the neutral region, thermal generation of electron-hole pairs and band-to-band tunneling [49]. Cooling the SPAD array detector can reduce the number of thermally generated electron-hole pairs and thus the DCR, whereas insufficient heat dissipation in turn increases the DCR. Correlated noise manifests itself in the context of a triggered SPAD as, a direct re-activation occurs without absorption of a photon (afterpulsing), or by neighboring SPADs interfering with each other and thus triggering (crosstalk). These can be reduced by a sufficient time interval between the charging process after quenching [50] and a higher distance between the SPADs [51].

The temporal jitter is the average difference between the time of the incoming photon and the detected signal and is determined by the statistical behavior of the avalanche breakdown [48].

Other parameters that are fixed by the SPAD structure include the quantum efficiency and the avalanche triggering probability. The quantum efficiency indicates the ratio of how many electron-hole pairs a photon generates in the detector and depends, among other things, on the material of the detector (in this case silicon), its layer thicknesses and the wavelength of the photons to be detected. The avalanche trigger probability indicates with which probability an avalanche will occur after the absorption. However, these parameters will not be discussed further because they depend on the fabrication parameters and processes used. [52]

2.2.3 Design Parameters

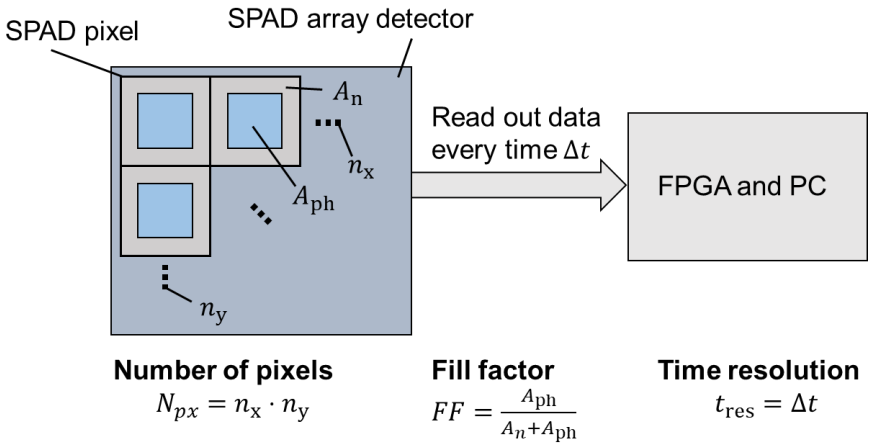

Figure 2.3: Schematic drawing of the adjustable SPAD array detector parameters. The pixel number N_{px} indicates the number of all pixels in the array with a respective connection and readout circuit. The fill factor is the ratio of the photosensitive area A_{ph} to the total pixel area. The fill factor decreases with increasing non-photosensitive area A_n. This area depends on the protection structures, connections and placement of readout circuits. The time resolution t_{res} is given by the frequency at which data from all pixels is read out or buffered.

Among the parameters that can be customized for the respective application is the time resolution, which is limited by the temporal jitter that a SPAD can achieve in the range of a few ps. The actual time resolution is determined by the readout circuitry connected to the SPAD. Different time stamp principles, with their respective advantages and disadvantages, can be used, such as time to digital converters (TDCs) or time to analog converters (TACs) followed by analog to digital converters (ADCs) [53]. If a high time resolution is selected, the required data rate to be read out by the SPAD also increases. By buffering data and reading it out later, high time resolutions can be achieved, but it is then not possible to perform successive measurements, since a certain amount of time is required to read out the data from the chip. Therefore, a time resolution should be selected that is also required for the specific application (**Figure 2.3**).

The fill factor (FF) is another important, but only partially customizable, parameter and describes the ratio between the photosensitive area of the detector and the total detector area (**Figure 2.3**). This is determined by the distance between the SPAD pixels, which is present due to the guarding structures, connections and readout circuitry. Depending on the requirements for data acquisition and its preprocessing, it is possible to place it outside the SPAD array area to increase the fill factor. [54]

An optimization of one parameter is often associated with a trade-off of another. For example, increasing the number of pixels increases the area over which photons can be recorded, but is also associated with a higher data rate to be read out and a lower fill factor, since a higher number of connections have to be routed off the SPAD area.

2.2.4 SPAD Array Detectors

Applications for SPAD array detectors include those in which distance measurements are used for 3D mapping by means of Light detection and ranging (LiDAR), such as the automotive industry for the navigation of autonomous vehicles, or for speed controls. This is due to the high time resolution of the SPAD array detector, which makes it possible to perform time-of-flight measurements. This in-

volves determining the time it takes for a laser pulse to travel back to the detector after reflecting off an object, in order to determine the distance traveled based on the constant speed of light [55]. Furthermore, in addition to the biophotonics applications investigated in this dissertation, others are possible, such as Förster resonance energy transfer, single-plane illumination fluorescence correlation spectroscopy, localization- and entangled photons-based super-resolution microscopy, time-resolved Raman spectroscopy, near-infra-red optical tomography and positron emission tomography [56]. Since the applications of chemiluminescence and FL determination were studied here, only the parameters that mainly affect these types of measurements were included in the comparison of different SPAD array detectors (**Table 2.1**).

Table 2.1: SPAD array detectors published since 2016 with the comparison of the previously described design parameters. The excess-bias voltage V_{ex} is the difference between bias and breakdown voltages. In this work SPAD-array No. 7 was used for chemiluminescence measurements, SPAD-array No. 8 was used for FL determination.

No.	Pixel arrangement	SPAD size (µm)	FF (%)	Max. time resolution (ps)	Measurement transfer time (µs)	Median DCR (Hz) @ V_{ex} and 300 K	Reference
1	32x32	19.8	19.5	210	591	360 @ 2.5	[53]
2	5x5	57	57.5	125	External evaluation	2 k @ 5	[54]
3	512x512	16.4	10.5	140	10.2	1.97 M @ 6.5	[57]
4	192x128	5.4	13	33	53.8	25 @ 1.5	[58]
5	32x64	30	3.14	400	0.02	307 k @ -	[59]
6	32x32	8	10	50	5.3	102 k @ -	[22]
7	8x8	30	14	No timestamp	No single measurement	68 @ -	[60]
8	2x192	12	5.32	312.5	21.25	40 @ 4.7	[61]

As described at the beginning of this section, the parameters of new SPAD array detectors are expected to improve as development progresses, so recently published SPAD array detectors have been used here for comparison (**Table 2.1**: Nos. 1, 2, 5 from 2020, Nos. 3, 4 from 2019, No. 8 from 2018, No. 6 from 2016). The SPAD array detectors No. 1 to 6, compared here, were developed by different research groups, for applications including fluorescence lifetime imaging microscopy (FLIM), for which reason, in order to achieve sufficient resolution, they usually have more than 100 pixels and mostly equal aspect ratios in both dimensions. Only No. 2 has a lower number of pixels, with the focus here being on a higher fill factor. For the SPAD array detectors compared here, the pixel size ranges from 8 to 57 µm in diameter. The time resolution of all compared SPAD array detectors is in the ps range, except for #7 which has no readout time stamps (see **Figure 2.5**), with the highest being Nr. 4 with 33 ps. The measurement transmission time indicates the time after which a measurement can be repeated. The shorter this time, the faster the required photon numbers can be obtained and the faster the FL determination. Among the SPAD array detectors compared here, no. 5 has the shortest measured value transmission time of 20 ns. However, in order for the detected photons to register as a signal, they must be above the noise level caused by the DCR, which ranges from 25 Hz to 1.97 MHz in this comparison.

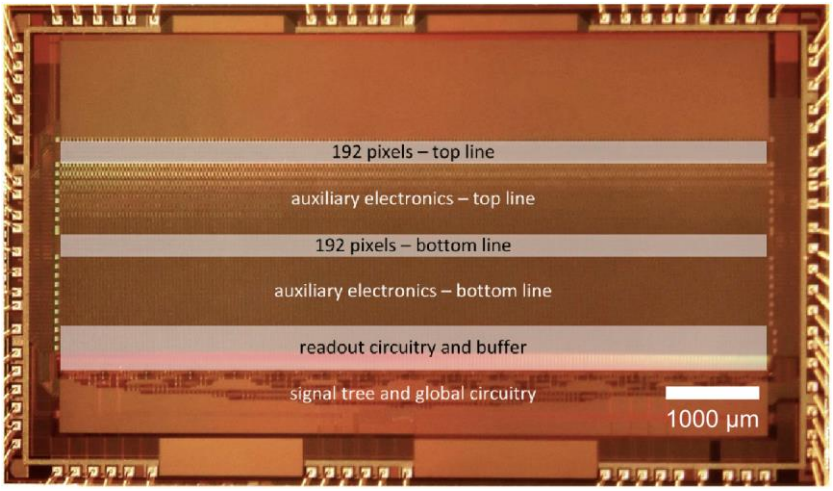

Figure 2.4: The SPAD array detector used in this work for FL determination. Here, a higher fill factor was achieved by relocating the evaluation circuit outside the pixel areas. [62]

For the determination of FLs, SPAD array detector No. 8 was selected in this dissertation (**Figure 2.4**). Since FLs were not determined spatially resolved here, a pixel array of 2x192 is sufficient to investigate the accelerated FL determination by parallel acquisition at multiple pixels. Although the measurement transfer time is not particularly low in the comparison shown here, the time stamps of all pixels are output after each measurement. The DCR in contrast is one of the lowest in the comparison, this is helpful to detect even weak fluorescence signals.

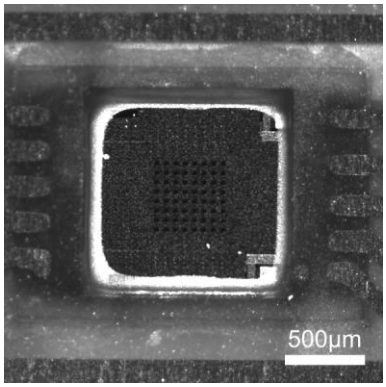

Figure 2.5: The SPAD array detector used in this work for CL measurements. Image of the 8x8 SPAD array detector taken with a microscope with the actual SPADs recognizable by the darker dots in the center of the detector. One pixel has a diameter of $30\ \mu m$.

In contrast to fluorescence, chemiluminescence usually produces only a few photons over a long period of several seconds to minutes, so a time resolution in the seconds range is sufficient. For this reason, no time stamps are read out in the SPAD array detector #7 used in this dissertation (**Figure 2.5**), which was developed at Fraunhofer IMS. To detect as many photons as possible, the detector should have a large photosensitive area, which depends on the number of pixels, pixel size, and fill factor. However, the parameters of the SPAD array detector used here are not particularly high in comparison. In order to register even weak signals in chemiluminescence measurements, the DCR should be as low as possible. Suitable for this application, the DCR of the SPAD array detector used here is one of the lowest in the comparison.

3 SARS-CoV-2 Chemiluminescence Detection Using a SPAD Setup

Since the emergence of Severe Acute Respiratory Syndrome Coronavirus 2 (SARS-CoV-2) in December 2019, the virus has spread around the world after just a few months. Containment issues include the difficulty of diagnosing SARS-CoV-2 with a high degree of certainty, as not all infected individuals show symptoms and, if often, are not noticeable until later in the course of the disease [63]. However, the risk of infection exists regardless of whether symptoms occur [64]. Therefore, to contain the pandemic, it is of high importance to test the majority of the population. Unfortunately, the reverse transcription polymerase chain reaction (RT-PCR), which is considered the gold standard, has shown drawbacks in large-scale use, as it requires significant laboratory infrastructure and qualified personnel, but also because there have been occasional bottlenecks in the supply of required reagents [65,66]. For this purpose, the Point-of-Care (PoC) rapid diagnostic tests (RDTs) used are mostly based on antigen detection (Ag)-RDT, which are cheaper and instead of taking several hours, usually provide the test result in less than 30 min, they do not require an additional laboratory request, and can be performed by anyone. However, the disadvantage of PoC tests is that they are less sensitive than RT-PCR based test systems [65].

In this chapter it was evaluated whether a lens-free SPAD-based measurement setup has sufficiently high sensitivity to be used for the detection of SARS-CoV-2. For this purpose, such a measurement setup, referred to here as a SPAD setup, was developed and used to study detection of SARS-CoV-2 RNA and single-stranded (ss)DNA. To assess the sensitivity of the SPAD setup, comparative measurements were performed on a commercial plate reader and Monte Carlo simulations were performed showing the effects of the size, pixel arrangement and number of SPAD array detector pixels, biosensor size and any intermediate layers on the detection of the chemiluminescence signal. The results were used to determine the limitations of the SPAD setup and to find possible optimization measures.

3.1 Chemiluminescence Measurement System

A PoC application usually consists of a low-cost disposable cartridge containing the required analytical reagents and an expensive readout device consisting of a detector and readout electronics. This concept was used for the SPAD setup developed here, which features a 2-component system of a cartridge, consisting of a microfluidic system with biosensors, and a base station, consisting of SPAD array detectors with a field programmable gate array (FPGA) readout unit (**Figure 3.2 A**). To keep size and complexity as low as possible, no lenses were integrated (**Figure 3.1**).

The SPAD setup is located in a closed and blackened aluminum box to protect it from stray light. The sample to be analyzed enters the microfluidics of the cartridge from the outside via connected tubing (**Figure 3.2 A**). The microfluidic consists of a double-sided adhesive tape ($d = 120\ \mu\mathrm{m}$) with the microfluidic cut to size, glued on one side to the polyether ether ketone (PEEK) lid with the tubing connections and sealed by a polystyrene (PS) film (**Figure 3.1** and **Figure 3.2 C**). Prior to attaching the films, the biosensors were spotted onto the PS film (described in more detail in **Section 3.3**).

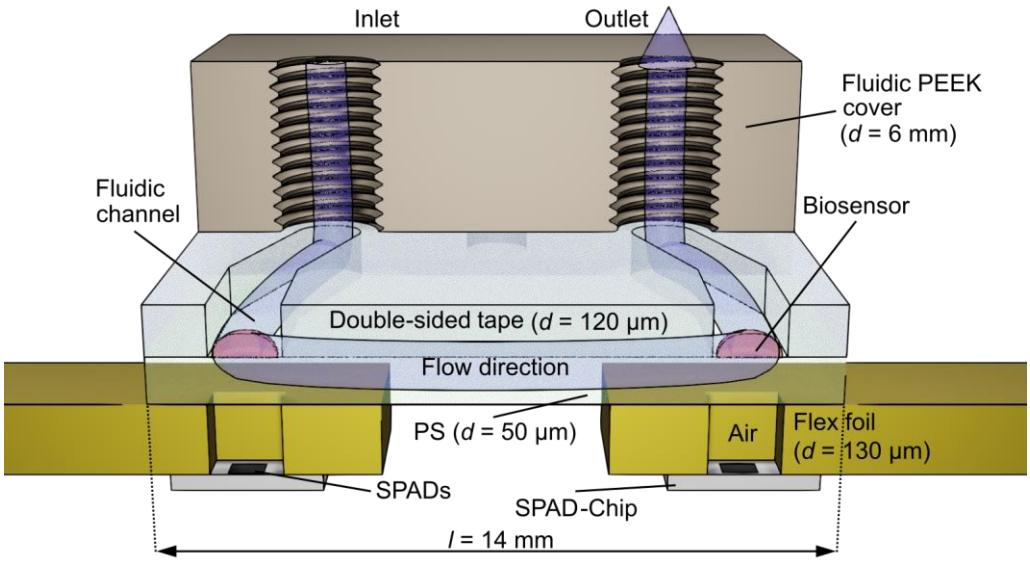

Figure 3.1: Schematic sectional view of the SPAD setup. The microfluidic channel consists of a cut-to-size double-sided adhesive tape bonded between a polyether ether ketone (PEEK) lid and a thin polystyrene (PS) film. Threads for the inlet and outlet are machined into the PEEK lid. Chemiluminescence is emitted at the biosensors inside the liquid channel. To detect this emitted light, the cartridge containing the biosensors is positioned exactly above two SPAD array detectors, with each SPAD chip connected to a flexible film at the bottom. The flexible films are perforated above the light-sensitive SPADs and connected to the respective readout circuits via integrated wiring.

The cartridge containing the microfluidics is attached to the base station by two magnets and two positioning pins, so that the biosensors located in the microfluidics are just above the two SPAD array detectors (**Figure 3.2 B**).

There are 2 SPAD array detectors attached to the base station, each connected via a flex foil to two printed circuit boards (PCBs) necessary for readout (**Figure 3.2 B**). The chips of the SPAD array detector are bonded to the bottom of the flex sheet, with the photosensitive SPADs capturing photons from the biosensor through an opening in the flex foil (**Figure 3.1**).

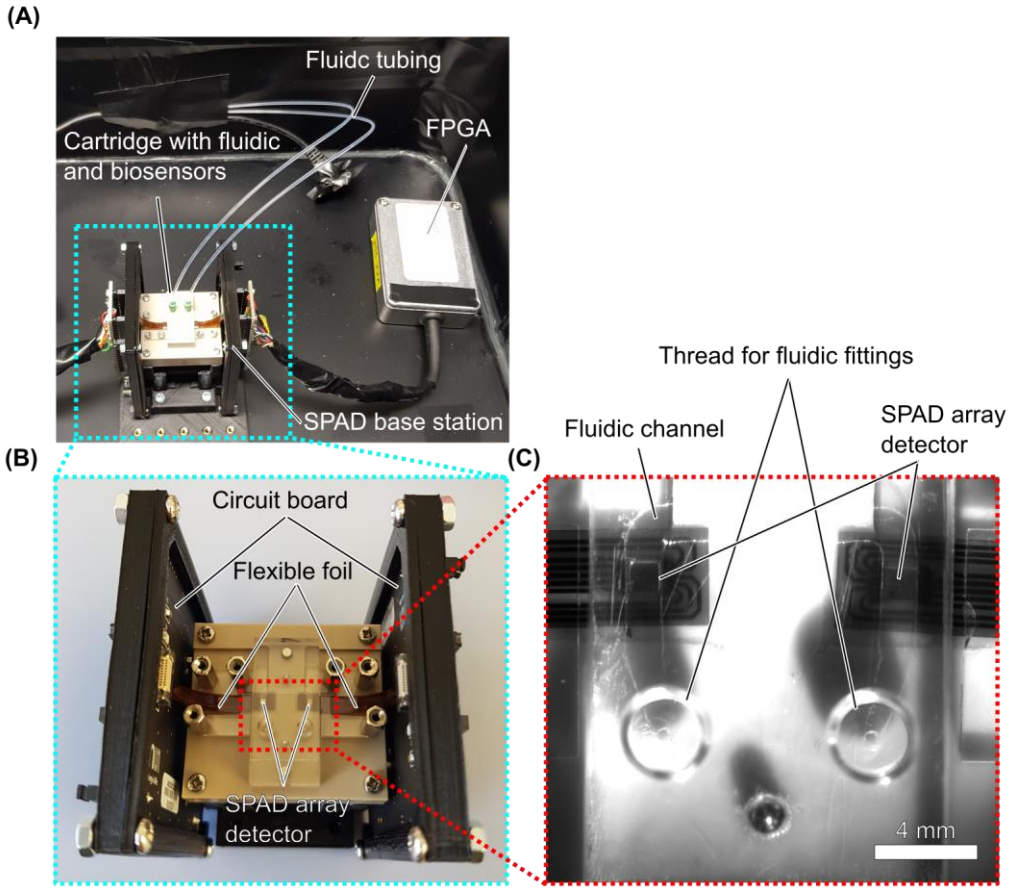

Figure 3.2: Images of the developed SPAD setup.
(A) SPAD setup: The SPAD setup is located inside a blackened aluminum box with FPGA and SPAD base station. Into the box leads tubing for sample delivery and a USB cable for data readout.
(B) Base station: On the base station is an inserted cartridge (transparent here for visualization, but non-transparent PEEK material for measurements) below which are the SPAD array detectors, connected via flex foil to the respective readout circuit.
(C) Cartridge: U-shaped microfluidic channel with inlet and outlet, described in more detail in **Figure 3.1**.

3.2 Potential of the SPAD Array Detector Measurement Systems

To detect chemiluminescence, plate readers are conventionally used. Such systems use standardized multi-well plates, where each well is individually controlled and the emitted light is captured via complex optical systems and detected on a PMT [67]. To assess the potential of the developed SPAD setup and to estimate the detectability of the titration curve with the developed SPAD array detector, the detected chemiluminescence in a plate reader was compared with that in the SPAD array detector without using SARS-CoV2 ssDNA and RNA (**Figure 3.3**). For this purpose, a black multi-well plate was used (**Figure 3.3 A 1.**), in which a hole was drilled at the bottom of a well (**Figure 3.3 A 2.**) and sealed by vacuum grease using PS foil (**Figure 3.3 A 3.**). Anti-DIG antibody with horseradish peroxidase (HRP) (0.1 U/ml and 0.5 U/ml) was incubated on the attached PS film for one night at 4 °C and the unbound anti-DIG HRP was washed off the next day (**Figure 3.3 A 4.**). After addition of luminol/H_2O_2 into the prepared multi-well, chemiluminescence started and was measured in the plate reader (Tecan Infinite Pro, SUI) (**Figure 3.3 A 5.**) and above the SPAD array detector (**Figure 3.3 A 6.**), respectively.

The measurements were repeated three times with three different wells for anti-DIG HRP concentration 5 U/ml and with two different wells for 0.1 U/ml **(Figure 3.3 B)**. U is used here as the enzyme unit defining substrate conversion in µmol per min. The mean value was then determined from the detected intensities of the chemiluminescence measurement of each well and the measurement was repeated three times per well. Since the distributions resemble a logarithmic distribution, the geometric means and standard errors were determined from the determined intensity values.

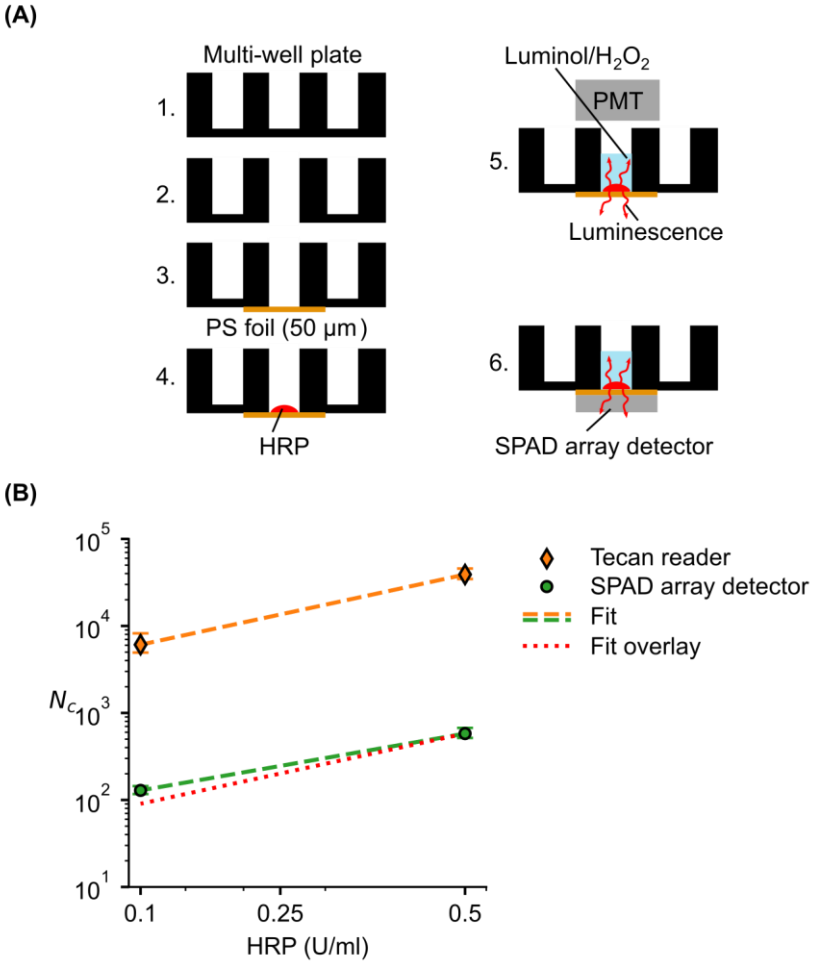

Figure 3.3: Comparison between plate reader system and SPAD array detector.
(A) Multi-well plate preparation steps: (2.) Removal of the well bottom, (3.) sealing of the opening with a PS film, and (4.) incubation of anti-DIG antibody with horseradish peroxidase HRP on the PS film. After adding luminol/H_2O_2, measuring of chemiluminescence in (5.) Tecan plate reader and (6.) SPAD array detector at two different concentrations (0.1 U/ml and 0.5 U/ml). U is used here as the enzyme unit defining substrate conversion in µmol per min.
(B) Measurement results: Comparison of the measured mean photon count number of both measurement systems leads to an offset factor (obtained by overlaying the line fit of the Tecan reader on that of the SPAD array detector, red dotted curve) of the Tecan plate reader of 67. Error bars in (B) are partially smaller than the markers

Measurements at different anti-DIG HRP concentrations showed that the intensity change of the Tecan plate reader and the SPAD array detector decreased in the same ratio (**Figure 3.3 B**). Since a higher intensity could be detected with the Tecan plate reader, it is more sensitive by an offset factor of 67 than the SPAD array detector directly underneath the multi-well plate.

Because of safety precautions, the SARS-CoV-2 ssDNA and RNA titration curves were performed at Fraunhofer IZI in Leipzig (**Section 3.3** and **Section 3.4**) using a different plate reader (Labrox multimode reader, Labrox Oy, FIN). To determine the sensitivity difference between the two plate readers, a titration curve was measured with the same anti-DIG HRP concentrations (**Figure 3.4**).

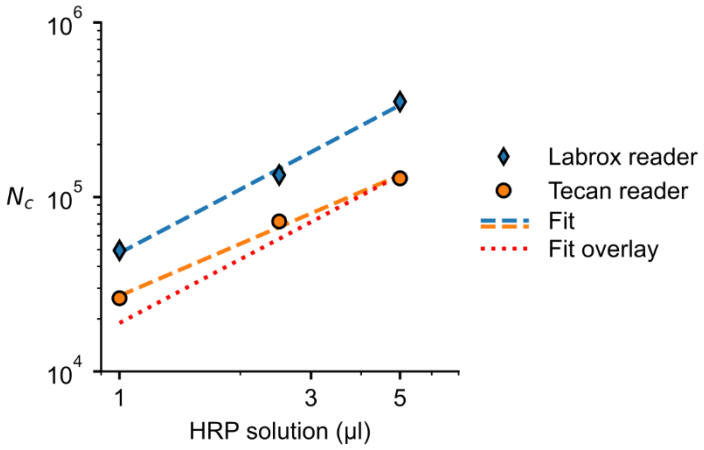

Figure 3.4: Comparison between two plate reader systems. Direct comparison between the measured intensity of two plate reader systems (Labrox blue and Tecan orange) with the resulting offset factor of 2.5, obtained from overlaying the line fits, red dotted curve.

Measurements were performed at three different anti-DIG HRP volumes using both Tecan and Labrox plate readers (**Figure 3.4**). After the measured intensity values settled to constant values (after 400 s), they were averaged.

The intensity drops with a similar ratio for both investigated systems, but with a determined offset factor of 2.5. Thus, from the two measurements performed, the total offset factor is 167.5, which describes the expected sensitivity difference in SARS-CoV-2 ssDNA and RNA detections. Since a simplified lens-free SPAD setup was developed here, a lower sensitivity is also expected.

3.3 Chemiluminescence Assay

In the following sections, SARS-CoV-2 ssDNA and RNA measurements are performed and compared on the plate reader (Labrox multimode reader) and SPAD setup. These measurements were performed by staff at Fraunhofer IZI in Leipzig, Germany, who have the necessary training and safety facilities to handle SARS-CoV-2 RNA and ssDNA.

3.3.1 Assay Principle (pre-hybridization in solution)

Reliable detection of pathogens is possible using RNA or ssDNA, which provides the flexibility to adapt an existing assay to the pathogen of interest [68]. The assay used here utilizes oligonucleotide probes (ssDNA) and chemiluminescence labelling for the detection of SARS-CoV-2 (**Figure 3.5**).

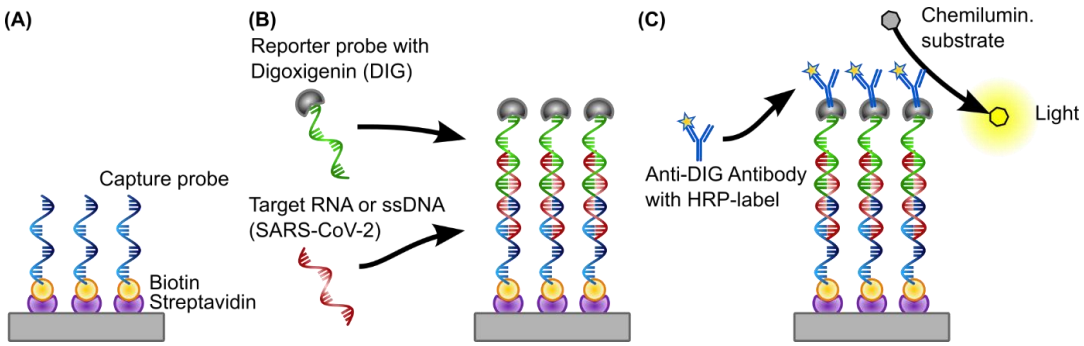

Figure 3.5: Chemiluminescence assay for the detection of SARS-CoV-2-RNA or ssDNA.
(A) Immobilization: Capture probe (ssDNA) is immobilized with biotin label to a substrate coated with streptavidin.
(B) Reporter probe: Addition of reporter probe with digoxigenin (DIG)-label and target RNA or ssDNA.
(C) Anti-DIG antibody: Addition of Anti-DIG antibody with horseradish peroxidase (HRP)-label followed by addition of chemiluminescence substrate (acridan-derivative and HO_2).

To evaluate the detection of SARS-CoV-2, an ssDNA corresponding to a fragment of the SARS-CoV-2 genome was used as a synthetic target since the required safety precautions are lower and handling is easier, and a purified genomic SARS-CoV-2 RNA was used as a real target (**Section 3.3.2**). To enable binding of the target RNA or ssDNA, a capture probe (ssDNA) with biotin label was immobilized on

a streptavidin-coated surface (**Figure 3.5 A**). After attachment of the target RNA or ssDNA of interest to the capture probe, a reporter probe (ssDNA) with digoxigenin (DIG) label is used, this process is also called "hybridization" (**Figure 3.5 B**). An anti-DIG HRP label was bound to the DIG label to catalytically oxidize the chemiluminescent substrate (luminol or acridan derivative) added in the last step in the presence of H_2O_2, generating chemiluminescent emission.

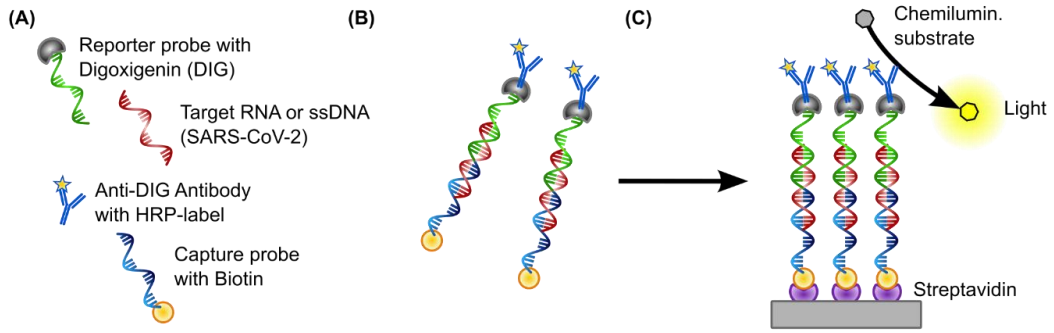

Figure 3.6: Pre-hybridization in solution.
(A) Incubation: Capture probe, reporter probe, target RNA, and anti-DIG-HRP are incubated in solution.
(B) Hybridized complex: A hybridized complex of capture probe, reporter probe, and target RNA with bound anti-DIG-HRP is obtained.
(C) Immobilization: This complex is then immobilized to a streptavidin-coated solid support via biotin-streptavidin binding.

To enable the best possible binding of the target RNA and ssDNA and to exclude as many influencing factors as possible that are difficult to assess (such as flow rates, non-specific binding, detachment effects), capture probe, target RNA or ssDNA, reporter probe and anti-DIG HRP were prehybridized in a solution for all assays performed here using the plate reader and SPAD setup (**Figure 3.6 A and B**). The resulting prehybridized complex was immobilized on a streptavidin-bound surface and catalytically oxidized in the presence of H_2O_2 using a chemiluminescent substrate (acridan derivative) and light was generated by chemiluminescence, as shown in **Figure 3.6 C**. The detailed test protocols performed during the experiments can be found in **Section 3.3.3 and 3.3.4**.

3.3.2 SARS-CoV-2 ssDNA and RNA

To evaluate the sensitivity of the SPAD setup, the first measurements were performed with the ssDNA (212 pb) of SARS-CoV-2 produced by a symmetric PCR in which one DNA strand was dominantly amplified [69]. Measurements performed here utilized purified ssDNA separated on a gel from the double-stranded (ds)DNA to obtain a purer stock without fractions of the complementary strand, resulting in more accurate ssDNA concentration values. The ssDNA used has the following sequence:

GTAG CTTGTCACAC CGTTTCTATA GATTAGCTAA TGAGTGTGCT CAAGTATTGA GTGAAATGGT CATGTGTGGC GGTTCACTAT ATGTTAAACC AGGTGGAACC TCATCAGGAG ATGCCACAAC TGCTTATGCT AATAGTGTTT TTAACATTTG TCAAGCTGTC ACGGCCAATG TTAATGCACT TTTATCTACT GATGGTAACA AAATTGCCG

The ssDNA concentration was measured by Qubit Fluorometer (ThermoFisher, US) using Qubit ssDNA Assay Kit (Thermofisher, US). The capture and reporter probes used (32 bp each) were designed to be complementary to the sequences of the inner fragment of the ssDNA:

SARS-CoV-2 capture probe: 5' ATATAGTGAACCGCCACACATGACCATTTCAC-Biotin
SARS-CoV-2 reporter probe: 5' DIG-GCATCTCCTGATGAGGTTCCACCTGGTTTAAC

The SARS-CoV-2 RNA used was isolated from a virus culture and has approximately $29{,}900$ bp [70]. The genomic RNA concentration was determined by quantitative RT-PCR.

3.3.3 Assay Protocol for Plate Reader

The capture probe was immobilized on the surface of a streptavidin plate (Pierce™ Streptavidin-coated High Capacity Plates, clear, 8-well strip, Pierce Biotechnology, US) and 50 µl of capture probe solution (100 pmol of capture probe in 4x saline-sodium citrate buffer (SSC)) was added to each well. Incubation was then

performed for $15\ \mathrm{min}$ at room temperature and $500\ \mathrm{rpm}$, and the unbound probes were removed in two consecutive 1 min wash steps with $200\ \mu\mathrm{l}$ phosphate buffer saline $+0.05\ \%$ tween-20 (PBST).

The target (ssDNA or viral RNA or water as a negative control) and the reporter probe ($5\ \mathrm{pmol}$ in 4xSSC) were added in a total volume of $50\ \mu\mathrm{l}$, the plate was covered and incubated for $30\ \mathrm{min}$ at $50\ ^{\circ}\mathrm{C}$ and $500\ \mathrm{rpm}$. The unbound compounds were then removed in two consecutive $1\ \mathrm{min}$ wash steps with $200\ \mu\mathrm{l}$ PBST. $100\ \mu\mathrm{l}$ of anti-DIG HRP (anti-digoxigenin POD (poly) Fab fragments; Roche, GER) diluted $1{:}100$ in PBST was added and incubated for $25\ \mathrm{min}$ at $25\ ^{\circ}\mathrm{C}$ and $500\ \mathrm{rpm}$, followed by two $1\ \mathrm{min}$ wash steps with $200\ \mu\mathrm{l}$ PBST.

To generate luminescence emissions upon successful binding, $100\ \mu\mathrm{l}$ of the chemiluminescent substrate acridan derivative, Lumigen ECL Ultra (Lumigen Inc., US) was added. A conventional plate reader (Labrox multimode reader, Labrox Oy, FIN) was used to detect luminescence, taking measurements with a dispenser unit in repeated cycles at $30\ \mathrm{s}$ intervals for $15\ \mathrm{min}$ immediately after addition of the substrate.

3.3.4 Assay Protocol for SPAD Setup

The following steps to apply the biosensor were performed prior to sealing the microfluidics (**Figure 3.2 D**). In this process, the area of the PS film, above the SPAD detector was first coated with streptavidin. For this, $5\ \mu\mathrm{l}$ of a $5\ \mathrm{mg/ml}$ streptavidin solution in phosphate buffer saline (PBS) was applied to the channel and incubated overnight in a humid chamber at $4\ ^{\circ}\mathrm{C}$. To remove the unbound streptavidin, three washing steps were performed in $1\ \mathrm{ml}$ PBST each with agitation and the films were dried with a gentle stream of nitrogen.

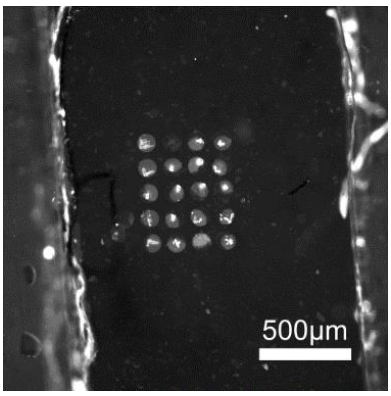

Figure 3.7: Microfluidic channel with biosensor array. Fluorescence image of fluorophore spots (500 pl per spot, Alexa Fluor 488) analogous to the biosensor, spotted in the microfluidic channel using a nanodispenser. The cartridge was imaged with a fluorescence microscope in top view without SPAD base station.

The streptavidin-coated area was spotted with 100 µM aqueous solution of the capture probe, at 75 spots/channel with a dispensed volume of 1000 pl/spot (analogous to array in **Figure 3.7**) and then washed three times in 1 ml PBST while shaking, after which the films were dried with a light stream of nitrogen.

The target (ssDNA or viral RNA or water as negative control) and the reporter probe (5 pmol in 4xSSC) were added in a total volume of 2.5 µl and incubated for 30 min at room temperature with movements of 200 rpm. Incubation at 50 °C causes the reaction mixture to dry out, thus avoiding hybridization. In three consecutive 1 min washing steps, the unbound compounds were removed with 1 ml PBST, after which the films were dried with a light stream of nitrogen.

On the hybridization surface of the film, 2.5 µl of HRP enzyme was applied at $1{:}\,100$ dilution in PBST and this was incubated for 25 minutes at room temperature while stirring. After this step, the film was adhered to the PEEK lid of the cartridge (**Figure 3.2 D**) and the biosensors were positioned in the closed microfluidic over the SPAD array detector.

The microfluidics were first primed with PBST and then 250 µl of the chemiluminescent substrate was pumped through at 200 µl/min. In order to transport the chemiluminescent substrate via the tubing to the biosensors, an additional 1000 µl of PBST was pumped through at 200 µl/min. The signal recorded at the SPAD array detector was recorded using Abios software from AMS.

3.4 Detection of SARS-CoV-2 RNA and ssDNA

In order to detect SARS-CoV-2, either the spike proteins located on the outer membrane are detected, or the RNA located in the interior is used, which is usually amplified by PCR [71]. The advantage of antigen detection is the high number of spike proteins per virus and the ease of use of these PoC test systems, but they usually have only a low sensitivity (11-40 % [72]). SARS-CoV-2 detection by RNA followed by RT-PCR is considered the gold standard [73], but is only possible in specialized laboratories with skilled personnel and is therefore associated with high costs. Currently, there is no detection method with high sensitivity, easy handling, high speed and low cost.

For this reason, we investigate whether a PCR-free method has the required sensitivity to be used as a detection method for ssDNA and RNA and what parameters such a setup must have to meet the requirements. The detection of RNA and ssDNA measured using the plate reader (Labrox multimode reader) was repeated 3 times (**Figure 3.8**). For this purpose, the mean value of the first 10 measuring points of the plate reader was determined for each concentration. From the repetitions, the geometrical mean value and standard deviation was determined for each concentration, which is shown in the error bars.

The determination of the chemiluminescence signal at different ssDNA and RNA concentrations (**Figure 3.8 A and B**) on the commercial plate reader (Labrox multimode reader) showed a linear dependence ($R^2 = 0.98$ and $R^2 = 0.93$, respectively). From the intersection of the linear fit and the negative control with three times the standard deviation, the limit of detection (LOD) is $\mathrm{LOD_{ssDNA}} = 2.4 \cdot 10^7\ \mathrm{copies/ml}$ and $\mathrm{LOD_{RNA}} = 5.7 \cdot 10^9\ \mathrm{copies/ml}$. The higher LOD in RNA detection probably results from the size differences of ssDNA ($213\ \mathrm{bp}$) and RNA (about $29{,}900\ \mathrm{bp}$), which strongly affects hybridization efficiency.

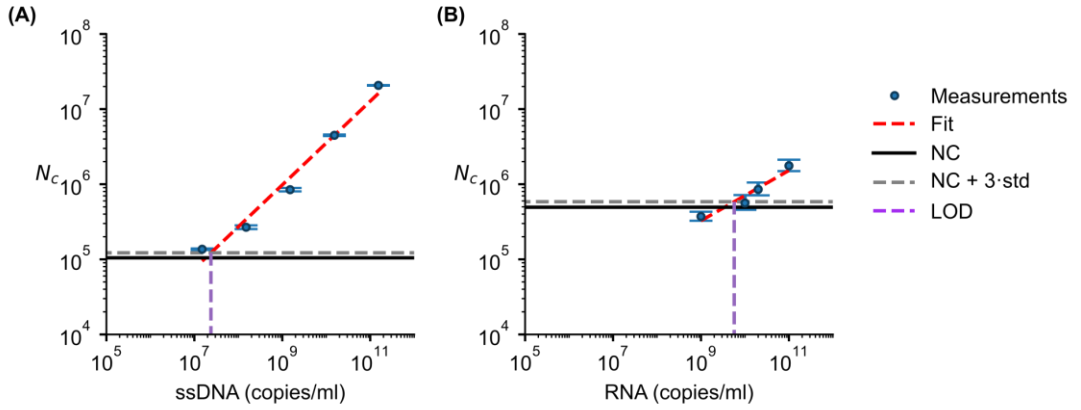

Figure 3.8: SARS-CoV-2 (A) ssDNA or (B) RNA detection using Labrox plate reader. The titration curve measured on the Labrox plate reader shows that as the concentration decreases, a lower intensity is detected (blue dots). The limit of detection (purple dashed curve) results from the negative control (black curve) without the use of RNA or ssDNA with three times its standard deviation (grey dashed curve).

Compared to LOD of some currently approved RT-PCR kits ($500\,\mathrm{copies/ml}$ [74]) and many commercially available Ag-RDT ($\mathrm{LOD} = 10^5$ to $10^7\,\mathrm{copies/ml}$ [65] in direct viral cultures), the method used here has a very high LOD when detecting RNA. The sensitivity defined by the World Health Organization (WHO) as acceptable ($\mathrm{LOD} = 10^6\,\mathrm{copies/ml}$) and desirable ($\mathrm{LOD} = 10^4\,\mathrm{copies/ml}$) [75] was also not achieved. The number of photon counts at LOD ($N_\mathrm{c} = 1.2 \cdot 10^5$) likely results from non-specific bindings, which also occurs in the absence of ssDNA and RNA to be detected. An increase can be expected by optimizing the assay protocol (*e.g.*, temperatures used, number of wash steps and concentrations) or increasing the target concentration by amplification, the number and area of the biosensor capture probes, or the use of auxiliary probes to increase the number of possible bindings to the target. The optimization steps of the assay, however, are not the focus of the studies performed here, but the sensitivity of the SPAD setup developed here.

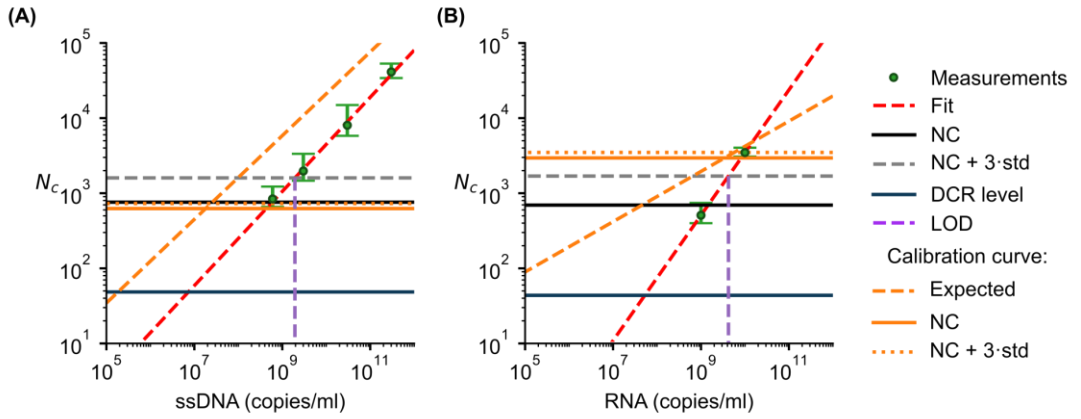

Figure 3.9: SARS-CoV-2 (A) ssDNA or (B) RNA detection using the SPAD setup. The titration curve measured on the SPAD setup shows that as the concentration decreases, a lower intensity is detected (green dots). The limit of detection (purple dashed curve) results from the negative control (black curve) without the use of RNA or ssDNA with three times its standard deviation (grey dashed curve). Using the offset factors from **Section 3.2** the expected calibration curve can be determined (orange dashed curve) and its negative control (orange curve) with three times its standard deviation (orange dotted curve).

The detection of RNA and ssDNA measured using the SPAD setup was repeated 5 and 6 times respectively (**Figure 3.9**). For this purpose, the maximal value during the measurement was determined for each concentration. From the repetitions, the geometrical mean value and standard deviation was determined for each concentration, which is shown in the error bars. DCR is the mean value of all minimum values of the individual measurements.

The results show that at different concentrations (**Figure 3.9**) resulted in a higher but similar LODs ($\mathrm{LOD}_{\mathrm{ssDNA}} = 1.9 \cdot 10^9$ copies/ml, $\mathrm{LOD}_{\mathrm{RNA}} = 4.2 \cdot 10^9$ copies/ml) than the previously performed experiments on the plate reader (**Figure 3.8**).

Using the factor determined in **Section 3.2** and the titration curve of the plate reader, the expected calibration curve was determined (**Figure 3.9 A orange dashed curve**). The small distance between the expected calibration curve and the ssDNA titration curve (**Figure 3.9 A red dashed curve**) of the SPAD setup shows that the lower volume in the microfluidic does not limit the sensitivity of the ssDNA detection considerably.

When comparing the RNA titration curve (**Figure 3.9 B red dashed curve**) and the expected calibration curve (**Figure 3.9 B orange dashed curve**), it is striking that a lower LOD was achieved with the SPAD setup than is theoretically possible. This is possibly an error in the Labrox plate reader measurements, because unlike the SPAD setup, the Labrox plate reader determined an LOD several orders of magnitude lower in the RNA measurements.

Regardless of the assay used, the measured mean DCR ($< N_c >= 48$) represents the lower limit at which clear detection of photons can be differentiated (**Figure 3.9 blue curve**). According to this limitation, in the ideal case (sensitivity of the calibration curve at the DCR level), a $\mathrm{LOD}_{\mathrm{ssDNA}} = 1.8 \cdot 10^5\ \mathrm{copies/ml}$ is possible and would thus be acceptable according to WHO definition.

3.5 SPAD Setup Monte Carlo Simulation

It is possible to further increase the sensitivity of the measurement system and the SPAD array detector by adjusting certain parameters. For this purpose, Monte Carlo simulations were performed in the following sections.

Generally, during a chemiluminescence measurement, the chemiluminescent substrate converted at the biosensor is catalytically oxidized in the presence of H_2O_2 and produces a chemiluminescent emission uniformly distributed in all directions (**Figure 3.10**). Therefore, only half of the generated radiation is emitted in the direction of the detector and is detectable at all (**Figure 3.10 b**). When this radiation encounters a material transition, it is refracted depending on the change in refractive index (**Figure 3.10 a**) and, above a certain critical angle, total reflection occurs (**Figure 3.10 c**). The fraction of photons arriving at the detector depends on the distance traveled. In order to investigate the influences of these parameters on the design of the setup, a Monte Carlo simulation was developed, which is more flexibly adjustable compared to an analytical model. [76]

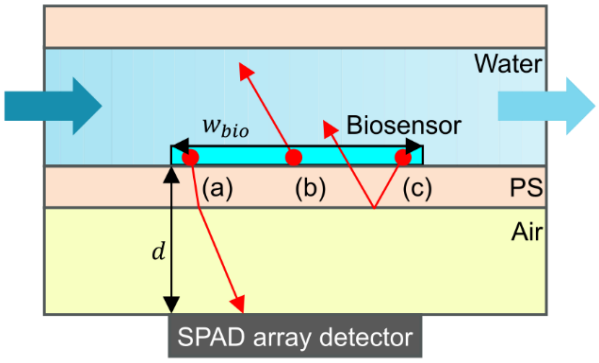

Figure 3.10: Schematic model illustrating the influences, for the detection of luminescence photons in the current setup: Number of generated photons, parameters of the detector, material transitions and respective layer thicknesses. The generated photons radiate equally distributed in all directions, half of them do not radiate in the direction of the detector (b), a part is totally reflected depending on the angle of incidence (c) and at the intermediate layers the photons are refracted (a).

The Monte Carlo simulation was performed by randomly positioning a large number of photons equally distributed on the circularly simplified biosensor (**Figure 3.11**). The generated photons also receive two random spatial angles each in order to achieve an equally distributed emission in all spatial directions. However, since it is known that only half of the photons are directed towards the detector, the spatial angles were limited to half a sphere in the direction of the detector. This can save half of the photons generated and thus increase the speed of the simulation.

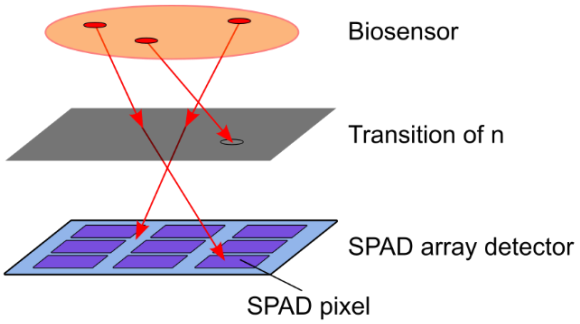

Figure 3.11: Representation of the developed simulation model. Configurable variables (distances, number of photons, number of intermediate layers and their refractive indices, detector specifications) allow the determination of optimal parameters.

Between the biosensor and the detector intermediate layers can be generated in adjusted height and refractive indices, at which reflection and refraction occur. In case of refraction, the new angle is obtained by the refraction law ($n_2 \sin\theta_2 = n_1 \sin\theta_1$). If reflection occurs ($\alpha_{\max} = \arcsin(n_2/n_1)$), the photon is removed from the list of all generated photons. The final position of all generated photons is on the plane of the detector. If the position is within one of the SPAD pixels in the detector, the photon is considered detected. Since only the fraction of the detected photons is evaluated here, the temporal aspect is neglected and the position of all photons is calculated simultaneously in parallel. [76]

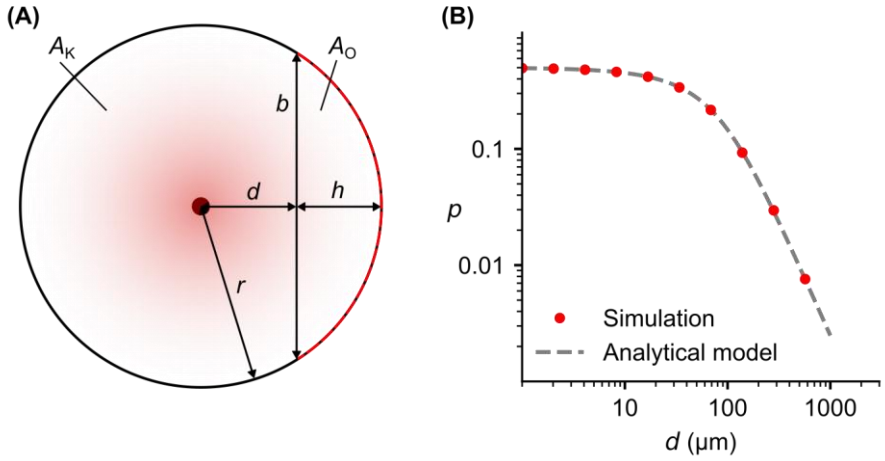

Figure 3.12: Analytical model and its verification:
(A) Schematic illustration of the compared analytical model.
(B) Proportion of detected photons as a function of distance for an analytical simplified model (grey dashed) and the Monte Carlo simulation with equivalent settings (red dots)

To verify the developed Monte Caro simulation, a simplified analytical model was created. The model assumes a point source where the radiation propagates spherically with radius r and only the spherical segment with height h is detected at the detector. The width of the detector and diameter of the spherical segment with b and the distance of the biosensor point to the detector with $d = r - h$, with a spherical area of $A_K = 4\pi r^2$ and an area of the spherical segment of $A_O = 2\pi rh$ [77] give the fraction of photons arriving on the detector:

$$p = \frac{A_O}{A_K} = \frac{h}{2r} = \frac{1}{2}\left(1 - \frac{d}{\sqrt{d^2 + \left(\frac{b}{2}\right)^2}}\right) \quad (3)$$

A good agreement between the two methods can be seen when the simulation is adjusted to match the simplifications of the analytical model (**Figure 3.12**). The advantage of the numerical model, however, is that many parameters, such as the dimensions of the biosensor and the arrangement of the detector, as well as the refraction for different materials and thicknesses, can be studied.

3.6 SPAD-Chip Specifications

The SPAD setup developed here uses a cartridge containing a biosensor in a microfluidic and a reusable base station with a detector and readout electronics. The advantage of this setup is the small biosensor size and the small volume required, reducing size and complexity compared to multi-well-based systems. However, the smaller volume also reduces the number of photons emitted at the biosensor, which is why it is necessary that the majority of the generated photons are detected for sufficient sensitivity of the system.

The size of the biosensor has to be chosen in such a way that most of the emitted chemiluminescence reaches the detector, otherwise the reagents are not used effectively. For this reason, the Monte Carlo simulation developed in **Section 3.5** was used to investigate the influence of the pixel diameter (**Figure 3.13 A**) and number of pixels (**Figure 3.13 B**) in relation to the biosensor diameter (**Figure 3.13 C**) on the proportion of detected photons. For higher comparability, the used fill factor, which describes the ratio between the photo-sensitive area and the total pixel area, of the simulated SPAD array detectors was set to 64 % and only in **Figure 3.13 E** material transitions with refraction and reflection were simulated.

Figure 3.13 A shows the percentage of detected photons as a function of the distance of the biosensor to the detector for a 10x10 pixel array for different pixel diameters, where the biosensor diameter was set constant to $d_{\mathrm{Biosensor}} = 10\ \mu\mathrm{m}$.

At low distances, a limit of $p_{\max} = 50\ \%$ is reached even with large pixel diameters, since only half of the photons are emitted in the direction of the detector. With high distances a proportionality of $1/d^2$ is shown, but this proportionality starts with increasing pixel diameter at higher distances. It can be concluded that pixels with larger diameters can still detect most of the emitted photons even at higher distances. Therefore, for a pixel diameter of $d_{\mathrm{Pixel}} = 20\ \mu\mathrm{m}$, a fraction of 10% of the emitted photons can still be detected even at a distance of $d = 100\ \mu\mathrm{m}$. This proportion can be reached at a distance of about $d = 150\ \mu\mathrm{m}$ for a pixel diameter of $d_{\mathrm{Pixel}} = 30\ \mu\mathrm{m}$ and at a distance of about $d = 200\ \mu\mathrm{m}$ for a pixel diameter of $d_{\mathrm{Pixel}} = 40\ \mu\mathrm{m}$. Thus, with increase in pixel diameter, the achievable distance also increases proportionally. Since the DCR of a SPAD array pixel increases with the area of the pixel [78] the diameter has to be chosen in a way that the required fraction of detected photons can be achieved and the DCR does not lead to loss of sensitivity. Since the sensitivity increases only slightly beyond the pixel diameter $d_{\mathrm{Pixel}} = 30\ \mu\mathrm{m}$, we set it to this value for the next simulations to keep the DCR as low as possible. The proportion of detected photons at a distance of $d = 100\ \mu\mathrm{m}$ as a function of the number of pixels (**Figure 3.13 B**) shows that the increase in the number of pixels from 1x1 to 10x10 leads to the highest increase in the proportion of 15 % and with further increasing pixel number this increase becomes gradually smaller. A pixel count of 20x20 requires four times the number of pixels compared to the pixel count of 10x10, but the percentage increases by only 7.4 %. Therefore, it can be assumed that a pixel number of 10x10 is sufficient to detect the majority of the photons. The Monte Carlo simulations also show that the biosensor diameter only has a clear influence on the proportion of detected photons when the biosensor diameter exceeds that of the entire detector (**Figure 3.13 C**). Therefore, to ensure the highest possible sensitivity of the SPAD setup, the biosensor must not be larger than the detector.

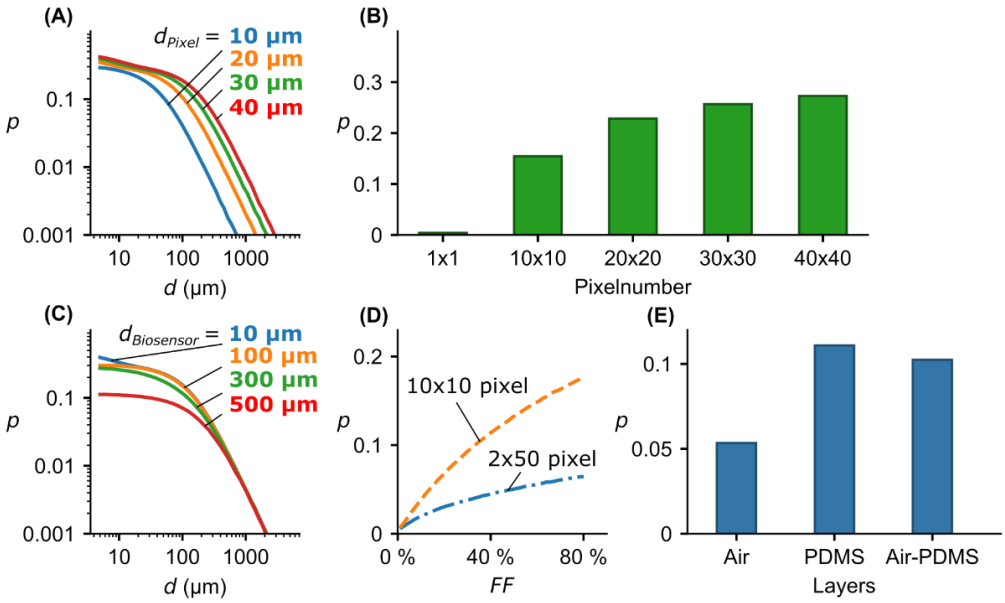

Figure 3.13: Optimal specifications for SPAD array detector and biosensor. Proportion of detected photons as a function of detector distance for **(A)** different pixel diameters (10 µm blue, 20 µm yellow, 30 µm green, 40 µm red), **(B)** for different number of pixels at a fixed distance of 100 µm to the biosensor, **(C)** biosensor diameter (10µm blue, 100 µm yellow, 300 µm green, 500 µm red) for constant detector size, **(D)** fill factor for different pixel arrangements (10x10 pixels dashed orange, 2x50 blue dot-dashed), **(E)** different materials between biosensor and detector.

Depending on the fill factor of the SPAD array detector a certain proportion of the photons incident on the SPAD array detector will arrive at the non-sensitive area. The fill factor depends on how much space must be used between each SPAD for any interconnects and Complementary metal–oxide–semiconductor (CMOS) circuitry for data pre-processing. With a pixel arrangement of two parallel rows, it is possible to achieve a high fill factor by leading lines and CMOS circuits away and placing the SPADs as close to each other as possible. However, with this pixel arrangement, the proportion of photons arriving outside the pixel area also increases. Simulation of two different pixel arrangements (**Figure 3.13 D**, 10x10 and 2x50) with the same number of pixels for a distance to the biosensor of $d = 100\ \mu m$ shows that a 2x50 pixel arrangement does reach only a fraction of detected photons of 6 % even with a high fill factor of 80 %. The 10x10 pixel array, on the other hand, achieves this proportion at a fill factor of 30 % and at a fill factor of 80 % even

a proportion of detected photons of 17 % can be achieved. Since the fill factor has a major influence on the proportion of detected photons, it should be set as high as possible in order to detect as many photons as possible. This can be made possible by moving CMOS circuits outside the pixel area.

However, in reality, the emitted photons have to pass through several layers on their way from the biosensor to the detector, which influence the beam path by refraction, reflection and absorption. Since transparent materials are usually used for this purpose, absorption is neglected in the studies carried out here. The highest losses of photons are caused by refraction and reflection at the transition between two different materials, which depend on the refractive indices and layer thicknesses of the two materials.

The SPAD setup used here has air between the PS film of the microfluidic and the SPAD array detector, with a high refractive index transition ($n_{\mathrm{PS}} = 1.59$ @ $587.6\ \mathrm{nm}$ [79] to $n_{\mathrm{Air}} = 1$). This causes most of the incoming photons to be reflected (**Figure 3.13 E, left**). With an intermediate layer of polydimethylsiloxane (PDMS) ($n_{\mathrm{PDMS}} = 1.44$ @ $532\ \mathrm{nm}$ [80]) it is possible to increase the fraction of incoming photons by a factor of two (**Figure 3.13 E, middle**). Once the cartridge has been inserted, it would probably be difficult to avoid air exposure, resulting in a thin air transition layer. The simulation results show that even with a thin layer of air between the two layers, the proportion of incoming photons is only slightly reduced (**Figure 3.13 E, right**). The optimization measures shown here can help to increase the proportion of detected photons and thus the sensitivity of the LoC measurement system.

These simulations results identified several optimal parameters to further improve the SPAD setup developed here. The SPAD array detector used consists of 8x8 SPAD pixels and has a pixel diameter of 30 µm with a distance between each pixel of about 60 µm and thus a fill factor of about 14 %. The pixel diameter and their number correspond approximately to the parameters that were also determined in the previous section and allow the detection of a high photon fraction (**Figure 3.13 A and B**). The fill factor, on the other hand, can be increased by reducing the spacing between pixels or by using microlenses [81], which should lead to a significant increase in sensitivity. A significant increase in sensitivity can also be

expected if the opening of the flex foil above the SPAD array detector is filled with a material of a refractive index comparable to that of the PS film, *e.g.* PDMS (**Figure 3.13 E**).

The comparison with another developed SPAD setup [82] is difficult because it was used in conjunction with fluorescence. Comparing of the DCR, which had a value below 8000 Hz for 70 % of the pixels there, to the SPAD array detector used here with a mean DCR of 48 Hz, show that the SPAD array detector used here, it is ideally suited for use as a chemiluminescence detector.

3.7 Conclusion

In this chapter, we have demonstrated the detection of SARS-CoV-2 RNA and ssDNA using a lens-free measurement setup developed here. The sensitivity defined as acceptable by WHO is technically achievable if the ideal LOD would be at the DCR level of the SPAD array detector used. However, the LOD determined from the measurements was also far above the currently available Ag-RDT and could not be obtained even with comparative measurements on a commercial plate reader. It can therefore be assumed that the determined LOD can be improved by optimizing the protocol used.

To further increase the sensitivity of the SPAD setup, Monte Carlo simulations were performed to identify the SPAD parameters with the greatest influence. These include the fill factor, which should be as high as possible (*e.g.* by using microlenses [81]), and the array arrangement of the SPADs, which could already detect a high photon fraction in the range of 10x10 pixels, while the total sensitive area being not larger than the biosensor. Reflection and refraction should also be reduced as much as possible, *e.g.* by using interlayers with the lowest possible refractive index differences.

4 Fluorescence Lifetime Measurements using SPAD Array Detector

Measuring the fluorescence lifetime (FL) has gained rising interest in the field of biomedicine with numerous applications such as studying molecular interactions [23,24], monitoring environmental parameters (pH [83–85], temperature [86], ion concentration [87]), and for multi-parametric bioassays [25]. FL is the average time a fluorophore remains in the excited state prior returning to ground state by emitting a fluorescence photon [8]. Compared to intensity-based fluorescence measurement, FL as an intrinsic material parameter has the advantage of being independent of fluorophore concentration and thus of intensity [88]. In addition, FL is very attractive for multiplexing in bioassays since it allows to distinguish between fluorophores with overlapping spectral properties based on their characteristic FL [89].

There are two main approaches to measure FL, either in time-domain or in frequency-domain [90]. FL measurements in the time-domain are advantageous over frequency-domain when for instance studying complex multi-exponential decays of the fluorescence signal [8]. In time-domain methods, *e.g.*, time-correlated single-photon counting (TCSPC), the sample is periodically excited by a short

light-pulse (*e.g.*, laser) and the arrival times of emitted fluorescence photons at a single-photon sensitive detector are recorded to reconstruct the temporal decay of the fluorescence intensity characterized by the FL [90]. However, precision and accuracy of FL determination strongly depends on the number of detected photons [91]. Since in conventional TCSPC the probability of photon detection is kept below one photon per measurement window to avoid an underestimation of the FL by the pile-up effect as a result of detector's dead time (typically tens of ns) [92], TCSPC is generally lacking of long measurement times. This is extremely crucial when it comes to highly dynamic applications such as flow cytometry [93] or high-speed imaging (FLIM) [94].

To overcome this limitation, in recent years different approaches have been proposed to reduce the detector's dead time such as hybrid photodetectors *i.e.,* vacuum tube-based electronic acceleration combined with avalanche diodes with dead times below 1 ns [95,96], or software-based dead-time corrections [97]. One further promising approach is using pixelated array detectors based on single photon avalanche diodes (SPADs) instead of conventional photomultiplier tubes (PMT) with "one-pixel" (*i.e.*, one photosensitive area) [21,97,98]. SPAD array detectors have the advantage that during one measurement window more than one photon can be detected. Hence, a shorter measurement time is needed to detect the same number of photons than using a "one-pixel" detector [99]. However, in this regard the question arises how are the correlations between photon statistics, number of pixels, time resolution and measurement time. We provide for the first time a comprehensive experimental and theoretical study on these correlations to extract the limits of SPAD array detectors for FL measurements. It could be shown that a SPAD array detector with only 30 pixels is necessary to record ns-FL with high precision and accuracy within a measurement time down to one µs, demonstrating the great potential of SPAD array detectors for high-speed FL applications. This measurement time is limited by the data rate to be read out, which is below $1\,\mathrm{Gbit/s}$ for 1000 pixels and FLs with $\tau \geq 3\,\mathrm{ns}$. To ensure continuous data transmission and FL determination, the data rate must not exceed a certain value depending on the given system.

4.1 Pile-Up Background

In TCSPC, due to the Poissonian nature of photon statistics and experimental noise, the intrinsic FL of a fluorophore (**Figure 4.1 A**) can only be determined with a certain accuracy. To give a fundamental understanding of the measurement principle in TCSPC and how the accuracy is affected by the count rate, we exemplary illustrated the determination of FL at relatively high photon rate for a “one-pixel” single-photon detector such as a PMT [100] (**Figure 4.1 C**) and a “pixelated” SPAD array detector (**Figure 4.1 D**).

In TCPSC, the temporal decay of the fluorescence intensity is obtained by detecting arrival times of single photon events emitted by a fluorophore after short-laser pulse excitation (**Figure 4.1 B**) and sorting the events in a histogram from which the FL is determined by curve fitting (**Figure 4.1 C, D**).

With a “one pixel” single-photon detector only one photon per laser excitation cycle can be detected (**Figure 4.1 C**). One cycle is declared as measurement window n_{w}, with the duration t_{w} throughout the paper.

This photon count limitation makes TCSPC to a cumbersome method because the count rate has to be adjusted by tuning the laser power so that the probability to detect a photon is below one photon per measurement window. If count rates are higher than the number of pixels, photons are missed by the detector. In this case, only the fastest photons are detected (**Figure 4.1 Ci-ii**). This so-called "first photon" problem causes a pile-up of the histogram (**Figure 4.1 Ciii**), resulting in a lower accuracy of FL acquisition. This problem is well known from literature [98,101]. Several methods have been developed to back-calculate the pile-up [97,102]. However, the use of these methods is limited, *e.g.*, for multiexponential decays with multiple fluorophores, information on the fractions in which the fluorophores are present is required.

With a “pixelated” SPAD array detector, the higher number of pixels allows for higher photon rates, so in the example shown, FL detection is less affected by pile-up than in a "single pixel" single photon detector (**Figure 4.1 Diii**). It is worth to mention, that with such SPAD array detector, less time is needed to collect a sufficient number of photons. In simple terms, if one pixel is dead due to photon hit, the

second one is still active to catch an additional photon. However, it remains to be investigated how the pile-up is related to the number of pixels and what measurement speed can be achieved with a given number of pixels.

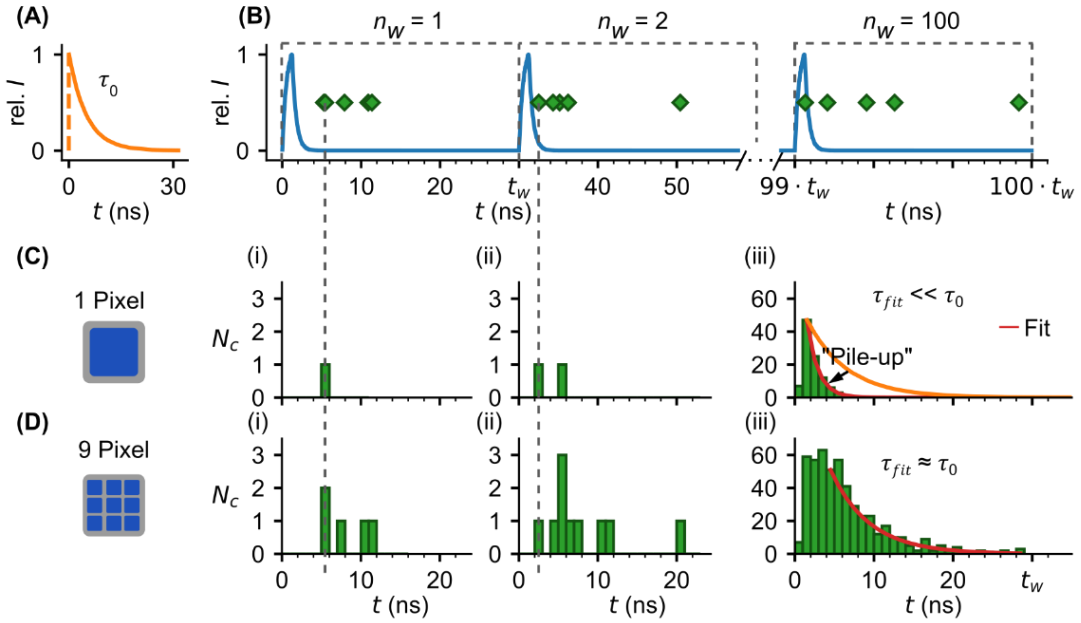

Figure 4.1: TCSPC-based FL measurements using SPAD array detector. (A) "Ideal" fluorescence signal (intensity vs. time) of a fluorophore with a single-exponential decay characterized by its lifetime τ_0. **(B)** Lifetime measured by TCSPC. Fluorophores are excited with a short laser pulse (blue curve) and the arrival times of emitted fluorescence photons (green markers) are detected by a single-photon detector, $e.g.$, PMT or SPAD array detector. To get a sufficient number of arrival times, laser excitation and photon counting are repeated for n_w-times with a defined measurement window duration t_w. All arrival times are stored in a histogram allowing to extract the lifetime by exponential fit (Ciii and Diii). The count rate during each measurement window depends on the number of individual photosensitive areas or pixels of the detector **(C and D)**. With "one pixel" single-photon detector, only the first photon per measurement window can be detected (Ci-ii). In case of high photon rates (photons per measurement window), this "first-photon"-issue leads to a pile-up of the histogram and an underestimation (lower accuracy) of the lifetime as indicated by difference between the fit (red curve) and ideal fluorescence signal (orange curve from (A)) (Ciii). To avoid pile-up the photon rate should be smaller than the number of pixels. With "pixelated" SPAD array detector higher photon rates can be permitted ((D), here, pixels $= 9 >$ photon rate $< N_c >_w = 5$) resulting in higher total counts and a more accurate estimation of the lifetime (Diii) compared to one pixel (Ciii) after the same number of measurement windows (*i.e.*, same total measurement time).

4.2 SPAD Array Detector Setup

FL measurements were carried out using a custom-built setup based on a 192 × 2 pixel CMOS SPAD array detector, which was developed by the Fraunhofer IMS and has a time resolution of 312.5 ps [62] (***cf.*** **Figure 4.2**).

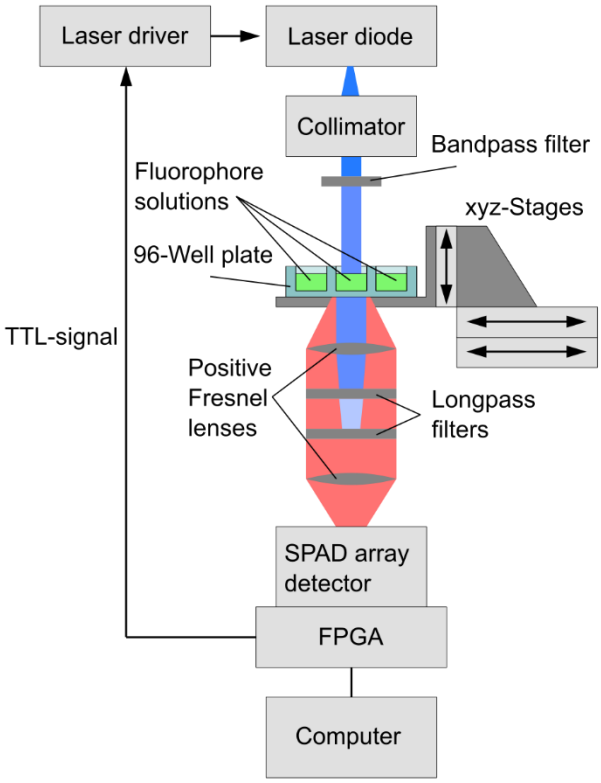

Figure 4.2: Schematic of the experimental FL setup. The is excited by a collimated pulsed laser diode ($\lambda = 450\ nm$), filtered by a bandpass filter. The emitted fluorescence is collected and focused onto the SPAD array detector by two positive Fresnel lenses. Longpass filters were used to filter out residual signal from the pulsed laser diode. A FPGA board was used to control trigger signals for laser and SPADs and to process the data from the SPAD array detector

Control and data readout of the SPAD array detector were realized with a FPGA-board. The sample was homogenously illuminated by a collimated pulsed laser diode with a wavelength ($\lambda = 450$ nm) (laser diode 720-PL450B, Mouser Electronics, US) filtered by a bandpass filter (BP 445/50, Carl Zeiss Microscopy LLC, US).

Laser pulses with a Full Width at Half Maximum (FWHM) = 1.25 ns) and a turn-off time of 0.5 ns were generated by a laser driver (iC-HG (HG8M), iC-Haus, Germany). The laser driver was also controlled by the FPGA-board. Positive Fresnel lenses (FRP125, FRP0510, Thorlabs, US) were mounted between sample and SPAD array detector to collect the fluorescence photons. In addition, longpass filters (#84-737, Edmund Optics, UK, cut-off wavelength 475 nm and FELH0500, Thorlabs, US, cut-off wavelength 500 nm) in front of the SPAD array detector were used to filter out the laser beam (**Figure 4.3 A**). Three stages (*xy*-direction: V-508 PIMag®; *z*-direction: M-122.2DD1, Physik Instrumente, Germany) allow to precisely position a 96-well plate with the fluorophore sample solution under the laser beam (**Figure 4.3 B**).

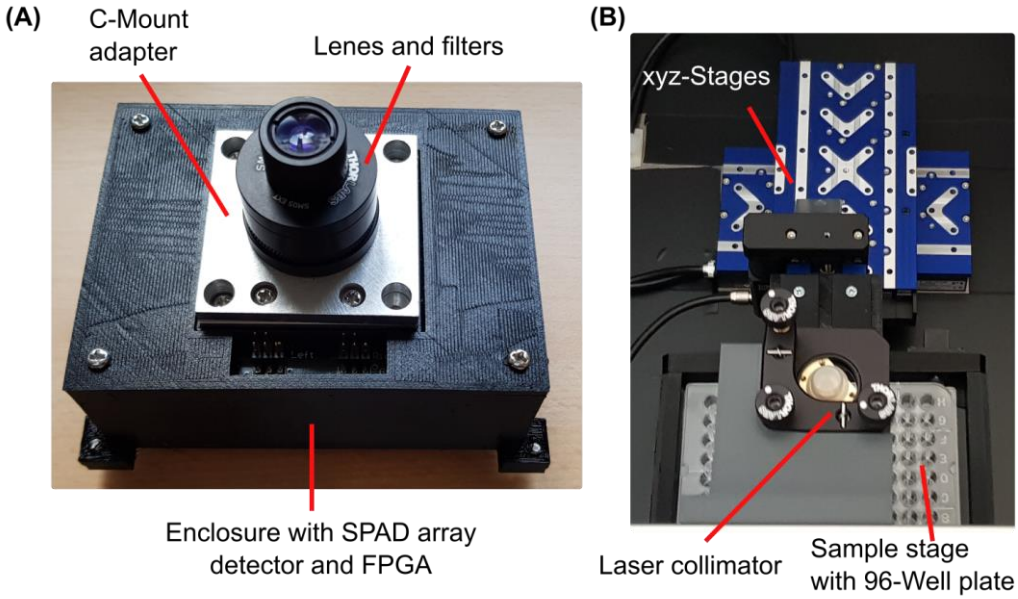

Figure 4.3: Images of the experimental FL setup:
(A) Detector: SPAD array detector with the lenses and filters attached in a tube housing mounted via a C-mount adapter.
(B) Measurement setup: Top view of the measurement setup with the laser and collimator mounted on top, the optical path of which is directed to a well in the underlying 96-well plate, adjustable in 3 axes by three stages. The SPAD array detector from (A) is located below the illuminated well.

During one measurement laser trigger and SPADs are repeatably turned on and off (**Figure 4.4 A**). In total one measurement was composed of 30,000 measurement windows. Each detected photon during the measurement windows has a specific arrival time. All arrival times are stored in a histogram to extract the FL by nonlinear least square (LS) fitting (**Figure 4.4 B**).

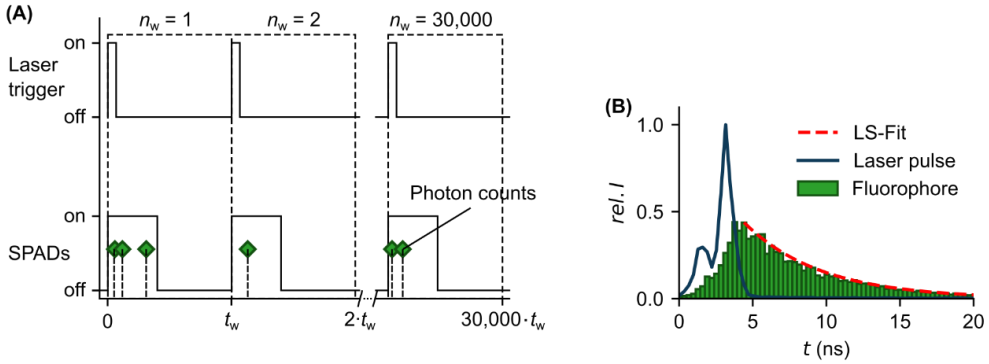

Figure 4.4: Experimental FL measurement.
(A) Timing scheme of the measurement procedure: Laser trigger and SPADs were turned on and off during one measurement window. The total number of measurement windows was set to $\mathrm{n_w} = 30{,}000$. Each detected photon (green markers) during the on-phase of the SPADs has a specific arrival time.
(B) FL determination: Representative measurement curves for a laser pulse ($\mathrm{FWHM} = 1.25$ ns, blue curve) and for the resulting fluorescence signal (histogram of all arrival times, green) detected by the SPAD array detector. The exponential decay of the fluorescence signal was fitted by nonlinear least square (LS) method to determine the FL (red dashed curve).

4.3 Used Fluorophores

Following fluorophores were used in FL experiments: lucifer yellow (L0259, Merck, Germany), acriflavine (01673, Merck, Germany), 2-amino-acridone (06627, Merck, Germany), fluorescein (46955, Merck, Germany). They were solved in deionized water. The final concentrations in solution were $c = 15.6\ \mu\mathrm{M}$ and $c = 3.9\ \mu\mathrm{M}$ for 2-amino-acridone, fluorescein, acriflavine and for lucifer yellow, respectively in this chapter.

4.4 Fluorescence Lifetime Monte Carlo Simulations

The experimental FL measurements were validated by a self-written single-photon statistic-based Monte Carlo simulation in Python (**Figure 4.5**).

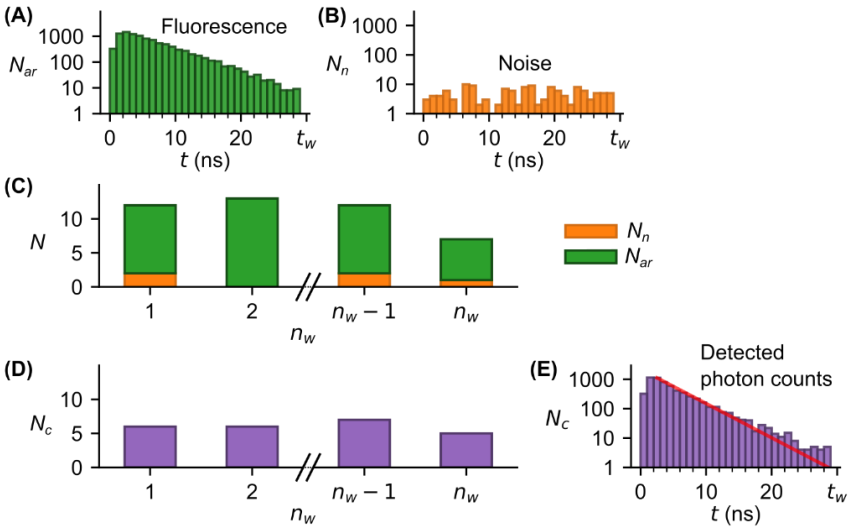

Figure 4.5: Principle of FL Monte Carlo simulation.
(A) Fluorescence photons: Distribution of fluorescence photons N_{ar} arriving at the detector. The distribution was obtained by convolving the turn-off function of the laser pulse and the exponential fluorescence decay of the fluorophore.
(B) Noise: Distribution of events that arise from noise sources N_{n} such as dark counts and scattered light.
(C) Distribution: Number of arrived photons per measurement window (randomly Poisson-distributed over all measurement windows).
(D) Detected photons: Number of detected photons per measurement window. Since only one photon can be detected per pixel and measurement window, only the fastest photons are detected.
(E) FL determination: Distribution of all detected photons from that the FL is determined by LS fitting.

In the FL simulation, for each measurement window an excitation laser pulse induces a Poisson-distributed random number of emitted fluorescence photons. Thereby, the laser pulse characteristics (width and falling edge) were considered (**Figure 4.5 A**). This number corresponds to the mean photon counts per measurement window $< N_{\mathrm{c}} >_{\mathrm{w}}$ that would be detected without the occurrence of pile-up, which will be referred to here as count rate. Each generated photon has its

characteristic arrival time at the SPAD array detector. In addition to the fluorescence photons, randomly events at the detector from noise sources (dark count rate (DCR), scattered light) were generated (**Figure 4.5 B**). All generated arrival times and noise events were Poisson distributed among the measurement windows n_{w} (**Figure 4.5 C**) and then evenly distributed among the pixels of the detector. In our simulation, each pixel can only count one photon per measurement window, which means that not all generated signals are counted (**Figure 4.5 D**). All counted photons N_{c} are stored in a histogram to determine the FL (**Figure 4.5 E**).

4.5 Statistical Analysis

The FL was determined from the histograms by LS fit with the following fit function for the detected intensity I during time t

$$I = I_0 e^{-\frac{t}{\tau_{\mathrm{fit}}}}, \tag{4}$$

where I_0 and τ_{fit} are the fit parameter for the intensity at time $t = 0$ and the FL, respectively. We calculated the coefficient of variation

$$c_{\mathrm{v}} = \frac{\sigma}{\langle \tau_{\mathrm{fit}} \rangle}, \tag{5}$$

with the arithmetic mean $< \tau_{\mathrm{fit}} >$ and standard deviation σ from multiple measurements ($N = 100$). The obtained c_{v}-values at three different sample positions were averaged to one representative mean value for the precision of FL acquisition $\bar{c}_{\mathrm{v}}$. From the fit parameter τ_{fit} and characteristic FL of the fluorophore τ_0, we calculated the relative error

$$\delta\tau = \langle \frac{|\tau_{\mathrm{fit}} - \tau_0|}{\tau_0} \rangle \tag{6}$$

from multiple measurements ($N = 100$). The obtained $\delta\tau$-values at three different sample positions were averaged to one representative mean value for the accuracy of FL acquisition $\overline{\delta\tau}$. Since c_{v} and $\delta\tau$ approximately followed a log-normal distribution, $\bar{c}_{\mathrm{v}}$ and $\overline{\delta\tau}$ were calculated as geometric means. Error bars represent (geometrical) standard error of mean (**Figure 4.6 A; Figure 4.7,Figure 4.8; Figure 4.11 Bi**). Data analysis were carried using self-written procedures in Python.

4.6 Photon Statistics

Since the FL determination underlies Poisson statistics, it can only be determined with a certain precision. For this reason, several FL measurements are usually performed in experiments to obtain robust values for the population mean and the standard deviation for the FL of each fluorophore. This is especially important in multiplexing applications aiming to distinguish between different fluorophores (**Figure 4.6**) [91].

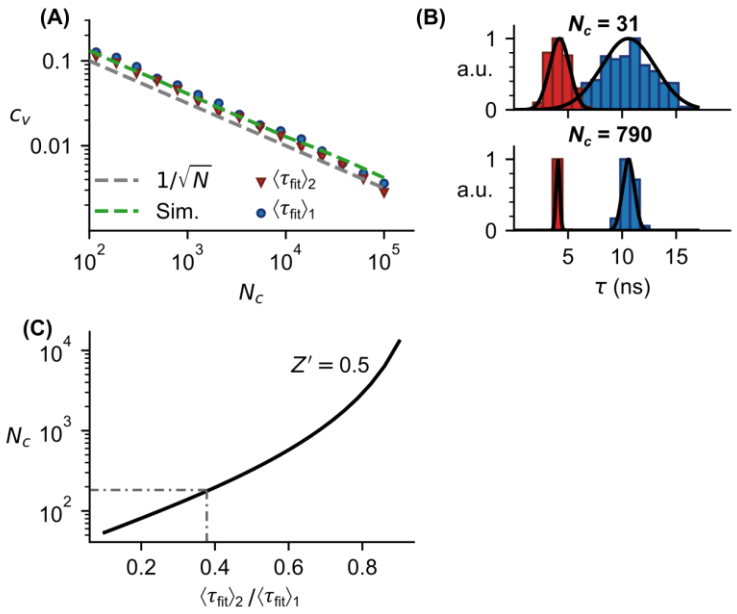

Figure 4.6: Photon statistics in FL measurements.
(A) Precision: Precision vs. photon counts. Experimental FL measurements of two fluorophores (2-amino-acridone, red and fluorescein, blue) and Monte Carlo simulations (green dashed curve) with a corresponding $1/\sqrt{N_c}$ curve (gray dashed curve).
(B) Distribution: Representative distribution of FLs at low N_c (upper panel) and high N_c (lower panel) for the two fluorophores shown in (A) with different standard variations σ, for the same mean values μ.
(C) Differentiation: Successful differentiation requires a sufficient distance between these two distributions, which can be achieved for $Z' = 0.5$ (**Equation 9**), corresponding to a distance of 6 of the standard deviation for each fluorophore. Such a distance is described in [103] as an excellent assay, and the number of counts required compared to the ratio of the mean values of two FLs to achieve this is shown here. The grey dashed/dotted line indicates the minimum required photon counts for distinguishing the fluorophores in (A, B). Error bars in (A) are smaller than the markers.

We carried out FL measurements using the FL measurement setup described in **Section 4.2** on two different fluorophores and obtained a mean FL of $\langle\tau_{\mathrm{fit}}\rangle_1 = 10.6\ \mathrm{ns}$ and $\langle\tau_{\mathrm{fit}}\rangle_2 = 4.1\ \mathrm{ns}$ for 2-amino-acridone and fluorescein, respectively. These values are in good accordance to the literature (2-amino-acridone in water: $\tau \approx 10\ \mathrm{ns}$ [104], fluorescein in PBS at $\mathrm{pH} = 8$: $\tau = 3.99\ \mathrm{ns}$ [105]).

For the two fluorophores (2-amino-acridone and fluorescein) with the experimentally obtained FLs and following Monte Carlo simulations with a FL of $\tau = 5\ \mathrm{ns}$, we determined the precision given by the mean coefficient of variation $\bar{c}_{\mathrm{v}}$ at different photon counts (**Figure 4.6 A**). It could be shown that independently from the absolute FL value, $\bar{c}_{\mathrm{v}}$ depends on the photon counts with $1/\sqrt{N_{\mathrm{c}}}$ as expected since photon counting in FL measurements underlies Poisson statistics. Larger photon counts result in lower values for $\bar{c}_{\mathrm{v}}$ and hence in a more precision FL determination. This coincides with Monte Carlo simulations for $\tau = 5\ \mathrm{ns}$ (**Figure 4.6 A**).

Histograms of FL distributions at two different photon counts for the two fluorophores (2-amino-acridone and fluorescein) show that at relatively low photon counts (corresponding to high c_{v}), the distributions overlap while at high photon counts (corresponding to low c_{v}), the distributions are clearly separated (**Figure 4.6 B**). In high-throughput screening assay, typically the Z' factor is calculated to give a quantitative value for separation of two distributions and hence for the assay quality [103]

$$Z' = 1 - \frac{(3\sigma_1 + 3\sigma_2)}{|\langle\tau_{\mathrm{fit}}\rangle_1 - \langle\tau_{\mathrm{fit}}\rangle_2|}, \tag{7}$$

with the standard deviations $\sigma_{1,2}$ the mean values $\langle\tau_{\mathrm{fit}}\rangle_{1,2}$.
From **Figure 4.6 A** we derived that c_{v} is approximately inverse proportional to the square root of the photon counts [21,91].

$$c_{\mathrm{v}} \approx \frac{1}{\sqrt{N_{\mathrm{c}}}} \tag{8}$$

Inserting **Equation 7** in **Equation 8** and rearranging to the photon count gives following relation for $\langle\tau_{\mathrm{fit}}\rangle_1 > \langle\tau_{\mathrm{fit}}\rangle_2$:

$$N_c = \left[\frac{3}{(1-Z')}\left(\frac{1+\frac{\langle\tau_{\mathrm{fit}}\rangle_2}{\langle\tau_{\mathrm{fit}}\rangle_1}}{1-\frac{\langle\tau_{\mathrm{fit}}\rangle_2}{\langle\tau_{\mathrm{fit}}\rangle_1}}\right)\right]^2 \tag{9}$$

For $Z' \geq 0.5$, the distributions are sufficiently separated, clarified as an excellent assay according to [103]. For example, with $Z' = 0.5$, which corresponds to a distance of 6 of the standard deviation for each fluorophore, this gives $N_{\mathrm{c}} = 184$ for the two fluorophores 2-amino-acridone and fluorescein with a ratio of $\langle\tau_{\mathrm{fit}}\rangle_2/\langle\tau_{\mathrm{fit}}\rangle_1 = 0.39$.

However, many of the commercial fluorophores used have very similar FLs, which means that the resulting ratio of $\langle\tau_{\mathrm{fit}}\rangle_2/\langle\tau_{\mathrm{fit}}\rangle_1$ is low and, based on the result shown here, a correspondingly large number of photon counts are required for successful differentiation. To keep the measurement time short, the required photon counts should be acquired as fast as possible, but this is limited due to the pile-up effect introduced in **Section 4.1**.

4.7 Pixel Dependency in FL Acquisition

To evaluate the pile-up effect introduced in **Section 4.1**, we carried out FL measurements on a fluorophore (acriflavine) while adjusting the fluorescence intensity by using neutral density filters (NDUV01A to NDUV40A, Thorlabs, US) in front of the SPAD array detector. This allowed us to determine the mean FL at different mean photon counts per measurement window (**Figure 4.7**).

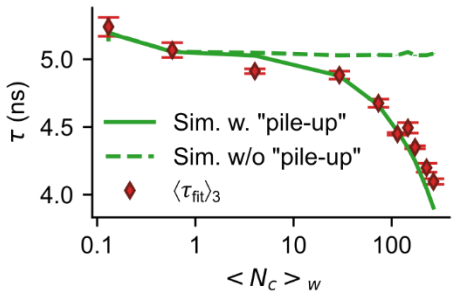

Figure 4.7: Impact of the detector's pile-up on the FL. Lifetime vs. count rate $\langle N_c \rangle_w$. Experimental FL measurements (red markers) and Monte Carlo simulations with pile-up (green solid curve) and without pile-up (green dashed curve) for a SPAD array detector.

At low count rates ($\langle N_c \rangle_w < 10$) the determined FL remains roughly constant ($< \tau_{fit} >_3 \approx 5$ ns). Beyond that, with increasing count rates the determined FL deviates significantly from the FL at low count rates, which is confirmed by a following Monte Carlo simulation (green solid curve, **Figure 4.7**). If we carry out the simulation without taken the pile-up into account, the resulting FL stays constant independently of the count rate (green dashed curve, **Figure 4.7**). It has to be mentioned that in the simulation we assumed that all pixels see the same count rate. However, this was not the case in the FL experiments due to the gaussian nature of the laser's beam profile. Therefore, only SPAD pixels illuminated with at least $50\ \%$ of max. intensity (photon counts) were considered (*i.e.*, 233 of the $2\text{x}192$ active SPAD pixels). To show the pile-up's influence independently of the absolute FL and considering the pixel number, we determine the relative accuracy $\delta\tau$ (**Equation 6**) as a dimensionless value (**Figure 4.8**).

Similar to the dependency of the precision (**Figure 4.7 A**), the relative accuracy initially decreases with increasing photon counts (**Figure 4.8 A-C, upper x-axis**) according to $1/\sqrt{N_c}$ (**Figure 4.8 A-C, grey dashed curve**), while keeping the number of measurement windows constant at $n_w = 30{,}000$. In contrast to the precision, the relative accuracy starts to increase again at a specific level of total counts. This level corresponds to a certain count rate

$$< N_c >_w = N_c / n_w \,. \tag{10}$$

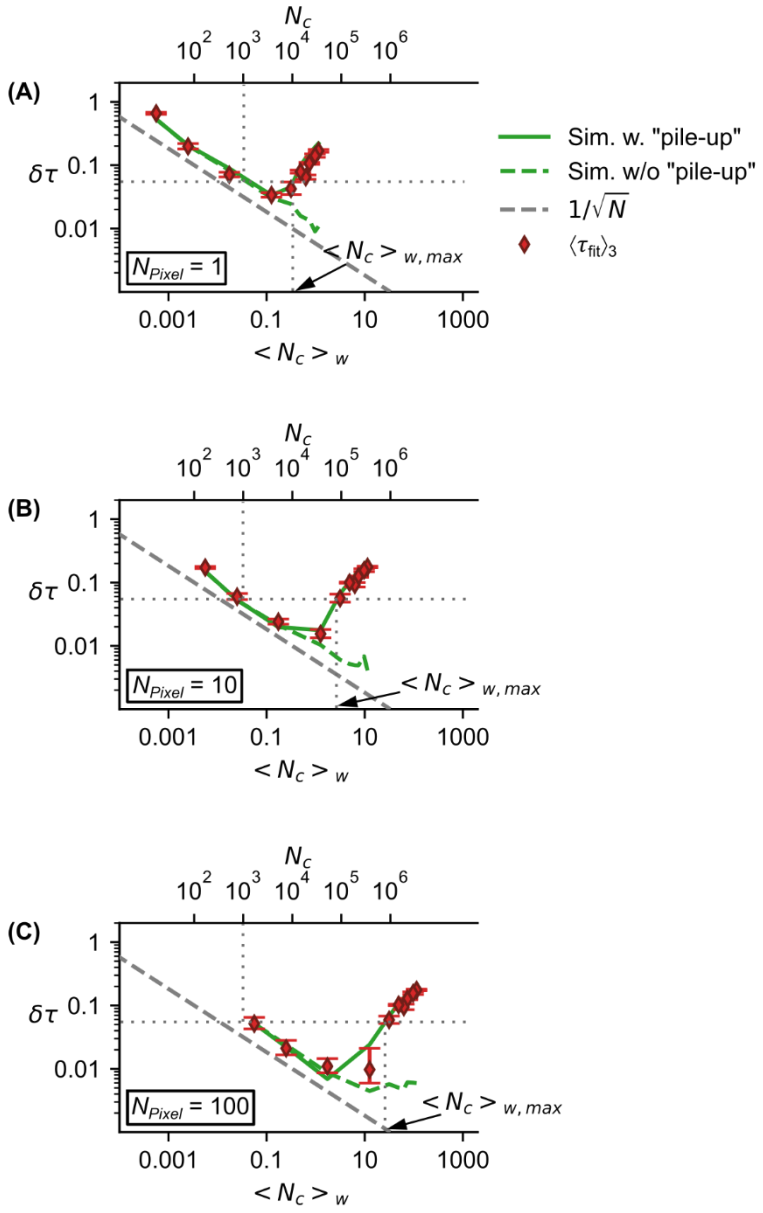

Figure 4.8: Impact of the detector's pile-up on relative accuracy of determined FL. Relative accuracy $\delta\tau$ of the measured lifetime τ vs. count rate $\langle N_c \rangle_w$ for different number of the SPAD array detector's active pixels (**(A)**, 1 pixel; **(B)**, 10 pixels; **(C)**, 100 pixels). At a relative accuracy of $\delta\tau = 5.5$ %, corresponding to a photon count of $N_c = 1000$, this results in a maximum count rate $\langle N_c \rangle_{w,max}$ that depends on the number of pixels (dotted lines).

The different behavior of the precision and relative accuracy is to be expected, since the precision is given by the coefficient of variation solely depends on the photon counts while the accuracy is of course affected when the detector's pile-up leads to an underestimation of the absolute FL.

However, the effect of pile-up is negligible when the accuracy of the FL determination is mainly limited by Poisson statistic, which achieves a relative accuracy of $\delta\tau = 5{,}5\ \%$ for photon counts of $N_\mathrm{c} = 1000$, regardless of the pixel number (**Figure 4.8 A-C**). This accuracy is reached by the pile-up only at a maximum count rate $\langle N_\mathrm{c}\rangle_\mathrm{w,max}$, which depends on the number of pixels (**Figure 4.8 A-C**). Since the experimentally accessible $\langle N_\mathrm{c}\rangle_\mathrm{w,max}$-values for different pixel numbers is in our case strongly limited, we carried out Monte Carlo simulations for a large number of different pixel numbers and show that there is a linear correlation between $\langle N_\mathrm{c}\rangle_\mathrm{w,max}$ and N_Pixel (**Figure 4.9**).

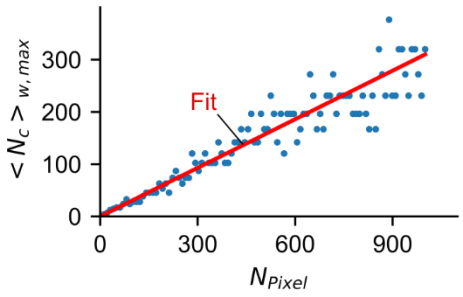

Figure 4.9: Pixel dependent count rate: $\langle N_\mathrm{c}\rangle_\mathrm{w,max}$ vs. N_Pixel determined from Monte Carlo simulations show a linear correlation. The fluctuations of the values are the result of system limitations on which the simulations were performed.

From the line fit (**Figure 4.9, red line**), we obtain a maximum count rate of $< N_\mathrm{c} >_\mathrm{w,max} = 0.31$ per pixel (for $N_\mathrm{c} = 1000$ and $n_\mathrm{w} = 30{,}000$). Assuming one pixel, this value is comparable to the count rate of an ideal PMT of 0.37 [95], but this is still higher than the maximum count rate normally used in TCSPC of 0.1 to 0.2 [98]. This shows that the use of a SPAD array detector for fast determination of FL is superior to a PMT even with a small number of pixels (>2 pixels).

4.8 Total Measurement Time and Data Rate

In order to perform a fast FL determination, it is necessary to detect as many photons in the shortest possible time. However, as discussed in **Section 4.7**, this is not trivial since only a maximum mean count rate is possible before pile-up affects the determined FL. Another factor influencing the measurement time is the duration of a single measurement window, which should also be short as possible, but so long that almost all emitted photons arrive on the detector within the measurement window. Otherwise, "slow" photons could be detected in the subsequent measurement window as "fast" photons. Many standard fluorophores, such as those used in this paper, display a single exponential decay

$$I = I_0 e^{-\frac{t}{\tau}} \tag{11}$$

with the Intensity I_0 at time $t = 0$.
The percentage of emitted photons from the fluorophore f after a laser pulse excitation can be extracted from

$$f = \frac{N_{\Delta t_\mathrm{w}}}{N_\mathrm{All}} = \frac{\int_0^{\Delta t_\mathrm{w}} I}{\int_0^{\infty} I} = \frac{\left[I_0(-\tau)e^{-\frac{t}{\tau}}\right]_0^{\Delta t_\mathrm{w}}}{\left[I_0(-\tau)e^{-\frac{t}{\tau}}\right]_0^{\infty}} = 1 - e^{-\frac{\Delta t_\mathrm{w}}{\tau}} \tag{12}$$

which is given by the ratio of the number of emitted photons $N_{\Delta t_\mathrm{w}}$ and all photons N_All at set measurement window Δt_w.

According to this function, for a proportion of $99.9\ \%$ emitted photons a minimum duration of the measurement window is $\Delta t_\mathrm{w} = 7 \cdot \tau$ (**Figure 4.10 A**). It is unlikely that photons of the remaining 0.1% fraction will be detected after this time, so the next measurement window can start right after that.

Next to the duration of a measurement window, an important factor that has to be considered regarding the total measurement time is the read-out rate of the chip containing the SPAD array detector and evaluation circuitry. This is, among other factors, influenced by the chip's time-resolution since higher time-resolution means simplified more data in shorter time.

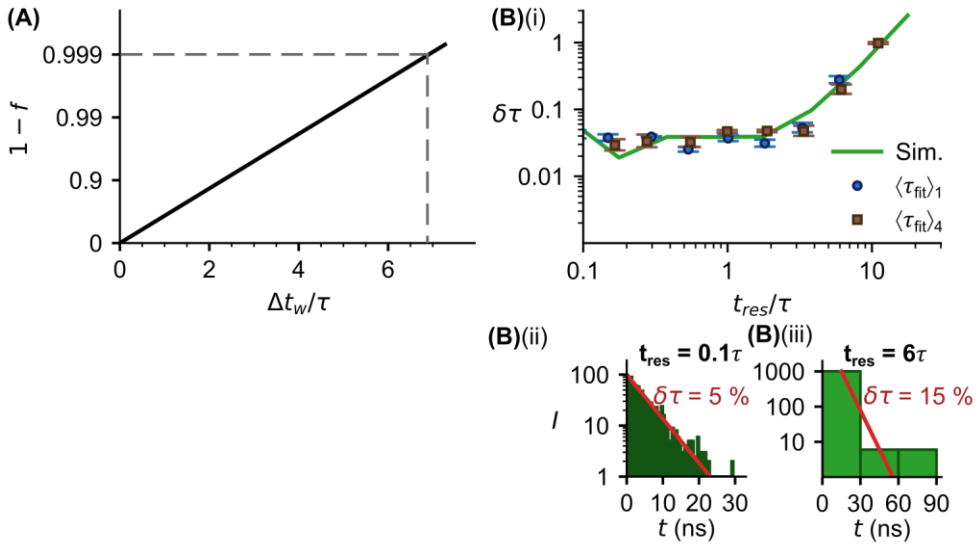

Figure 4.10: Required width of the measurement window duration and influence of the time resolution.
(A) Measurement window duration: Proportion of emitted photons that arrive at the detector within the measurement window duration t_{w} (normalized by the lifetime).
(B) Time resolution: (Bi) Relative accuracy of lifetime acquisition from fitting the histograms depends on the binning, *i.e.*, time resolution of the detector (for $N_{\mathrm{c}} = 1000$). Experimental measurements (blue and brown markers) and Monte Carlo simulations (green curve) with representative histograms for simulated data at a low time resolution of $t_{\mathrm{res}} = 6\tau$ (Bii) and at a high time resolution of $t_{\mathrm{res}} = 0.1\tau$ (Biii).

To evaluate how the accuracy of FL determination is affected by the time-resolution, we carried out FL measurements on two different fluorophores with the SPAD array detector's time-resolution of 312.5 ps. We obtained for 2-aminoacridone and for lucifer yellow a mean FL of $\langle\tau_{\mathrm{fit}}\rangle_1 = 10.6\ \mathrm{ns}$ and $\langle\tau_{\mathrm{fit}}\rangle_4 = 5.7\ \mathrm{ns}$, respectively. These values are in good accordance to the literature (2-aminoacridone in water: $\tau \approx 10\ \mathrm{ns}$ [104], lucifer yellow: $\tau = 5.29\ \mathrm{ns}$ [106]). In order to obtain lower time resolutions, the width of the time resolution was then resized afterwards during the evaluation of the measurement results (**Figure 4.10 Bi**).

It could be shown that, regardless of the absolute FL, the accuracy is approximately constant until the time resolution is smaller than two times the FL ($t_{\mathrm{res}} < 2\tau$) (**Figure 4.10 Bi**). For the line fit at least two bins with photon counts representing the single-exponential decay are required. If the time resolution is much larger than the FL, then most of the detected photon counts within the

second bin result from noise (*e.g.*, DCR, scattered light) and the relative accuracy decreases (**Figure 4.10 Bi**). To emphasize these findings, in **Figure 4.10 Bii and iii** two representative histograms for simulated data at a relatively high time resolution of $t_{\mathrm{res}} = 0.1\tau$, where photon counts are widely distributed over the bins (resulting in high accuracy of FL) and at a low time resolution of $t_{\mathrm{res}} = 6\tau$, where almost all photon counts are in the first bin (resulting in low accuracy of FL), are shown. With a maximum FL accuracy of $10\ \%$, the required minimum time resolution is $t_{\mathrm{res}} = 4\tau$ (**Figure 4.10 Bi**). By increasing the number of photon counts and reducing experimental noise, this limit can be increased (data not shown).

In conclusion, these results show that the time resolution does not necessarily need to be in the ~ps range to determine the FL with a sufficient accuracy. Since more data is generated at higher time resolution, reducing the required time resolution speeds up the chip's read-out rate.

In the following, we discuss the pros and cons of using pixelated array detectors in the context of measurement time and read-out rate. The total measurement time t_{tot} is determined by the number of measurement windows n_{w} times the duration of a measurement window Δt_{w}. The number of measurement windows is given by ratio of the photon counts N_{c} and the count rate $< N_{\mathrm{c}} >_{\mathrm{w}}$

$$t_{\mathrm{tot}} = n_{\mathrm{w}} \cdot \Delta t_{\mathrm{w}} = \frac{N_{\mathrm{c}}}{< N_{\mathrm{c}} >_{\mathrm{w}}} \cdot \Delta t_{\mathrm{w}} \tag{13}$$

As an example, for photon counts of $N_{\mathrm{c}} = 1000$, the maximum count rate, as determined in **Section 4.7**, is $< N_{\mathrm{c}} >_{\mathrm{w,max}} = 0.31$ per pixel. With a duration of a single measurement windows of $\Delta t_{\mathrm{w}} = 7\tau$ (**Figure 4.10 A**) we get following equation

$$t_{\mathrm{tot}} = \frac{7000 \cdot \tau}{0.31 \cdot N_{\mathrm{Pixel}}}. \tag{14}$$

In **Figure 4.11 A**, it is shown that for different FLs, the total measurement time decreases with increasing pixel number.

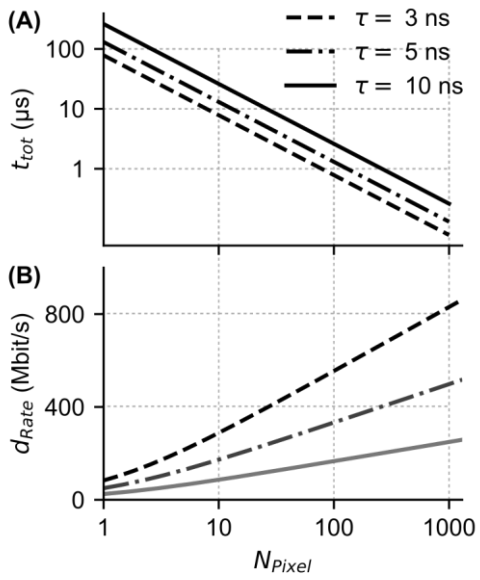

Figure 4.11: SPAD array detector: Impact of the number of pixels on the total measurement time and data rate.
(A) Total measurement time: Total measurement time vs. number of pixels for different FLs (**Equation 14).**
(B) Data rate: Relationship between estimated required data rate of SPAD array detector with on-chip digital signal processing (CMOS device) and number of pixels for different FLs (time resolution t_{res} was set to 4τ) (**Equation 15**).

For a given pixel number, the total measurement time is shorter the smaller FL is, since the minimum duration of the measurement window is shorter (**Figure 4.10 A**). Starting at about 30 pixels, the measurement time (for $\tau \leq 10$ ns) is less than 10 µs, and starting at 300 pixels, a measurement time of less than 1 µs is required to acquire 1000 photon counts and thus determine the FL with a precision and accuracy of 4 % and of 5.5 %, respectively. It is worth to mention that the total measurement duration cannot be shorter than the FL of the analyzed fluorophore. Another limiting factor for the total measurement time is the fluorophore concentration, which determines the number of detectable photons per laser pulse.

To determine the read-out rate, we used a time resolution of $t_{\mathrm{res}} = 4\tau$ according to the results in **Figure 4.10 Bi** and assume that the photon counts from the SPAD array detector's pixels are summed to one photon count value after each measurement window and forwarded to a FPGA for further data processing. Note

that in this case the pixel information and the imaging capabilities of the SPAD array detector get lost. We get following equation for the read-out rate

$$d_{\mathrm{rate}} = \frac{log_2(N_{\mathrm{Pixel}}+1)}{t_{\mathrm{res}}} = \frac{log_2(N_{\mathrm{Pixel}}+1)}{4\cdot\tau}. \quad (15)$$

As expected, **Figure 4.11 B** shows that the read-out rate increases with increasing pixel count. Shorter FLs require a higher read-out rate, since the required time resolution is higher. However, the data rate remains below 1 Gbit/s even with a pixel count of 10^3. These rates can be transferred with modern digital circuits (for comparison USB 3.0: $5\ \mathrm{Gbit/s}$ [107]) and evaluated for example using an FPGA. In this case, read-out rate does not limit the FL measurement time.

4.9 Conclusion

In this paper, the advantages and limitations of using SPAD array detectors for precise and accurate measurement of FLs were investigated. Experiments and single-photon statistic-based Monte Carlo simulations have shown that the precision underlie Poisson statistics and improve with increasing photon counts. We could determine the correlation between photon counts and the FL ratio of fluorophores, which allows to derive the required photon counts to experimentally distinguish fluorophores based on their FLs.

Furthermore, we investigated the correlation between count rate, pile-up-effect and detector's number of pixels. As a result, it could be shown that higher pixel numbers allow higher count rates without pile-up. This, in turn, allows to detect the statistically required photons for a certain precision and accuracy in a shorter time, emphasizing the main advantage of using pixelated SPAD array detectors instead of single-pixel, *e.g.*, PMT detectors. To complete the picture, we derive the correlation between total measurement time, the time resolution, and the read-out rate and show that FLs $< 10\ \mathrm{ns}$ can be measured by a SPAD array detector with 30 SPAD pixels within a measurement time less than $10\ \mu\mathrm{s}$ and with 300 SPAD pixels less than $1\ \mu\mathrm{s}$. SPAD array detectors with a high number of pixels have already been manufactured, such as one from [57] with a 512x512 SPAD array. However, with a high number of pixels, the amount of data to be read out is

correspondingly high. To achieve continuous determination of FLs, the data rate to be read out must not exceed the rate of the system-related transmission evaluation. It has been shown that even with a pixel count of 1000 and FLs $\geq 3\,\mathrm{ns}$, the generated data rates remain still below $1\,\mathrm{Gbit/s}$, data rates achievable with modern digital circuits. These finding are important when looking at high-speed applications for FL measurements such as flow cytometry where measurement times per cell are in the µs-range and can serve as a foundation for developing dedicated high-speed SPAD-based array detectors.

5 Fractional Contributions in a Mixture of Fluorophores

Fluorophores are used in a wide range of biomedical applications: *e.g.* detection of cancer [108] or pathogens [109] in systems such as flow cytometry [110], PoC devices [111] and monitoring environmental parameters (pH [83–85], temperature [86], ion concentration [87]). When analyzing multiple parameters simultaneously, optical filters are used to filter out the emission spectra of individual fluorophores so that many fluorophores can be distinguished at once. However, overlaps in the emission spectra limit the maximum number of fluorophores that can be differentiated [112].

Fluorescence lifetime (FL) is the average time a fluorophore remains in the excited state prior returning to ground state by emitting a fluorescence photon and is characteristic of the fluorophore in question [8]. There are two main approaches to measure FL, either in time-domain or in frequency-domain [90]. FLs measured in the time domain are advantageous over those measured in the frequency domain since complex multi-exponential decays of the fluorescence signal can be investigated [8]. Many standard fluorophores show a mono-exponential decay resulting in one FL [38]. Mixing a multitude of fluorophores results in a multiexponential decay, where for each of the fluorophores a FL τ_i and amplitude-representative pre-exponential factor α_i must be determined [113]. The problem is that with more

than two fluorophores, there are in most cases multiple possible solutions for τ_i and α_i and therefore an explicit determination of all parameters is no longer possible [8]. Many applications measure the change in FLs to determine certain parameters. However, in most cases, the FL of standard fluorophores changes only slightly and can be considered constant or its change predictable. [39,113].

The method presented here uses the FL assumed to be constant to determine the fractional contributions P_i of each fluorophore and can be used to derive the respective fluorophore concentration. This method can be used in conjunction with spectrally resolved methods multiplying the number of distinguishable fluorophores and thus increasing the degree of multiplexing [114].

This chapter demonstrates that the determination of the fractional contribution of individual fluorophores in a mixture is not limited by the number of fluorophores and requires only a minimum delta FL between each of the fluorophores. This assumes that the process of mixing multiple fluorophores does not significantly alter their FLs. Mixtures of 2 and 3 fluorophores were studied experimentally using the SPAD array detector setup developed in **Section 4.1** and compared with simulations. Two analysis methods were used: weighted nonlinear least square (LS) fit method and artificial neural networks (ANN). Using the LS-Fit method, it was shown that for mixtures of 2 fluorophores, the accuracy and precision of the individual fractional contributions increased when the delta FL was higher. Mixtures of 3 fluorophores were also possible using the LS-Fit method, and the accuracy and precision of the fractional contributions of these mixtures were further improved by the use of ANN. Based on these measurement results and Monte Carlo simulations, we then determined the FL difference required for a higher number of fluorophore mixtures.

5.1 Used Fluorophores

The fluorophores used for the measurements in this chapter are lucifer yellow (L0259, Merck, Germany), acriflavine (01673, Merck, Germany), 2-amino-acridone (06627, Merck, Germany), fluorescein (46955, Merck, Germany) and Atto 465 NHS ester (53404, Merck, Germany). Deionized water was used as solvent. The final concentrations for each series of measurements were diluted from a $1\,\mathrm{M}$ stock solution (2-amino-acrdone $c = 15.6\,\mu\mathrm{M}$, fluorescein $c = 3\,\mu\mathrm{M}$; acriflavine $c = 0.2\,\mu\mathrm{M}$; Atto 465 $c = 0.5\,\mu\mathrm{M}$, lucifer yellow $c = 2.0\,\mu\mathrm{M}$). At these concentrations, the detected intensity of the individual fluorophores in the SPAD array detector setup is very similar, so that a wide range of different fractional contributions can be adjusted by mixing different volumes.

5.2 Statistical Analysis

The FLs τ_i and amplitude-representative pre-exponential factors α_i with the emitted intensity I during time t were determined from the histograms by weighted nonlinear least square (LS) fit with a multi-exponential fit function [90]

$$I = \sum\nolimits_{\mathrm{i}}^{\mathrm{n}} \alpha_\mathrm{i} e^{-\frac{t}{\tau_\mathrm{i}}}. \tag{16}$$

This method was compared with an ANN trained with simulations and experimental measurement data. Each fluorophore was examined individually with a volume of 100 µl for each series of measurements, determining the FL and the number of photon counts $N_{\mathrm{c,i}}$ at the present concentration. In the mixture, the fractional contributions P_{set} were determined proportional to the volume fraction v_i of the fluorophore present:

$$P_{\mathrm{set}} = \frac{N_{\mathrm{c,i}} v_\mathrm{i}}{\sum_{\mathrm{i}}^{\mathrm{n}} N_{\mathrm{c,i}} v_\mathrm{i}} \tag{17}$$

The amplitude representative preexponential factors α_i determined with LS fit and ANN and the individually obtained FL τ_i were used to calculate the fractional contributions [8]:

$$P_{\mathrm{LS}} = P_{\mathrm{ANN}} = \frac{\alpha_{\mathrm{i}}\tau_{\mathrm{i}}}{\sum_{\mathrm{i}}^{\mathrm{n}} \alpha_{\mathrm{i}}\tau_{\mathrm{i}}} \tag{18}$$

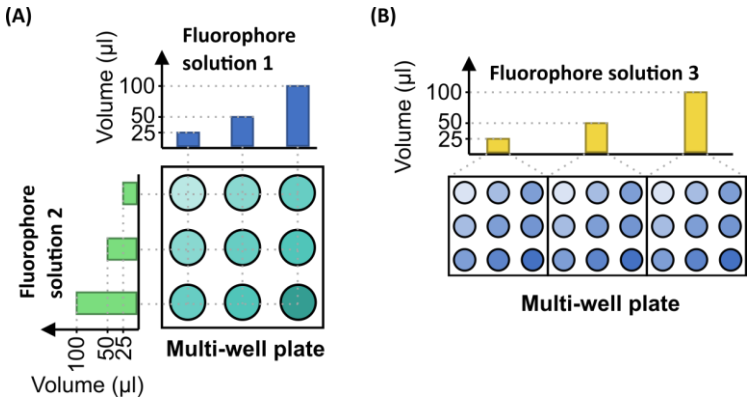

Figure 5.1: Mixtures of several fluorophores to adjust different fractional contributions.
(A) 2 fluorophores: Mixing of 2 different fluorophore solutions in a multi-well plate with different volumes (25 µl, 50 µl, 100 µl).
(B) 3 fluorophores: For mixtures of 3 different fluorophore solutions, different volumes of the third fluorophore were added in addition to the wells prepared as in (A).

To adjust different fractional contributions, the fluorophore solutions were mixed together at different volumes (25, 50 and 100 µl) (**Figure 5.1**). One measurement series, with a mixture of 2 fluorophores consists of 9 variations and with a mixture of 3 fluorophores consists of 27 variations. Each measurement series was repeated three times similar to [115,116]. Since the stock solution was prepared anew after each series of measurements, the fluorophore concentration differs slightly, which is why the measurement points do not match exactly. In order to obtain the minimum determinable fluorophore concentration and its deviation, the difference between the expected P_{e} and the determined P_{d} fractional contributions was calculated. Its mean, referred to here as the mean offset $\langle \Delta P \rangle = \langle P_{\mathrm{d}} - P_{\mathrm{d}} \rangle$, and standard deviation σ represent the minimum determinable fluorophore concentration and deviation, respectively. The data analysis was performed with self-written procedures in Python.

5.3 Principle of Determining Fractional Contributions

The number of fluorophores and their respective intensities that can be distinguished using spectral filters is limited by the superposition of their spectra [112]. Measurements of the emission spectra of the fluorophores lucifer yellow, 2-amino-acridone and fluorescein at the excitation wavelength of 450 nm with the multi-well plate reader show that the spectra overlap strongly, making differentiation using spectral filters almost impossible (**Figure 5.2 A**). When the overlap is smaller, the intensities can be distinguished, but the maximum intensity difference that can be distinguished is still limited.

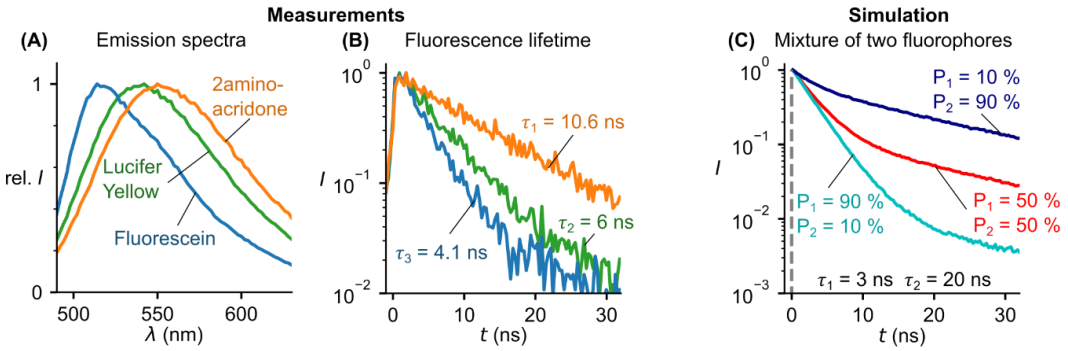

Figure 5.2: Determination of the fractional contributions based on the FLs.
(A) Fluorescence spectra: Overlapping fluorescence spectra of three different fluorophores (2-amino-acridone: orange curve $\tau_1 = 10.6\,ns$, lucifer yellow: green curve $\tau_2 = 6.0\,ns$ and fluorescein: blue curve $\tau_3 = 4.1\,ns$) are almost impossible to separate using spectral filters.
(B) FLs: Fluorescence decay behavior of the fluorophores shown in (A) after excitation with a short laser pulse and determination of each fluorophore specific FL.
(C) Simulation of 2 fluorophores: Simulation of a mixture of 2 fluorophores with different FL at different concentration ratios shows the principle of determining the fractional contributions by calculating the fractional contributions using the amplitude representative pre-exponential factor of the component α_i (**Equation 17**).

In addition to the spectral properties of a fluorophore, the FL is a characteristic parameter (**Figure 5.2 B**), which in most cases changes only by proximity to certain other molecules, such as oxygen [8]. In **Figure 5.2 B**, the FLs of the fluorophores used in **Figure 5.2 A** were determined (2-amino-acridone $\langle\tau_1\rangle = 10.6$ ns, lucifer yellow $\langle\tau_2\rangle = 6.0$ ns and fluorescein: curve $\langle\tau_3\rangle = 4.1$ ns). These values are

in good accordance to the literature (2-amino-acridone in water: $\tau \approx 10\ \mathrm{ns}$ [104], lucifer yellow: $\tau = 5.29\ \mathrm{ns}$ [106], fluorescein in PBS at $\mathrm{pH} = 8$: $\tau = 3.99\ \mathrm{ns}$ [105]).

The use of FL as a constant allows the fractional contributions of fluorophores in the mixture to be determined, further increasing the degree of multiplexing in addition to spectral differentiation (**Figure 5.2 C**) (**Equation 17**). To illustrate this principle, simulations were created representing a mixture of two fluorophores with different FLs ($\tau_1 = 3\ \mathrm{ns}$, $\tau_2 = 20\ \mathrm{ns}$), each with different concentrations and thus fractional contributions (**Figure 5.2 C**). If the concentration of the first fluorophore with the short FL is low, the intensity of the second fluorophore with the long FL predominates and the signal consists mostly of the fluorescence of the second fluorophore (**Figure 5.2 C** dark blue curve). Conversely, if the concentration of the second fluorophore is low, the fluorescence of the first fluorophore predominates (**Figure 5.2 C** cyan curve). Equally distributed fractional contributions of both fluorophores can be clearly distinguished optically from both curves (**Figure 5.2 C** red curve). In this way, different concentration ratios can be determined. In the simulation shown here, the noise and temporal jitter of the signal have not yet been added. The FL difference was set particularly high here to illustrate the principle, whereas real FL differences are much lower, so that a change in fractional contributions is no longer visually apparent.

5.4 Fluorophore Differentiation using LS-Fit

To verify the method addressed in **Section 5.3**, we prepared fluorophore mixtures with 2 and 3 fluorophores at different volumes and determined the fractional contributions using LS fit (**Figure 5.3**). For this purpose, we used a series of different fluorophores (2-amino-acridone $\langle\tau_1\rangle = 10.6\,\mathrm{ns}$, lucifer yellow: $\langle\tau_2\rangle = 6.0\,\mathrm{ns}$, fluorescein $\langle\tau_3\rangle = 4.1\,\mathrm{ns}$, acriflavine $\langle\tau_4\rangle = 5.6\,\mathrm{ns}$, and Atto 465 $\langle\tau_5\rangle = 5.8\,\mathrm{ns}$) to produce mixtures with several FL differences. These values are in good accordance to the literature (2-amino-acridone in water: $\tau \approx 10\,\mathrm{ns}$ [104], lucifer yellow: $\tau = 5.29\,\mathrm{ns}$ [106], fluorescein in PBS at $\mathrm{pH} = 8$: $\tau = 3.99\,\mathrm{ns}$ [105], Acriflavine $\tau = 5\,\mathrm{ns}$ [117], Atto 465 in water at $25\,°\mathrm{C}$ $\tau = 5.2\,\mathrm{ns}$ [118]).

When the determined P_{LS} (**Equation 18**) are close to the set fractional contributions P_{set} (**Equation 17**) of the individual fluorophores, the ideal case shows a linear behavior (**Figure 5.3** grey dashed curve). The deviation from this ideal behavior is described by the mean offset $\langle\Delta P\rangle = \langle P_{LS} - P_{\mathrm{set}}\rangle$ which determines the smallest possible fraction $P_{\mathrm{min,k}} = \langle\Delta P\rangle$ above which the presence of the fluorophore can be detected. The standard deviation of all offsets σ provides information about the resolution with which the fraction contributions can be determined. The smallest possible fraction indicates the maximum possible ratio of intensity fractions, where $N_{\mathrm{c,i}}$ is the number of photon counts for each fluorophore:

$$P_{\mathrm{min,k}} = \frac{N_{\mathrm{c,i}}}{\sum_{\mathrm{i}} N_{\mathrm{c,i}}} \tag{19}$$

Different mixtures of 2 fluorophores show (**Figure 5.3 Ai-iii**) that the determined fractional contributions from the fluorophore mixtures 2-amino-acridone with fluorescein ($\Delta\tau = 6.5\,\mathrm{ns}$, $\langle\Delta P\rangle = 1.8\,\%$, $\sigma = 4.2\,\%$) and 2-amino-acridones with acriflavine ($\Delta\tau = 5.0\,\mathrm{ns}$, $\langle\Delta P\rangle = 3.1\,\%$, $\sigma = 3.3\,\%$) are close to the adjusted fractional contributions. Due to the low mean offset of both mixtures and the proximity of the moving average to the ideal behavior, the minimum possible fractional contribution and thus the maximum possible ratio of the intensity fractions of both fluorophores is also high ($N_{\mathrm{c,1}}/N_{\mathrm{c,3}} = 53.1$, $N_{\mathrm{c,1}}/N_{\mathrm{c,4}} = 31.1$) (**Equation 19**).

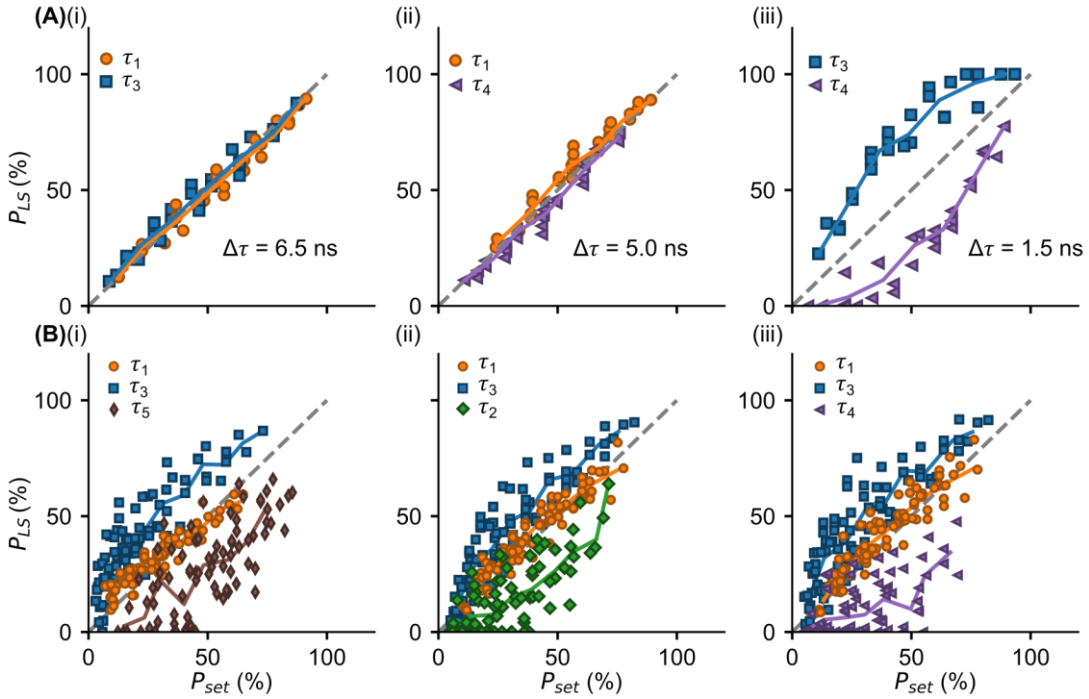

Figure 5.3: Differentiation of (A) 2 and (B) 3 fluorophores using LS-Fit. Experimental results for expected P_{set} (**Equation 17**) against determined fractional contributions P_{LS} (**Equation 18**) for mixtures of 2 (A) and 3 (B) different fluorophores (2-amino-acridone: orange $\tau_1 = 10.6$ ns, Lucifer Yellow: green $\tau_2 = 6.0$ ns, fluorescein: blue $\tau_3 = 4.1$ ns, acriflavine: violet $\tau_4 = 5.6$ ns, Atto 465: brown $\tau_5 = 5.8$ ns) using their FL in different concentrations and volume. Each point shows the fractional contribution of a fluorophore in a mixture. The lines of the same color represent the moving average of the measurement data. (Ai-iii) For mixtures of 2 fluorophores, the deviation from the expected values increases as the FL difference between the fluorophores becomes smaller. (Bi-iii) For mixtures of 3 fluorophores with similar FL differences, fluorophore-specific deviations from the expected values can be seen, which are higher for certain fluorophore combinations.

The fractional contributions from the mixture of acriflavine and Fluorescein ($\Delta\tau = 1.5$ ns, $\langle\Delta P\rangle = 22.5$ %, $\sigma = 8.5$ %) show a higher mean offset than in the previous mixtures, but the fractional contributions of both fluorophores can still be distinguished. Due to the higher mean offset, the maximum possible ratio is also only $N_{c,3}/N_{c,4} = 3.5$. It can also be seen from the moving average that the change is not linear over the entire range.

Since the offset increases with decreasing FL difference for the mixtures shown here, it can be assumed that with a higher FL difference, the determinability of

fractional contributions increases and a minimum FL difference is required. Interactions between fluorophores may also be a possible reason for the high offset and the non-linear behavior of the mixture of acriflavine and fluorescein.

The principle is used in some cases to determine the fractional contributions in mixtures of 2 fluorophores. For some cases the contributions are determined together with the FLs [119,120], in others the FLs are determined before or only once [116,121] after the mixture as individual components. It is known that some FL difference is required [26], however, to our knowledge, no such targeted study has been performed.

The determination of fractional contributions in mixtures of 3 fluorophores was also shown to be possible (**Figure 5.3 Bi-iii**). For this purpose, different mixtures of fluorophores 2-amino-acridone were mixed with fluorescein, varying Atto 465 (**Figure 5.3 Bi**), lucifer yellow (**Figure 5.3 Bii**) or acriflavine (**Figure 5.3 Biii**) and the FL differences between the fluorophores were kept as constant as possible (**Figure 5.3 B** $\Delta\tau_{\mathrm{i}} = 1.7\ \mathrm{ns}$, $\Delta\tau_{\mathrm{ii}} = 1.8\ \mathrm{ns}$, $\Delta\tau_{\mathrm{iii}} = 1.5\ \mathrm{ns}$). Strikingly, in the determined fractional contributions of fluorophores, 2-amino-acridone (orange) exhibits low offsets and standard deviations for all mixtures ($2.6\ \% \leq \langle \Delta P \rangle \leq 3.3\ \%$, $5.1\ \% \leq \sigma \leq 6.4\ \%$). As in **Figure 5.3 Aiii**, the determined fractional contributions of fluorescein (blue) are also above the set ones ($12.5\ \% \leq \langle \Delta P \rangle \leq 19.2\ \%$, $9.8\ \% \leq \sigma \leq 10.7\ \%$), possibly due to interactions between fluorophores. The fractional contributions of the third fluorophore were determined to be too low regardless of the fluorophore, with offsets and standard deviations also differing only slightly (Atto 465: $\langle \Delta P \rangle = -21.8\ \%$, $\sigma = 13.8\ \%$, lucifer yellow: $\langle \Delta P \rangle = -15.1\ \%$, $\sigma = 11.4\ \%$, acriflavine: $\langle \Delta P \rangle = -19.6\ \%$, $\sigma = 13.5\ \%$). Since the offsets and standard deviations differed only slightly for all three mixture variations, it can be assumed that the determination of the fractional contributions is mainly limited by the FLs of the fluorophores.

In the mixture with acriflavine (**Figure 5.3 Biii**), a higher number of certain fractional contributions are determined at $P_{\mathrm{set}} < 50\ \%$ to $P_{\mathrm{LS}} = 0\ \%$ compared to both other mixtures (**Figure 5.3 Bi-ii**). As a result, the determined moving average also assumes lower values, possibly showing a low fluorophore-specific dependence. One possible reason for the fractional contributions of fluorescein being

overestimated and those of the other two fluorophores being underestimated is that fluorescence energy transfer has occurred. For this, the energy of a donor fluorophore is transferred to an acceptor fluorophore, but this requires an overlap of the excitation and emission spectral regions of these two fluorophores [8]. However, this process also leads to the change of the particular FLs, which was not considered here.

To the best of our knowledge, [116] is the only one to have already demonstrated the successful determination of the fractional contributions of 3 fluorophores (Osteosense 750: $\tau = 0.8\,\mathrm{ns}$, Atto 740: $\tau = 1.1\,\mathrm{ns}$, Qtracker 800: τ not determined) using this principle. However, the required fluorophore proportions in the mixture and the determinable resolution of the individual fractional contributions were not determined, making a comparison difficult.

5.5 Fluorophore Mixture Monte Carlo Simulations

To validate the experimentally determined fractional contributions and train the ANN, a self-written Monte Carlo simulation in Python was used. This simulation is based on the FL simulation in **Section 4.4**, modified to simulate multiple fluorophores at various fractional contributions. For this purpose, the decay curves of the fluorophores are generated individually and evaluated in a histogram. In addition, the influence of the temporal jitter is taken into account according to the SPAD array detector used. However, possible chemical interactions between the individual fluorophores are neglected, since they are difficult to predict.

5.6 Artificial Neural Network

As an alternative to the conventional LS fit method, we used fully connected feed-forward ANNs that were trained with both simulated and experimental data in Python using PyTorch [122]. An ANN with 3 hidden layers (40, 20, 10 nodes) was used to determine the fractional contributions of 2 fluorophores, and an ANN with 4 hidden layers (70, 50, 30, 10 nodes) was used for more than 2 fluorophores, using

ReLU (rectified linear unit) as activation functions. The first training step used Monte Carlo simulations of the fluorophore mixtures (10,000 times) with uniformly distributed random volumes (from 10 to 100 µl) and using the determined fixed FLs of the fluorophores in **Section 5.1**. Backpropagation training using the Adam optimization algorithm with a mean square error loss function (MSELoss) was used, with the batch size set to 500 and 20 epochs each at a learning rate of 10^{-3}. This training process was repeated several times until the loss did not decrease noticeably. A second short training process with real experimental data of a measurement series (5 epochs) was performed to determine the fractional contributions of the experimental measurement data.

5.7 Fluorophore Differentiation using ANN

A potential solution to resolve the possible interactions between the fluorophores and the complex changes of the FLs determined in **Section 5.4** and thus to determine the fractional contributions of all fluorophores with small offsets and standard deviations is the use of ANN (**Figure 5.4**). These are particularly suitable for applications where many influencing factors affect the result in complex ways, *e.g.* measurements inside an organism, where each organ provides a different environment [118]. Advantages are the high speed and flexibility of the ANN, which however have to be trained with a high number of data to produce reliable results.

To determine the fractional contributions, a feedforward ANN was trained, which received the temporal histogram data (**Figure 5.2 B**) as input and outputted the amplitude-representative pre-exponential factors α_i, with which the fractional contributions were then determined with **Equation 17** (**Figure 5.4 A**). For comparison, the same measured data of the mixture in **Figure 5.3 Biii** were determined once with LS (**Figure 5.4 Bi**) and once with ANN (**Figure 5.4 Bii**). From the fractional contributions determined by ANN and the resulting moving average, it can be seen that the minimum determinable range, of LS was about 50%. For ANN, the minimum determinable range is about 10%, thus making it possible to determine lower fluorophore concentrations by ANN.

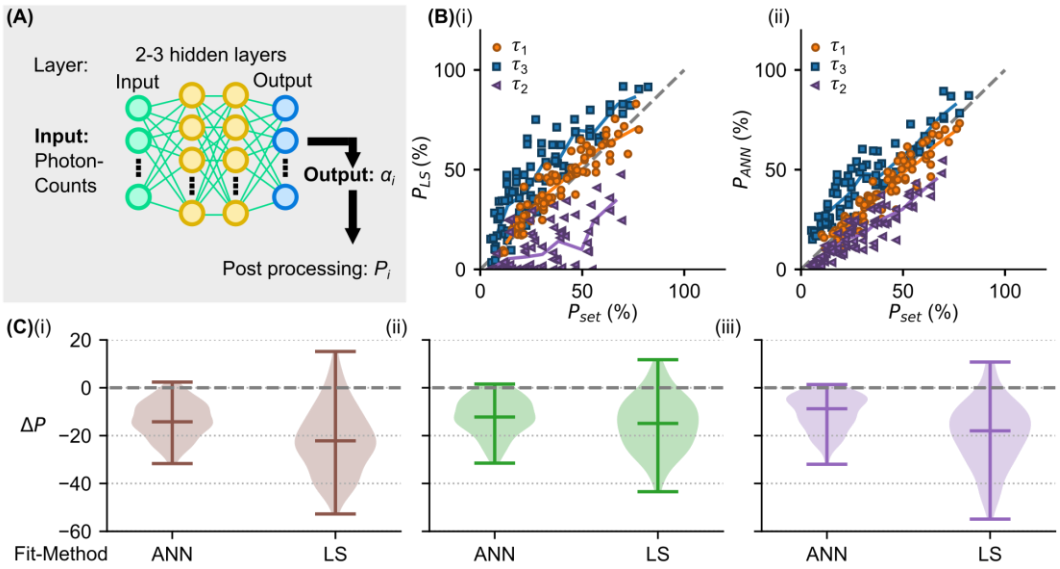

Figure 5.4: Differentiation of 3 fluorophores using ANN.
(A) Schematic structure of the ANN: A feed-forward ANN using a backpropagation training algorithm. The decay curve of the fluorophore mixture was used as input and α of the exponential decay function as output. Depending on the number of fluorophores, 2 or 3 hidden layers were used. The FL of each fluorophore was used to determine the fluorophore fraction (**Equation 17**). The training consisted of two training steps: 1st step with simulated data and 2nd step briefly with a series of real measurements.
(B) LS fit and ANN: Comparison between fractional contributions determined using LS fit (Bi) and a trained ANN (Bii).
(C) Comparison of the distributions: Vase plots showing the distribution of the differences between the determined and expected fractional contribution when varying the third fluorophore with (Ci) Atto 465, (Cii) lucifer yellow and (Ciii) acriflavine, comparing ANN and LS fit.

The measured data of the mixtures in **Figure 5.3 Bi** and in **Figure 5.3 Bii** were also evaluated and compared with ANN. The differences of the fractional contributions can be determined with lower standard deviations and offsets by using ANN (Abb. 4.3 Ci-iii; Atto 465: $\langle \Delta P \rangle = -13.5\ \%$, $\sigma = 7.6\ \%$, lucifer yellow: $\langle \Delta P \rangle = -11.8\ \%$, $\sigma = 7.8\ \%$, acriflavine: $\langle \Delta P \rangle = -11.6\ \%$, $\sigma = 7.5\ \%$) than with LS (**Figure 5.3 Bi-iii**). Thus, it is possible to reliably determine the fractional contributions of all fluorophores with a higher resolution and at lower concentration fractions.

The improved determination of the fractional contributions probably results from the fact that interactions between the fluorophores can be compensated by the nonlinear processing of the data using the ANN. Such an increase in determinability could already be achieved with the use of one measurement series. Therefore, it is expected that training with larger data sets will further reduce the offset and the standard deviation.

The advantage of FL determination by means of ANN compared to conventionally used LS is the high evaluation speed and parallelizability, whereby image data from FL microscope images can be evaluated more quickly [28,123,124]. To our knowledge, this is the first time that ANN have been used specifically for the determination of fractional contributions.

5.8 Comparison and Limitations

Section 5.4 showed that the determination of the fractional contributions is mainly influenced by the FL difference. To evaluate its influence, the standard deviation is used, which results from the differences of the fractional contributions, of the individual measurement series (**Figure 5.5**). Since the obtained standard deviations and the mean FLs determined per measurement series approximately follow a log-normal distribution, the standard deviations of several measurement series repetitions were determined as a geometric mean (**Figure 5.5 B**). The error bars represent the (geometric) standard error of the mean (**Figure 5.5 B**).

In mixtures of 2 fluorophores, this standard deviation decreases with increasing FL difference, which was confirmed by Monte Carlo simulations (**Figure 5.5 A**). The first fluorophore was simulated with a constant FL of $\tau_1 = 4\ \mathrm{ns}$, while the FL of the second fluorophore was varied. Mixtures for which the FL difference was too small to reproducibly determine the fractional contributions by LS showed a standard deviation above the set limit of $\sigma_{\mathrm{LS}} = 10\ \%$, corresponding to a minimum FL difference of $\Delta\tau_{\mathrm{min}} = 0.5\ \mathrm{ns}$ (**Figure 5.5 Ai**). Determination of the fractional contributions by ANN shows a decrease in the determined standard deviations in the simulations (**Figure 5.5 Aii**).

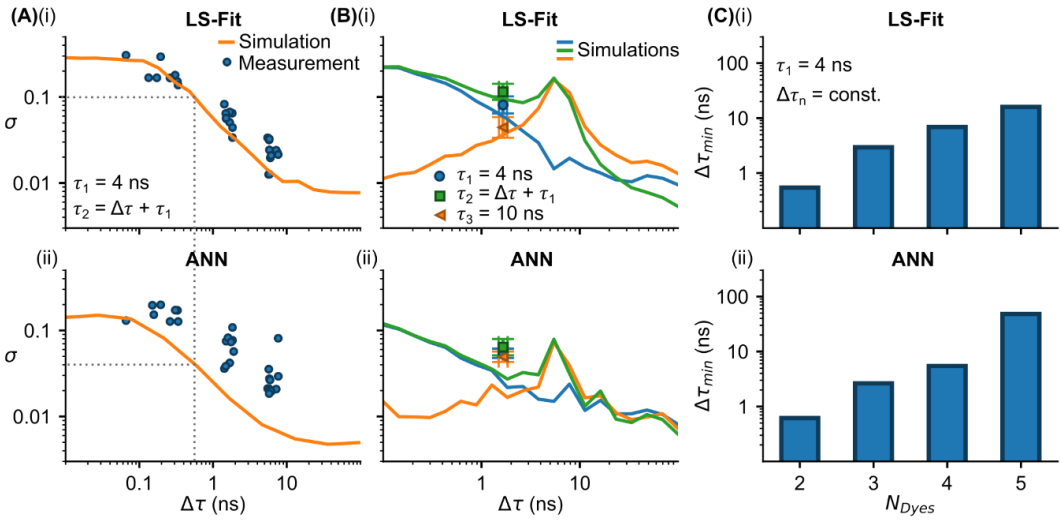

Figure 5.5: Required FL difference to determine the fractional contributions.
(A) 2 and (B) 3 fluorophores: Measurement results and simulations for mixtures with (A) 2 and (B) 3 fluorophores. The standard deviations shown were determined from the differences of the determined and expected fractional contributions and plotted against the FL differences of the fluorophores present in the mixture. The smaller the standard deviation, the more precise the fractional contributions of the fluorophores can be determined. The measurement results were plotted as points that partially overlap, and the simulation results were plotted as lines with corresponding colors. Here, a comparison was made between (Ai, Bi, Ci) LS fit and (Aii, Bii, Cii) ANN. The higher the FL difference between fluorophores in the mixture, the lower the measured and simulated standard deviation.
(C) Multiple fluorophores: Simulation results at equidistant FLs to determine the minimum FL difference, required to determine the fractional contributions, at different numbers of fluorophores. $\sigma = 10\,\%$ (LS fit) of (Ai) and $\sigma = 4\,\%$ (ANN) of (Aii) were used as the threshold above which the determination of the fractional contributions is considered possible. It can be seen that the required FL difference increases with increasing number of fluorophores.

In the experimental measurement results, however, there was no clear improvement in the determinability of the fractional contributions, which can be seen from the fact that the standard deviations of the determinable mixtures remained in approximately the same range of values. The discrepancy between simulation and measured values can be explained by the fact that the ANN were mainly trained with simulation data and these did not reflect all influencing factors that occurred. Since no improvement of the determined fractional contributions occurred by using the ANN, the minimum FL difference of $\Delta\tau_{\mathrm{min}} = 0.5\ \mathrm{ns}$ is also used

as a limit in the ANN. From the simulations, this FL difference results in a minimum required standard deviation of $\sigma_{\mathrm{ANN}} = 4\ \%$.

A FL difference of $\Delta\tau_{\mathrm{min}} = 0.5\ \mathrm{ns}$ for the determination of fractional contributions for 2 fluorophores can be achieved with the combination of many different fluorophores, demonstrating that the method shown here can be used in many applications with existing assays.

In **Figure 5.3 B**, the fractional contributions of all fluorophores in a mixture of 3 fluorophores were successfully determined, and it was seen that the fractional contributions of the fluorophore with the FL between those of the other two fluorophores could only be determined with a higher mean offset and standard deviation. One possible explanation was that these were interactions between the fluorophores. However, this is probably not the case, since this behavior was also shown in Monte Carlo simulations without including fluorophore interactions (**Figure 5.5 Bi**). In the simulations, the FL of the first and third fluorophore were always set to the same values ($\tau_1 = 4\ \mathrm{ns}$, $\tau_3 = 10\ \mathrm{ns}$), whereas the FL of the second fluorophore was varied ($\tau_2 = \Delta\tau + \tau_1$). The simulations show that if the FL of the second fluorophore must lie between those of the other two, a minimum standard deviation at a FL difference of $\Delta\tau = 3\ \mathrm{ns}$ is ideal. This indicates that for an optimal determination of the fractional contributions, the FL difference between the different fluorophores must be equidistant. A minimum FL difference of $\tau = 1.3\ \mathrm{ns}$ is required to reach the previously established threshold of $\sigma_{\mathrm{LS}} = 10\ \%$. Since the FL of a large number of fluorophores are in the limit range ($5.3\ \mathrm{ns} \leq \tau_2 \leq 8\ \mathrm{ns}$), the use of 3 fluorophores for the determination of fractional contributions with various fluorophores for different applications is also conceivable.

In **Figure 5.4**, the improvement in the determination of fractional contributions by using ANN was successfully demonstrated. However, just as when considering 2 fluorophores (**Figure 5.5 Aii**), there is a discrepancy between simulated and experimentally determined standard deviations for 3 fluorophores (**Figure 5.5 Bii**). One possible reason, as in **Figure 5.5 Aii**, is that the simulated data do not reflect all the influencing factors that occur. The difference between the set and determined fractional contributions for each fluorophore in the mixture (**Section 5.4**) could be

reduced by using the ANN (**Section 5.7**), which was also shown here in the simulations (**Figure 5.5 Bii**). To reach the previously established limit of $\sigma_{\mathrm{ANN}} = 4\,\%$, a minimum FL difference of $\tau = 1\,\mathrm{ns}$ is required. The cutoff range of FLs of possible usable fluorophores with ANN is similar to the LS method ($5\,\mathrm{ns} \leq \tau_2 \leq 8\,\mathrm{ns}$), but has the advantage that the determined fractional contributions have a lower offset and standard deviation. Thus, by using ANN instead of LS, lower fluorophore concentrations and higher resolution of fractional contributions can be determined.

Previous simulations in **Figure 5.5 Bi** determined that an equidistant FL difference ($\Delta\tau = |\tau_1 - \tau_2| = |\tau_2 - \tau_3|$) with 3 fluorophores allowed an optimal determination of the fractional contributions. Therefore, additional simulations were carried out using equidistant FL differences from an increasing number of fluorophores showing the minimum FL differences needed to reach the established limit of $\sigma_{\mathrm{LS}} = 10\,\%$ (**Figure 5.5 Ci**) and $\sigma_{\mathrm{ANN}} = 4\,\%$ (**Figure 5.5 Cii**). It can be seen that fluorophore mixtures with more than 3 fluorophores are difficult to achieve because the FL of the fluorophores exceeds 10 ns, which does not occur in most fluorophores encountered [8,38].

Based on the simulation results, which achieved very low standard deviations, it is expected that adjustments to the type of ANN used and training method on a larger data base, can lead to a significant increase in the possible applicable FL differences and the accuracy of the determined fractional contributions, as in other areas, such as object detection [125].

In the simulations performed here, the FL of the first fluorophore is fixed at a value of $\tau = 4\,\mathrm{ns}$, the lowest FL used here also occurring in this range ($\langle\tau_3\rangle = 4.1\,\mathrm{ns}$). Adjustments to a lower FL may result in the determination of fractional contributions from more than 3 fluorophores. Integration of this method into existing assays, such as those used in enzyme-linked immunosorbent assay (ELISA) and flow cytometry measurement systems, could theoretically allow an increase in the number of distinguishable fluorophores by several fold.

5.9 Conclusion

In this chapter, we determined different factors that influence the determination of fractional contributions based on FLs in fluorophore mixtures by performing experimental measurements and confirming them through Monte Carlo simulations. The accuracy and precision of the determined fractional contributions are thereby mainly limited by the FL difference of the fluorophores in the mixture, where a minimum FL difference is required. This minimum FL difference increases with increasing fluorophore number, where even in a mixture of 4 fluorophores the minimum FL difference is $\Delta\tau_{\mathrm{min}} = 7\ \mathrm{ns}$. Through the use of ANN instead of the conventionally used LS fit, we achieved a significant increase in accuracy and precision of the determined fractional contributions, since these were determined with a lower standard deviation (from $\langle\sigma_{\mathrm{LS}}\rangle = 12.9\ \%$ to $\langle\sigma_{\mathrm{ANN}}\rangle = 7.6\ \%$), at lower fluorophore fractions (from $\langle\langle\Delta P\rangle_{\mathrm{LS}}\rangle = -18.8\ \%$ to $\langle\langle\Delta P\rangle_{\mathrm{ANN}}\rangle = 12.3\ \%$). In areas where spectral differentiation of fluorophores reaches its limits when using optical filters, this method can be used to multiply the number of fluorophores that can be differentiated.

6 Differentiation of Background Fluorescence by Fractional Contributions

Flow cytometry is used for the characterization of suspended single cells and is applied in areas such as cancer therapy [126] and detection of pathogens [127]. The cells to be analyzed are labelled with several fluorophores, which are excited in a fluidic channel using a laser and the fluorescence is registered on a detector. The cells can be counted, characterized and sorted using the signal obtained. However, the solution to be analyzed also contains unbound fluorophores and autofluorescent components that cause the detected intensity signal to fluctuate significantly, which complicates the differentiation and characterization of the target cells [27,128–130]. This signal is referred to here as background fluorescence.

Different methods have been developed to reduce the influence of background fluorescence [131,132]. One of these methods is the differentiation of cells and particles based on the characteristic fluorescence lifetime (FL) [133]. In this context, the FLs of the fluorophores used are usually known and their changes are small or predictable [39,113]. Therefore, the fractional contribution method studied in **Chapter 5** can be used to increase the differentiability of the targeted cells and particles from other components in the solution (**Figure 6.1**).

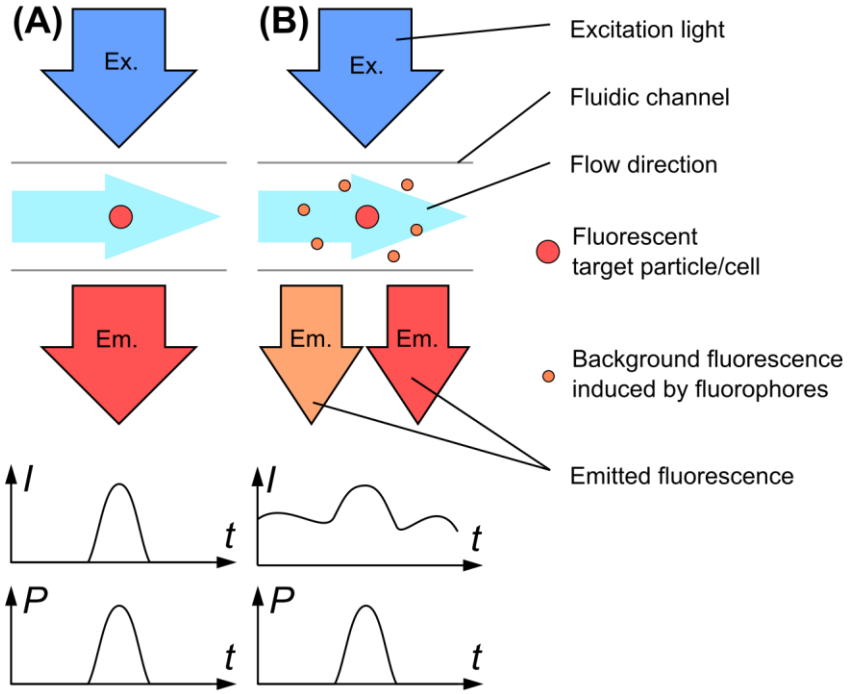

Figure 6.1: Influence of background fluorescence.
(A) Without background fluorescence: Fluorescence of a target particle or cell flowing through a fluidic channel that can be registered and counted after excitation with light.
(B) With background fluorescence: Additional fluorophores in the fluid produce an additional fluorescence signal. Since the concentration of fluorophores varies, the resulting background fluorescence is not constant. If the detected intensity is too high, the particles/cells cannot be clearly registered and counted. However, by determining the fractional contributions P, it is still possible to clearly identify the incoming particles/cells.

This chapter investigates how high the proportion of background fluorescence is allowed to be for successful differentiation by determining the fractional contributions and what FL difference is required for this purpose. Also investigated is how many photon counts are needed for successful differentiation. For this purpose, measurements were performed with fluorescent microparticles suspended in a microfluidic system with various fluorophores added to the solution. Monte Carlo simulations were then used to further investigate the dependencies of the FL differences. With the results obtained, extrapolations were then made as to what particle count rate is possible with the measurement setup and the SPAD array detector used.

6.1 Fluorescent Fluorophores

The fluorophores used are lucifer yellow (L0259, Merck, Germany), acriflavine (01673, Merck, Germany), 2-amino-acridone (06627, Merck, Germany), fluorescein (46955, Merck, Germany), Atto 465-NHS-ester (53404, Merck, Germany) and deionized water was used as solvent. All fluorophores were present at a concentration of $c = 0.9\ \mathrm{M}$ in the solution (**Figure 6.4**). 2-amino-acridone was present at a concentration of $c = 0.83\ \mathrm{M}$ with Atto 465 present at a concentration of $c = 82.6\ \mathrm{mM}$ in the solution (**Figure 6.5**).

6.2 Microfluidic System Measurements

The measurement setup developed in **Chapter 4.1** was used here to investigate the possible count and flow rates for a flow cytometric measurement method (**Figure 6.2**). The SPAD array detector used for this purpose, however, is not optimized for flow cytometric applications because the time required for readout after each measurement window is about $19.2\ \mu\mathrm{s}$. This is due to all 192x2 pixels of the SPAD array detector being read out sequentially at a frequency of $20\ \mathrm{MHz}$. To investigate the number of photon counts that can be achieved to determine the required measurement time, microparticles (Fluorobrite® Microparticels, Polyscience Inc., US) with a diameter of $45\ \mu\mathrm{m}$ were added to the microfluidic system (10000211 Straight channel chip (4 parallel channels), microfluidic ChipShop GmbH, GER) and the flow of solution in the microfluidic system was stopped to keep the microparticles in one location. The microfluidic system was then scanned and a FL measurement was taken at each position. 50 different measurement positions were scanned per measurement series, with $30{,}000$ measurement windows each. The fractional contributions and total intensity from all photon counts were determined from the measurement results.

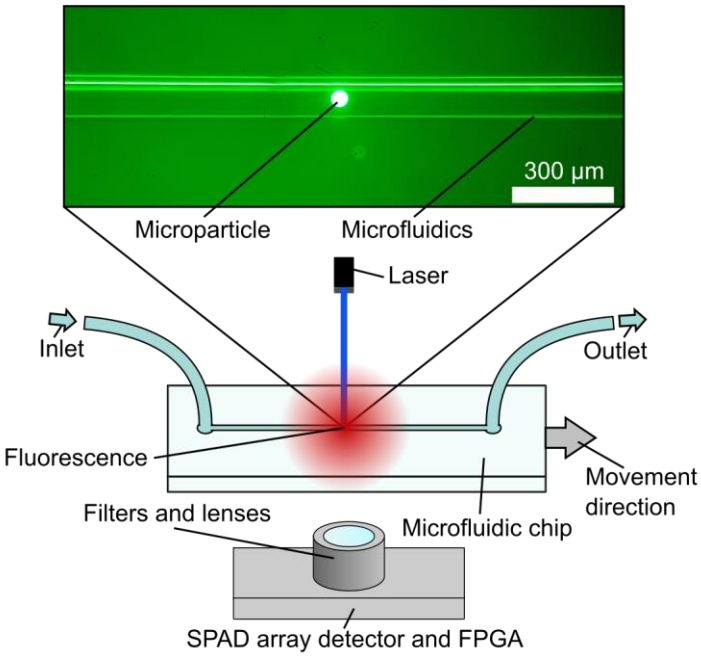

Figure 6.2: Schematic representation of the measurement setup. Microparticles suspended in DI water are placed in a microfluidic chip and fixed in one position (upper microscopy image). A laser is used to illuminate a spot on the microfluidic chip, and the fluorescence emitted below the microfluidic chip is detected by the SPAD array detector. By moving the microfluidic chip in the corresponding direction, the microfluidic is scanned point by point. Background fluorescence is then generated by introducing fluorophores into the solution of suspended microparticles.

To determine the FL of the microparticles (**Appendix, Figure A.1 B**), the point at which the intensity was maximum in **Figure 6.3 B** was evaluated.

For **Figure 6.6**, the measurements in **Figure 6.4** and **Figure 6.5** and two further repeat measurements in each case, measurement windows were randomly selected at the positions with the maximum (particle fluorescence) and minimum intensity (background fluorescence) until the required photon counts were reached. These photon counts were then used to determine the fractional contributions and whether differentiability of the particles from the background fluorescence was possible. Differentiability was defined as follows:

$$P_{\mathrm{wP}} > P_{\mathrm{woP}} + 3\sigma_{\mathrm{woP}} \tag{20}$$

For this purpose, the fractional contribution with particle fluorescence (P_{wP}), the fractional contribution of the background fluorescence (P_{woP}) and its standard deviation distribution (σ_{woP}) are used.

6.3 Particle Detection

In order to identify microparticles, they must stand out from the background signal. Then a threshold value can be defined from which a microparticle can be counted as detected (**Figure 6.3**). Below the threshold, microparticles are either not counted or incorrectly identified as such.

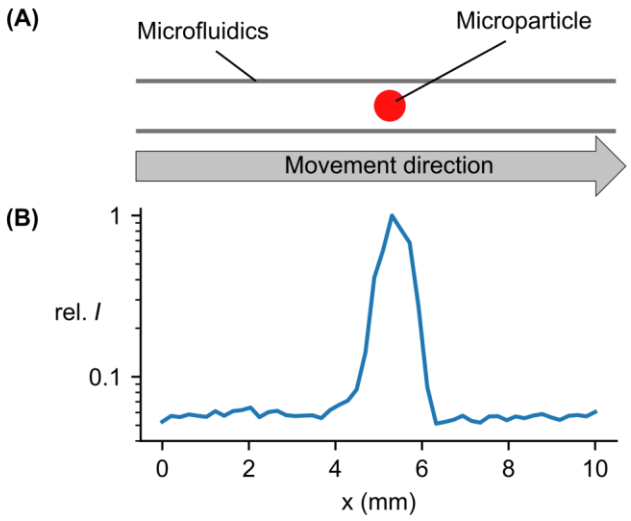

Figure 6.3: Detection of fluorescent microparticles.
(A) Schematic representation of the measurement process: Microparticles with a diameter of $45\ \mu\mathrm{m}$ are in a microfluidic system with a diameter of $100\ \mu\mathrm{m}$ fixated in one position.
(B) Detected intensity: By shifting the fluidics and recording the fluorescence, the required measurement time can be investigated.

The intensity results (**Figure 6.3 B**) show that over a channel length of $2\ \mathrm{mm}$, the fluorescence of the single microparticle can be detected. This is because the laser spot is not focused but collimated to a diameter of about $2\ \mathrm{mm}$. Outside the area in which the microparticles were excited, a much lower intensity could be determined. This is because the microparticles were suspended in DI water during this

measurement, resulting in the intensity being mainly due to the dark count rate (DCR) of the SPAD array detector. When flow resumes, the particles can be clearly distinguished from the substrate and counted.

To determine the maximum flow rate at which particles can be counted with the measurement setup used here, it is assumed that all particles are at least $2\ \mathrm{mm}$ apart due to the laser width. From the sum signal of the detected particle in **Figure 6.3 B**, an average of about 0.2 photon counts per measurement window can be detected at this particle spacing. Thus, to detect at least one photon from a particle, at least 5 measurement windows per particle are required. With a single measurement time of $20.48\ \mu\mathrm{s}$, consisting of measurement window $1.28\ \mu\mathrm{s}$ and readout time $19.2\ \mu s$, the required measurement time is about $102\ \mu\mathrm{s}$. The maximum possible count rate of 9765 particles per second results from the reciprocal of this measurement time. Taking into account the minimum distance between individual particles, this corresponds to a maximum flow rate of $199\ \mu\mathrm{l}/\mathrm{s}$ for the microfluidics used (width: $100\ \mu\mathrm{m}$, height: $100\ \mu\mathrm{m}$). However, it should be noted that only one photon count per particle can be expected in these calculations, which is not sufficient for characterization of the particles. If 1000 photon counts per measurement are expected, a maximum flow rate of $0.2\ \mu\mathrm{l}/\mathrm{s}$ can be set. Compared to other systems, this flow rate is not particularly high, as the pumps used for this purpose can often achieve flow rates of 1 to $10\ \mu\mathrm{l}/\mathrm{s}$ [134,135]. The reason for this is that the system is not optimized for excitation and detection in microfluidics, but for measurements in 96 well plates. By focusing the laser directly on the microfluidics and using optimized objectives, a higher photon count rate can be expected at smaller distances between particles, resulting in a higher flow rate.

6.4 Particle Differentiation in Background Fluorescence

In contrast to the measurements performed in **Section 6.3**, real applications involve many other components (unbound fluorophores and substances with intrinsic fluorescence [27]) producing background fluorescence, which makes it difficult to differentiate the cells and particles under investigation. When the

background fluorescence is also in the same spectral range, optical filters cannot be used for differentiation. An alternative method is to use the FL characteristic from the fluorophore, as discussed in **Chapter 5**. This has already been used in the frequency domain [133], but is limited by the fact that multiexponential decay curves cannot be evaluated. By performing the determination in the time domain, multiple FLs can be distinguished from each other and the respective fractional contributions can be determined. For this purpose, the components to be determined must have different FLs.

In order to create conditions where the microparticles are no longer clearly distinguishable from the background fluorescence based on the intensity change, different fluorophores emitting in the similar spectral range (**Appendix, Figure A.1 A**) were mixed into the solution with the particles. The determined FL of a microparticle ($\tau_\mathrm{p} = 3.4\ \mathrm{ns}$), shows that the difference to the fluorophores used is higher than the minimum required threshold of $\Delta\tau_\mathrm{min} = 0.5\ \mathrm{ns}$ determined in **Chapter 5**.

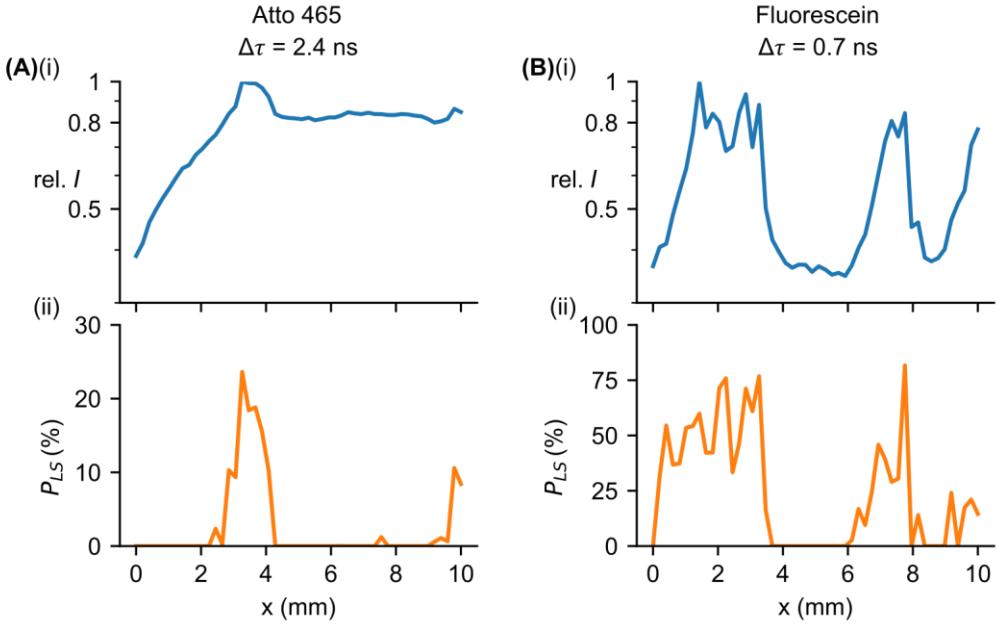

Figure 6.4: Differentiation of microparticles with fluorescent background. Microparticles in a solution containing a fluorophore (**(A)** Atto 465 and **(B)** Fluorescein) with a fluctuating (i) fluorescence intensity. Determination of the (ii) fractional contribution of the microparticles allows for intensity-independent differentiation.

After mixing the fluorophores Atto 465 or Fluorescein into the solution containing the microparticles, an increase in the measured background fluorescence is observed. Moreover, this is not constant over the scanned region, as the concentration of the fluorophore may differ in some regions (**Figure 6.4 Ai and Bi**). When a particle is excited, the measured intensity increases. However, if the background fluorescence is too high, it is difficult to differentiate the intensity of a particle from the background fluorescence. Under worst case conditions, either the particle is not recognized, or a particle is falsely identified.

By determining the fractional contributions, the fluorescence of the particles can be precisely assigned, independent of the intensity of the background fluorescence (**Figure 6.4 Aii and Bii**). This is also possible when the detected intensity increases by less than $20\,\%$ for a particle detection (FL difference $\Delta\tau = 2.4\,ns$) (**Figure 6.4 Ai**) and also possible when the FL difference ($\Delta\tau = 0.7\,ns$) is close to the limiting value ($\Delta\tau_{\min} = 0.5\,ns$) (**Figure 6.4 Bi**). Since this could be shown for a total of 5 different fluorophores (**Appendix, Figure A.2**), it can be assumed, as in **Chapter 5**, that the principle can be applied independently of the fluorophore used.

In most cases, different sample types are distinguished in flow cytometric measurements by binding multiple fluorophores [136,137]. Thus, by using multiple fluorophores, it is possible that these fluorophores also enter the solution and contribute to the background fluorescence. For this reason, it was now also investigated whether a differentiation of the particles is possible with two fluorophores (Atto 465 and 2-amino-acridone) in the solution (**Figure 6.5**).

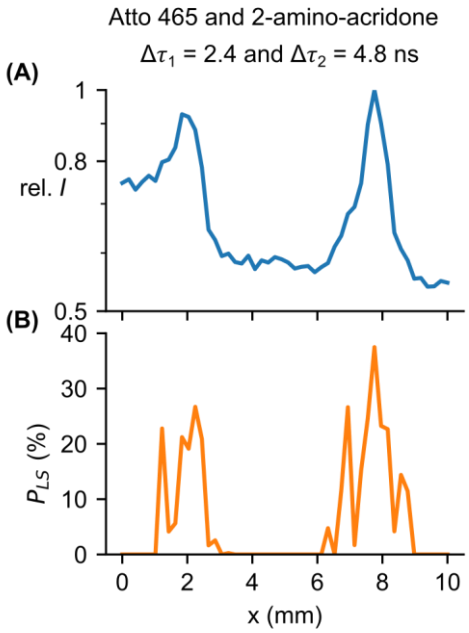

Figure 6.5: Differentiation of microparticles with fluorescent background using 2 Fluorophores. Microparticles are in a solution of two fluorophores (Atto 465 and 2-amino-acridone) with a fluctuating **(A)** fluorescence intensity. Determination of the **(B)** fractional contribution of the microparticles allows intensity-independent differentiation.

Despite the varying background fluorescence (**Figure 6.5 A**) due to both fluorophores, it is still possible to clearly determine the fractional contributions of the particles (**Figure 6.5 B**). The concentrations of the fluorophores were chosen such that the background fluorescence corresponds to a fraction of 50 % of the particle fluorescence. The successful determination of the fractional contributions of all three fluorophores (as in **Chapter 5**) shows that even particles labelled with several fluorophores can be characterized by this method.

6.5 Required Fluorescence Fraction and Number of Detected Photons

To investigate whether the tests performed in **Section 6.3 and Section 6.4** are suitable for flow cytometric measurement, Monte Carlo simulations (as in **Chapter 5**) were performed and these were supplemented with measurement results where possible (**Figure 6.6**). Here the threshold was determined at which differentiation from the background fluorescence is still possible. Pile-up was not considered, since its influence was already investigated in **Chapter 4**.

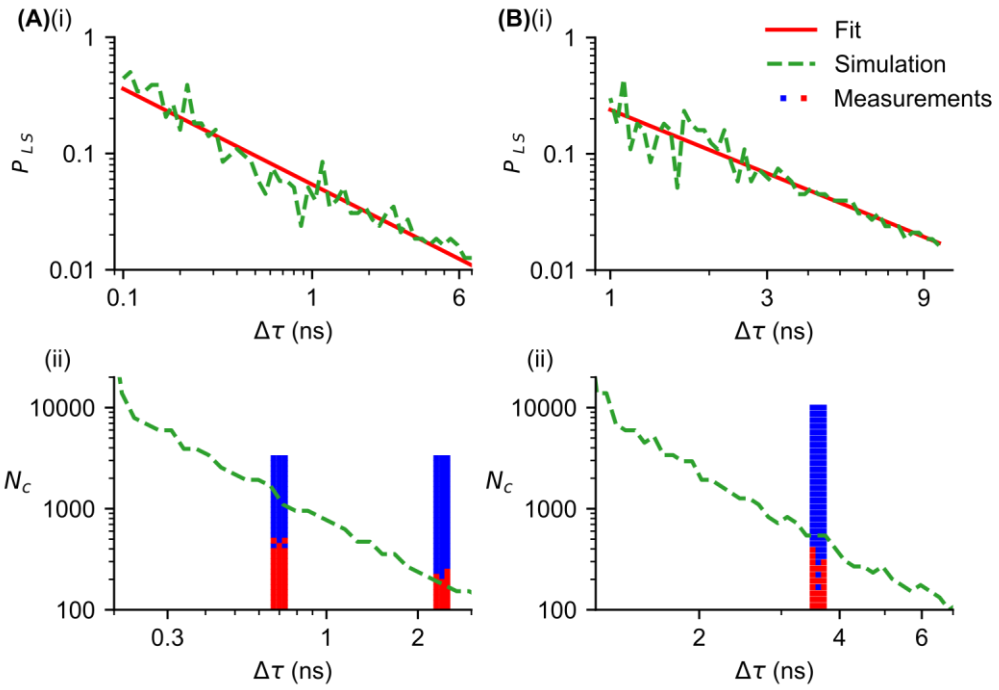

Figure 6.6: Required fluorescence fraction and number of detected photons with fluorescent background using (A) 1 and (B) 2 Fluorophores. (Ai and Bi) Fractional contribution P_{LS} of the particles required for differentiation must be above the specified limit (simulation: green dashed curve, fit: red curve) for $N_{\mathrm{c}} = 30{,}000$. (Aii and Bii) The number of total photon counts required for differentiation at a fractional contribution $P_{\mathrm{LS}} = 0.5$, must also be above the specified limit (simulation: green dashed line, measurement differentiation possible: blue squares, measurement differentiation not possible: red squares) plotted with three repetitions next to each other. The determined limits depend on the (A) FL difference of the particles and one fluorophore or (B) in case of two fluorophores also their respective FL difference.

The simulation results in **Figure 6.6 Ai and Bi** show that the limit of the fractional contribution of the particle at which differentiation is still possible depends linearly in the log-log representation on the FL difference. According to the simulation results (**Figure 6.6 Ai**), the differentiation of the particles is possible at the used FL differences $\Delta\tau = 0.7\ \mathrm{ns}$ and $\Delta\tau = 2.4\ \mathrm{ns}$ up to the respective fractional contribution of $8\ \%$ and $3\ \%$ from the background fluorescence generated by a fluorophore. With two fluorophores (**Figure 6.6 Bi**) in solution with a mean FL difference of $\Delta\tau = 2.4\ \mathrm{ns}$, a fractional contribution from the particles of $6\ \%$ should be differentiable according to the simulations. In some applications, the fluorescence to be detected is very low, thus this method can be used to differentiate it from the predominant autofluorescence [129].

Experimental measurements to confirm these simulation results were not performed, since the concentration of the fluorophores could not be further increased without the occurrence of self-absorption and a resulting significant FL change (data not shown). However, with several of the fluorophores used, a fractional contribution of about $50\ \%$ to the particle fluorescence could be reached (**Figure 6.4 and Figure 6.5**). The simulations in **Figure 6.6 Aii and Bii** with the fractional contributions of 50 % of the background fluorescence also show in the log-log plot a linear dependence of the required number of detected photon counts for a successful differentiation on the FL difference. The approximate limit determined by the simulations was confirmed by measurements.

The results show that a certain number of photon counts is necessary to differentiate the particles from the background fluorescence with the LS-Fit method (**Figure 6.6 Aii and Bii, blue squares**). However, if this number is insufficient, differentiation is no longer possible (**Figure 6.6 Aii and Bii, red squares**). By using the ANN utilized in this dissertation, an improvement of the differentiation, especially at low fractional contributions and at low photon counts [123] can be expected.

For all performed measurements, the threshold value of the required photon counts for a successful differentiation is less than 1000 photons, which enables a flow rate of 0.2 µl/s, as determined in **Section 6.3**, to be used for differentiation. If the setup is optimized for flow cytometric measurements, a higher mean photon

count rate can be expected, allowing a higher flow rate. This is due to the advantages of SPAD array detectors over the conventionally used PMT detectors, such as the high pixel count and thus the high average photon detection rate that can be allowed. The pile-up limitation investigated in **Chapter 4** results in a maximum average photon count rate of 119 counts per measurement window with the 384 pixels SPAD array detector employed here. This results in a maximum particle count rate of 5425 per second and a maximum possible flow rate of about $108.5\ \mu l/s$ according to the parameters defined in **Section 6.3**. Thus, theoretically, a high particle count rate at a high flow rate can also be achieved with this detector chip compared to other flow cytometer systems [134,135]. However, compared to the SPAD array detector used in [22] ($60{,}000$ cells per second), only a lower particle count rate is achievable here due to the long readout time from the SPAD array detector chip. Furthermore, the differentiation of particles by fractional contributions allows to differentiate a higher number of fluorophores and therefore also a higher number of particles or cells labelled with different fluorophores.

6.6 Conclusion

In this chapter, the potential of differentiation of fluorescent cells and particles at high background fluorescence using fractional contributions based on the characteristic FLs was shown to be applicable in flow cytometry. The experimental results showed that less than 1000 photon counts are required for successful differentiation at a background fluorescence of $50\ \%$, even when there is only a small FL difference of $\Delta\tau = 0.7\ \mathrm{ns}$ from the targeted samples. This also applies when the background fluorescence is caused by two different fluorophores. Using the SPAD array detector presented here and a measurement setup optimized for flow cytometry, extrapolations show that a maximum particle count rate of about 5425 per second is achievable. This particle count rate is limited by the readout rate of the SPAD array detector chip used and is significantly lower compared to a SPAD array detector optimized for flow cytometry [22] ($60{,}000$ cells per second).

7 Combined Conclusion and Outlook

In this dissertation, the parameters of SPAD array detectors required for chemiluminescence and fluorescence-based biomedical applications were investigated. For this purpose, two measurement setups with different SPAD array detectors and corresponding Monte Carlo simulations were developed to investigate the optimal parameters.

The high sensitivity and integration of the SPAD array detectors was shown to be particularly suitable for compact and lens-free chemiluminescence-based applications. Measurements on SARS-CoV-2 RNA and ssDNA showed that with the SPAD setup developed here and a suitable assay, the sensitivity of $10^6\ \mathrm{copies/ml}$ defined as sufficient by WHO [75] can be achieved theoretically. In addition, the Monte Carlo simulations showed key parameters such as a high fill factor (*e.g.* by using microlenses [81]), and a total photosensitive area that should not be larger than the biosensor from where the chemiluminescence originates. In a lens-free system design, reflection and refraction from the biosensor to the detector should also be reduced as much as possible, *e.g.* by using intermediate layers with the lowest possible refractive index differences to the fluid material. If these optimization measures are taken into account, further applications are possible, such as

the PCR-free detection of SARS-CoV-2 RNA with its associated advantages such as a high analysis speed.

Another feature of SPAD array detectors is the high temporal resolution with which FLs can be determined in the nanosecond range. However, especially with a high number of pixels and a high temporal resolution, continuous measurement is usually not possible due to the amount of data generated. Therefore, in the biomedical field, these detectors are usually limited to use in FLIMs requiring long measurement times. However, when all pixels of the SPAD array detector are used simultaneously to determine a FL, the influence of the limiting pile-up effect is reduced, and with 300 SPAD pixels, FLs at ≤ 10 ns can be measured in less than 1 µs. This enables new application areas such as FL-based flow cytometry with direct cell sorting.

In the previous paragraph, it was assumed that only one FL of a fluorophore needs to be determined. However, when the fluorophores are present in a mixture, it is often not possible to determine the FLs to distinguish the individual fluorophores. Knowing this, however, it is possible to distinguish the fluorophores by determining the fractional contributions. Experimental measurements and Monte Carlo simulations have shown that in order to successfully determine the fractional contributions, the fluorophores present in the mixture must have a minimum FL difference which increases with increasing number of fluorophores. In addition, the use of artificial neural networks (ANN) allows the fractional contributions to be determined with higher accuracy and precision compared to LS fitting. This method is particularly suitable in areas where the differentiation of fluorophores with optical filters reaches its limits and can multiply the number of fluorophores to be differentiated. Thus, in applications such as ELISA, the number of differentiable fluorophores can be increased several fold.

In flow cytometry, a large number of fluorophores are differentiated, in this context it may happen during some measurements that the detected fluorescence is very low compared to the background fluorescence. Measurements and Monte Carlo simulations have shown that fewer than 1000 photon counts are required to successfully differentiate from background fluorescence, regardless of the spectrum, when the background fluorescence is 50 % of the target fluorescence signal

and the FL difference is only $\Delta\tau = 0.7\ \mathrm{ns}$. With the SPAD array detector used here, a theoretical particle count rates of about 5425 per second can be achieved. However, this requires the here developed measurement setup to be optimized for flow cytometric measurements, *e.g.* focusing the laser and optics on the fluidic channel. With the results shown here, applications such as vivo FL-based flow cytometry are conceivable where a high degree of autofluorescence occur [138].

To further improve the key performance parameters of the analytical methods addressed here, such as the detection limit in the chemiluminescence-based PoC measurement system or the flow rate and differentiability in flow cytometry, the development of dedicated SPAD array detectors is required. To ensure that the highest possible photon fraction can be detected, a high fill factor is required which is not limited by the size of the evaluation circuit. This can be achieved, for example, by 3D integration, in which the SPAD array detectors and the evaluation circuitry, located on separate wafers, are brought together only after fabrication. However, such 3D integration also leads to an increase in cost, which should be kept as low as possible for use in PoC measurement systems. Another way to increase the fill factor is to move part of the data evaluation outside the SPAD array detector to the connected FPGA or ASIC. Depending on the requirements, photon counts can then be summed or the time stamp required for FL determination can be provided. This way, it would be possible to cover the requirements of both application areas addressed here with the development of one SPAD array detector.

References

1. Ahmad, F.B.; Anderson, R.N. The Leading Causes of Death in the US for 2020. *JAMA* **2021**, *325*, 1829–1830, doi:10.1001/jama.2021.5469.
2. World Health Organization. Coronavirus Disease (COVID-19) Dashboard. World Health Organization. Available online: https://www.who.int/emergencies/diseases/novel-coronavirus-2019 (accessed on 2 December 2021).
3. Corman, V.; Bleicker, T.; Brünink, S.; Drosten, C. Diagnostic detection of 2019-nCoV by real-time RT-PCR. Available online: https://www.who.int/docs/default-source/coronaviruse/protocol-v2-1.pdf (accessed on 2 December 2021).
4. Scerbo, M.H.; Kaplan, H.B.; Dua, A.; Litwin, D.B.; Ambrose, C.G.; Moore, L.J.; Murray, C.C.K.; Wade, C.E.; Holcomb, J.B. Beyond Blood Culture and Gram Stain Analysis: A Review of Molecular Techniques for the Early Detection of Bacteremia in Surgical Patients. *Surg. Infect. (Larchmt)* **2016**, *17*, 294–302, doi:10.1089/sur.2015.099.
5. Giuliano, C.; Patel, C.R.; Kale-Pradhan, P.B. A Guide to Bacterial Culture Identification And Results Interpretation. *P. T.* **2019**, *44*, 192–200.
6. Fereja, T.H.; Hymete, A.; Gunasekaran, T. A Recent Review on Chemiluminescence Reaction, Principle and Application on Pharmaceutical Analysis. *ISRN Spectroscopy* **2013**, *2013*, 1–12, doi:10.1155/2013/230858.
7. Pierce, M.C.; Weigum, S.E.; Jaslove, J.M.; Richards-Kortum, R.; Tkaczyk, T.S. Optical systems for point-of-care diagnostic instrumentation: analysis of imag-

ing performance and cost. *Ann. Biomed. Eng.* **2014**, *42*, 231–240, doi:10.1007/s10439-013-0918-z.

8. Lakowicz, J.R. *Principles of fluorescence spectroscopy*, 3rd ed.; Springer: New York, 2006, ISBN 0387312781.
9. Ateya, D.A.; Erickson, J.S.; Howell, P.B.; Hilliard, L.R.; Golden, J.P.; Ligler, F.S. The good, the bad, and the tiny: a review of microflow cytometry. *Anal. Bioanal. Chem.* **2008**, *391*, 1485–1498, doi:10.1007/s00216-007-1827-5.
10. Lesaicherre, M.-L.; Uttamchandani, M.; Chen, G.Y.J.; Yao, S.Q. Antibody-Based fluorescence detection of kinase activity on a peptide array. *Bioorganic & Medicinal Chemistry Letters* **2002**, *12*, 2085–2088, doi:10.1016/S0960-894X(02)00378-5.
11. Kricka, L.J. Clinical applications of chemiluminescence. *Analytica Chimica Acta* **2003**, *500*, 279–286, doi:10.1016/S0003-2670(03)00809-2.
12. Xu, W.; Chan, K.M.; Kool, E.T. Fluorescent nucleobases as tools for studying DNA and RNA. *Nat. Chem.* **2017**, *9*, 1043–1055, doi:10.1038/nchem.2859.
13. Hopkins, T.A.; Seliger, H.H.; White, E.H.; Cass, M.H. The chemiluminescence of firefly luciferin. A model for the bioluminescent reaction and identification of the product excited state. *J. Am. Chem. Soc.* **1967**, *89*, 7148–7150, doi:10.1021/ja01002a076.
14. Rudolf Seitz, W. Immunoassay labels based on chemiluminescence and bioluminescence. *Clinical Biochemistry* **1984**, *17*, 120–125, doi:10.1016/S0009-9120(84)90318-7.
15. Matsuzawa, T.; Aoki, Y.; Takeuchi, N.; Murayama, Y. A New Long Phosphorescent Phosphor with High Brightness, SrAl2 O 4 : Eu2 + , Dy3 +. *J. Electrochem. Soc.* **1996**, *143*, 2670–2673, doi:10.1149/1.1837067.
16. Donati, S.; Tambosso, T. Single-Photon Detectors: From Traditional PMT to Solid-State SPAD-Based Technology. *IEEE J. Select. Topics Quantum Electron.* **2014**, *20*, 204–211, doi:10.1109/JSTQE.2014.2350836.
17. Gollob, C.; Ritter, T.; Kraßnitzer, R.; Tockner, A.; Nothdurft, A. Measurement of Forest Inventory Parameters with Apple iPad Pro and Integrated LiDAR Technology. *Remote Sensing* **2021**, *13*, 3129, doi:10.3390/rs13163129.

18. Luetzenburg, G.; Kroon, A.; Bjørk, A.A. Evaluation of the Apple iPhone 12 Pro LiDAR for an Application in Geosciences. *Sci. Rep.* **2021**, *11*, 22221, doi:10.1038/s41598-021-01763-9.
19. Mokroš, M.; Mikita, T.; Singh, A.; Tomaštík, J.; Chudá, J.; Wężyk, P.; Kuželka, K.; Surový, P.; Klimánek, M.; Zięba-Kulawik, K.; et al. Novel low-cost mobile mapping systems for forest inventories as terrestrial laser scanning alternatives. *International Journal of Applied Earth Observation and Geoinformation* **2021**, *104*, 102512, doi:10.1016/j.jag.2021.102512.
20. Zappa, F.; Tisa, S.; Tosi, A.; Cova, S. Principles and features of single-photon avalanche diode arrays. *Sensors and Actuators A: Physical* **2007**, *140*, 103–112, doi:10.1016/j.sna.2007.06.021.
21. Katsoulidou, V.; Bergmann, A.; Becker, W. How fast can TCSPC FLIM be made? In *Advanced Photon Counting Techniques II.* Optics East 2007, Boston, MA, Sunday 9 September 2007; Becker, W., Ed.; SPIE, 2007; 67710B.
22. Della Rocca, F.M.; Nedbal, J.; Tyndall, D.; Krstajić, N.; Li, D.D.-U.; Ameer-Beg, S.M.; Henderson, R.K. Real-time fluorescence lifetime actuation for cell sorting using a CMOS SPAD silicon photomultiplier. *Opt. Lett.* **2016**, *41*, 673–676, doi:10.1364/OL.41.000673.
23. Sarder, P.; Maji, D.; Achilefu, S. Molecular probes for fluorescence lifetime imaging. *Bioconjug. Chem.* **2015**, *26*, 963–974, doi:10.1021/acs.bioconjchem.5b00167.
24. Tramier, M.; Gautier, I.; Piolot, T.; Ravalet, S.; Kemnitz, K.; Coppey, J.; Durieux, C.; Mignotte, V.; Coppey-Moisan, M. Picosecond-Hetero-FRET Microscopy to Probe Protein-Protein Interactions in Live Cells. *Biophysical Journal* **2002**, *83*, 3570–3577, doi:10.1016/S0006-3495(02)75357-5.
25. Pepperkok, R.; Squire, A.; Geley, S.; Bastiaens, P.I.H. Simultaneous detection of multiple green fluorescent proteins in live cells by fluorescence lifetime imaging microscopy. *Current Biology* **1999**, *9*, 269–274, doi:10.1016/S0960-9822(99)80117-1.
26. Brismar, H.; Ulfhake, B. Fluorescence lifetime measurements in confocal microscopy of neurons labeled with multiple fluorophores. *Nat. Biotechnol.* **1997**, *15*, 373–377, doi:10.1038/nbt0497-373.

27. Alberti, S.; Parks, D.R.; Herzenberg, L.A. A single laser method for subtraction of cell autofluorescence in flow cytometry. *Cytometry* **1987**, *8*, 114–119, doi:10.1002/cyto.990080203.
28. Wu, G.; Nowotny, T.; Zhang, Y.; Yu, H.-Q.; Li, D.D.-U. Artificial neural network approaches for fluorescence lifetime imaging techniques. *Opt. Lett.* **2016**, *41*, 2561–2564, doi:10.1364/OL.41.002561.
29. Wiedemann, E. Ueber Fluorescenz und Phosphorescenz I. Abhandlung. *Ann. Phys. Chem.* **1888**, *270*, 446–463, doi:10.1002/andp.18882700703.
30. Newton Harvey. A History of Luminescence From the Earliest Times Until 1900. *The American Historical Review* **1958**, doi:10.1086/ahr/63.4.937.
31. Virk, H.S. History of Luminescence from Ancient to Modern Times. *DDF* **2015**, *361*, 1–13, doi:10.4028/www.scientific.net/DDF.361.1.
32. Radziszewski, B.R. Untersuchungen über hydrobenzamid, amarin und lophin. *Berichte der deutschen chemischen Gesellschaft* **1877**, *10*, 70–75.
33. Cinquanta, L.; Fontana, D.E.; Bizzaro, N. Chemiluminescent immunoassay technology: what does it change in autoantibody detection? *Auto Immun. Highlights* **2017**, *8*, 9, doi:10.1007/s13317-017-0097-2.
34. García-Campaña, A.M.; Baeyens, W.R.G. Principles and recent analytical applications of chemiluminescence. *Analusis* **2000**, *28*, 686–698, doi:10.1051/analusis:2000280686.
35. Baeyens, W.R.G.; Schulman, S.G.; Calokerinos, A.C.; Zhao, Y.; García Campaña, A.M.; Nakashima, K.; Keukeleire, D. de. Chemiluminescence-based detection: principles and analytical applications in flowing streams and in immunoassays. *Journal of Pharmaceutical and Biomedical Analysis* **1998**, *17*, 941–953, doi:10.1016/S0731-7085(98)00062-4.
36. Ghosh, S.; Ahn, C.H. Lyophilization of chemiluminescent substrate reagents for high-sensitive microchannel-based lateral flow assay (MLFA) in point-of-care (POC) diagnostic system. *Analyst* **2019**, *144*, 2109–2119, doi:10.1039/C8AN01899E.
37. Parker, C.A.; Rees, W.T. Correction of fluorescence spectra and measurement of fluorescence quantum efficiency. *Analyst* **1960**, *85*, 587, doi:10.1039/an9608500587.

38. Joung, J.F.; Han, M.; Jeong, M.; Park, S. Experimental database of optical properties of organic compounds. *Sci. Data* **2020**, *7*, 295, doi:10.1038/s41597-020-00634-8.
39. Grauw, C.J. de; Gerritsen, H.C. Multiple Time-Gate Module for Fluorescence Lifetime Imaging. *Appl Spectrosc* **2001**, *55*, 670–678, doi:10.1366/0003702011952587.
40. *Fluorescence applications in biotechnology and life sciences;* Goldys, E.M., Ed.; Wiley-Blackwell: Hoboken, N.J., 2009, ISBN 978-0-470-08370-3.
41. Kim, H.; Choi, S.-K.; Ahn, J.; Yu, H.; Min, K.; Hong, C.; Shin, I.-S.; Lee, S.; Lee, H.; Im, H.; et al. Kaleidoscopic fluorescent arrays for machine-learning-based point-of-care chemical sensing. *Sens. Actuators B Chem.* **2021**, *329*, doi:10.1016/j.snb.2020.129248.
42. Natarajan, S.; Su, F.; Jayaraj, J.; Shah, M.I.I.; Huang, Y. A paper microfluidics-based fluorescent lateral flow immunoassay for point-of-care diagnostics of non-communicable diseases. *Analyst* **2019**, *144*, 6291–6303, doi:10.1039/C9AN01382B.
43. Rochas, A.; Gosch, M.; Serov, A.; Besse, P.A.; Popovic, R.S.; Lasser, T.; Rigler, R. First fully integrated 2-D array of single-photon detectors in standard CMOS technology. *IEEE Photon. Technol. Lett.* **2003**, *15*, 963–965, doi:10.1109/LPT.2003.813387.
44. Beer, M. SPAD basierte Sensoren für die laufzeitbasierte Distanzmessung bei hoher Hintergrundlichtintensität. PhD thesis; Universität Duisburg Essen, Duisburg, 2018.
45. Badih El-Kareh. *Silicon Devices and Process Integration*: *Deep Submicron and Nano-Scale Technologies;* Springer US: Boston, MA, 2009, ISBN 9780387690100.
46. Eisele, A.; Henderson, R.; Schmidtke, B.; Funk, T.; Grant, L.; Richardson, J.; Freude, W. 185 MHz count rate 139 dB dynamic range single-photon avalanche diode with active quenching circuit in 130 nm CMOS technology. In.
47. Maruyama, Y.; Blacksberg, J.; Charbon, E. A 1024 x 8, 700-ps Time-Gated SPAD Line Sensor for Planetary Surface Exploration With Laser Raman Spec-

troscopy and LIBS. *IEEE J. Solid-State Circuits* **2014**, *49*, 179–189, doi:10.1109/JSSC.2013.2282091.

48. Palubiak, D.P.; Deen, M.J. CMOS SPADs: Design Issues and Research Challenges for Detectors, Circuits, and Arrays. *IEEE J. Select. Topics Quantum Electron.* **2014**, *20*, 409–426, doi:10.1109/JSTQE.2014.2344034.
49. Cheng, Z.; Zheng, X.; Palubiak, D.; Deen, M.J.; Peng, H. A Comprehensive and Accurate Analytical SPAD Model for Circuit Simulation. *IEEE Trans. Electron Devices* **2016**, *63*, 1940–1948, doi:10.1109/TED.2016.2537879.
50. Pellegrini, S.; Warburton, R.E.; Tan, L.J.J.; Ng, J.S.; Krysa, A.B.; Groom, K.; David, J.P.R.; Cova, S.; Robertson, M.J.; Buller, G.S. Design and Performance of an InGaAs–InP Single-Photon Avalanche Diode Detector. *IEEE J. Quantum Electron.* **2006**, *42*, 397–403, doi:10.1109/JQE.2006.871067.
51. Rech, I.; Ingargiola, A.; Spinelli, R.; Labanca, I.; Marangoni, S.; Ghioni, M.; Cova, S. Optical crosstalk in single photon avalanche diode arrays: a new complete model. *Opt. Express* **2008**, *16*, 8381–8394, doi:10.1364/OE.16.008381.
52. Panglosse, A.; Martin-Gonthier, P.; Marcelot, O.; Virmontois, C.; Saint-Pé, O.; Magnan, P. Modeling, Simulation Methods and Characterization of Photon Detection Probability in CMOS-SPAD. *Sensors (Basel)* **2021**, *21*, doi:10.3390/s21175860.
53. Zarghami, M.; Gasparini, L.; Parmesan, L.; Moreno-Garcia, M.; Stefanov, A.; Bessire, B.; Unternahrer, M.; Perenzoni, M. A 32 × 32-Pixel CMOS Imager for Quantum Optics With Per-SPAD TDC, 19.48% Fill-Factor in a 44.64-µm Pitch Reaching 1-MHz Observation Rate. *IEEE J. Solid-State Circuits* **2020**, *55*, 2819–2830, doi:10.1109/JSSC.2020.3005756.
54. Buttafava, M.; Villa, F.; Castello, M.; Tortarolo, G.; Conca, E.; Sanzaro, M.; Piazza, S.; Bianchini, P.; Diaspro, A.; Zappa, F.; et al. SPAD-based asynchronous-readout array detectors for image-scanning microscopy. *Optica* **2020**, *7*, 755, doi:10.1364/OPTICA.391726.
55. Incoronato, A.; Locatelli, M.; Zappa, F. Statistical Modelling of SPADs for Time-of-Flight LiDAR. *Sensors (Basel)* **2021**, *21*, doi:10.3390/s21134481.

56. Bruschini, C.; Homulle, H.; Antolovic, I.M.; Burri, S.; Charbon, E. Single-photon avalanche diode imagers in biophotonics: review and outlook. *Light Sci. Appl.* **2019**, *8*, 87, doi:10.1038/s41377-019-0191-5.
57. Ulku, A.C.; Bruschini, C.; Antolovic, I.M.; Charbon, E.; Kuo, Y.; Ankri, R.; Weiss, S.; Michalet, X. A 512×512 SPAD Image Sensor with Integrated Gating for Widefield FLIM. *IEEE J. Select. Topics Quantum Electron.* **2019**, *25*, doi:10.1109/JSTQE.2018.2867439.
58. Henderson, R.K.; Johnston, N.; Della Mattioli Rocca, F.; Chen, H.; Day-Uei Li, D.; Hungerford, G.; Hirsch, R.; Mcloskey, D.; Yip, P.; Birch, D.J.S. A 192 x 128 Time Correlated SPAD Image Sensor in 40-nm CMOS Technology. *IEEE J. Solid-State Circuits* **2019**, *54*, 1907–1916, doi:10.1109/JSSC.2019.2905163.
59. Lagarto, J.L.; Villa, F.; Tisa, S.; Zappa, F.; Shcheslavskiy, V.; Pavone, F.S.; Cicchi, R. Real-time multispectral fluorescence lifetime imaging using Single Photon Avalanche Diode arrays. *Sci. Rep.* **2020**, *10*, 8116, doi:10.1038/s41598-020-65218-3.
60. Fraunhofer IMS. *Development not published*.
61. Fraunhofer IMS. SPADEYE2 - CMOS LIDAR SENSOR. Available online: https://www.ims.fraunhofer.de/content/dam/ims/de/documents/Downloads/SPADeye2.pdf (accessed on 3 December 2021).
62. Beer, M.; Thattil, C.; F. Haase, J.; Ruskowski, J.; Brockherde, W.; Kokozinski, R. SPAD-Based LiDAR Sensor in 0.35 µm Automotive CMOS with Variable Background Light Rejection. *Proceedings* **2018**, *2*, 749, doi:10.3390/proceedings2130749.
63. Rong, X.M.; Yang, L.; Di Chu, H.; Fan, M. Effect of delay in diagnosis on transmission of COVID-19. *Math. Biosci. Eng.* **2020**, *17*, 2725–2740, doi:10.3934/mbe.2020149.
64. Johansson, M.A.; Quandelacy, T.M.; Kada, S.; Prasad, P.V.; Steele, M.; Brooks, J.T.; Slayton, R.B.; Biggerstaff, M.; Butler, J.C. SARS-CoV-2 Transmission From People Without COVID-19 Symptoms. *JAMA Netw. Open* **2021**, *4*, e2035057, doi:10.1001/jamanetworkopen.2020.35057.
65. Cubas-Atienzar, A.I.; Kontogianni, K.; Edwards, T.; Wooding, D.; Buist, K.; Thompson, C.R.; Williams, C.T.; Patterson, E.I.; Hughes, G.L.; Baldwin, L.; et

al. Limit of detection in different matrices of 19 commercially available rapid antigen tests for the detection of SARS-CoV-2. *Sci. Rep.* **2021**, *11*, 18313, doi:10.1038/s41598-021-97489-9.

66. Scott, A. Reagents hold up European COVID-19 tests. *C&EN Global Enterp* **2020**, *98*, 11, doi:10.1021/cen-09813-buscon3.
67. Tecan Austria GmbH. Instructions for Use for Infinite 200 PRO. Available online: http://biomimetic-lab.vscht.cz/wp-content/uploads/2017/04/Infinite-200-PRO.pdf (accessed on 4 February 2022).
68. Nimse, S.B.; Song, K.; Sonawane, M.D.; Sayyed, D.R.; Kim, T. Immobilization techniques for microarray: challenges and applications. *Sensors (Basel)* **2014**, *14*, 22208–22229, doi:10.3390/s141222208.
69. Tolnai, Z.; Harkai, Á.; Szeitner, Z.; Scholz, É.N.; Percze, K.; Gyurkovics, A.; Mészáros, T. A simple modification increases specificity and efficiency of asymmetric PCR. *Analytica Chimica Acta* **2019**, *1047*, 225–230, doi:10.1016/j.aca.2018.10.017.
70. Khailany, R.A.; Safdar, M.; Ozaslan, M. Genomic characterization of a novel SARS-CoV-2. *Gene Rep.* **2020**, *19*, 100682, doi:10.1016/j.genrep.2020.100682.
71. Laue, M.; Kauter, A.; Hoffmann, T.; Möller, L.; Michel, J.; Nitsche, A. Morphometry of SARS-CoV and SARS-CoV-2 particles in ultrathin plastic sections of infected Vero cell cultures. *Sci. Rep.* **2021**, *11*, 3515, doi:10.1038/s41598-021-82852-7.
72. Mak, G.C.; Cheng, P.K.; Lau, S.S.; Wong, K.K.; Lau, C.S.; Lam, E.T.; Chan, R.C.; Tsang, D.N. Evaluation of rapid antigen test for detection of SARS-CoV-2 virus. *J. Clin. Virol.* **2020**, *129*, 104500, doi:10.1016/j.jcv.2020.104500.
73. Eftekhari, A.; Alipour, M.; Chodari, L.; Maleki Dizaj, S.; Ardalan, M.; Samiei, M.; Sharifi, S.; Zununi Vahed, S.; Huseynova, I.; Khalilov, R.; et al. A Comprehensive Review of Detection Methods for SARS-CoV-2. *Microorganisms* **2021**, *9*, doi:10.3390/microorganisms9020232.
74. Wang, X.; Yao, H.; Xu, X.; Zhang, P.; Zhang, M.; Shao, J.; Xiao, Y.; Wang, H. Limits of Detection of 6 Approved RT-PCR Kits for the Novel SARS-

Coronavirus-2 (SARS-CoV-2). *Clin. Chem.* **2020**, *66*, 977–979, doi:10.1093/clinchem/hvaa099.

75. WHO & R&D Blue Print. Target product profiles for priority diagnostics to support response to the COVID-19 pandemic v.1.0 (2020). Available online: https://www.who.int/publications/m/item/covid-19-target-product-profiles-for-priority-diagnostics-to-support-response-to-the-covid-19-pandemic-v.0.1 (accessed on 13 October 2021).
76. Sharma, K.K. *Optics*: *Principles and Applications;* Elsevier Science & Technology: San Diego, 2006, ISBN 9780080463919.
77. Papula, L. *Mathematische Formelsammlung*: *Für Ingenieure und Naturwissenschaftler*, 12. Aufl. 2017; Springer Vieweg: Wiesbaden, 2017, ISBN 978-3658161941.
78. Morimoto, K.; Charbon, E. A Scaling Law for SPAD Pixel Miniaturization. *Sensors (Basel)* **2021**, *21*, doi:10.3390/s21103447.
79. Sultanova, N.; Kasarova, S.; Nikolov, I. Dispersion Properties of Optical Polymers. *Acta Phys. Pol. A* **2009**, *116*, 585–587, doi:10.12693/APhysPolA.116.585.
80. Schneider, F.; Draheim, J.; Kamberger, R.; Wallrabe, U. Process and material properties of polydimethylsiloxane (PDMS) for Optical MEMS. *Sensors and Actuators A: Physical* **2009**, *151*, 95–99, doi:10.1016/j.sna.2009.01.026.
81. Intermite, G.; McCarthy, A.; Warburton, R.E.; Ren, X.; Villa, F.; Lussana, R.; Waddie, A.J.; Taghizadeh, M.R.; Tosi, A.; Zappa, F.; et al. Fill-factor improvement of Si CMOS single-photon avalanche diode detector arrays by integration of diffractive microlens arrays. *Opt. Express* **2015**, *23*, 33777–33791, doi:10.1364/OE.23.033777.
82. Canals, J.; Franch, N.; Alonso, O.; Vilà, A.; Diéguez, A. A Point-of-Care Device for Molecular Diagnosis Based on CMOS SPAD Detectors with Integrated Microfluidics. *Sensors (Basel)* **2019**, *19*, doi:10.3390/s19030445.
83. Poehler, E.; Pfeiffer, S.A.; Herm, M.; Gaebler, M.; Busse, B.; Nagl, S. Microchamber arrays with an integrated long luminescence lifetime pH sensor. *Anal. Bioanal. Chem.* **2016**, *408*, 2927–2935, doi:10.1007/s00216-015-9178-0.

84. Netaev, A.; Karaduman, B.D.; Sheikh, M.A.; Schierbaum, N.; Seidl, K. pH-and oxygen sensors based on fluorescent nanoparticles for Lab-on-Chip applications. *Biomedical Engineering / Biomedizinische Technik* **2020**, *65*, 296–300, doi:10.1515/bmt-2020-6051.
85. Netaev, A.; Karaduman, B.D.; Sheikh, M.A.; Schierbaum, N.; Seidl, K. Single photon avalanche diode (SPAD)-based sensor system for measuring the fluorescence lifetime of functionalized silica-nanoparticles [Single-Photon Avalanche Diode (SPAD)-basiertes Sensorsystem zur Messung der Fluoreszenzlebensdauer von funktionalisierten Silica-Nanopartikeln]. *Mikro-Nano-Integration - 8. GMM-Workshops* **2020**.
86. Inada, N.; Fukuda, N.; Hayashi, T.; Uchiyama, S. Temperature imaging using a cationic linear fluorescent polymeric thermometer and fluorescence lifetime imaging microscopy. *Nat. Protoc.* **2019**, *14*, 1293–1321, doi:10.1038/s41596-019-0145-7.
87. Gilbert, D.; Franjic-Würtz, C.; Funk, K.; Gensch, T.; Frings, S.; Möhrlen, F. Differential maturation of chloride homeostasis in primary afferent neurons of the somatosensory system. *Int. J. Dev. Neurosci.* **2007**, *25*, 479–489, doi:10.1016/j.ijdevneu.2007.08.001.
88. Becker, W. Fluorescence lifetime imaging--techniques and applications. *J. Microsc.* **2012**, *247*, 119–136, doi:10.1111/j.1365-2818.2012.03618.x.
89. Li, D.D.-U.; Ameer-Beg, S.; Arlt, J.; Tyndall, D.; Walker, R.; Matthews, D.R.; Visitkul, V.; Richardson, J.; Henderson, R.K. Time-domain fluorescence lifetime imaging techniques suitable for solid-state imaging sensor arrays. *Sensors (Basel)* **2012**, *12*, 5650–5669, doi:10.3390/s120505650.
90. Datta, R.; Heaster, T.M.; Sharick, J.T.; Gillette, A.A.; Skala, M.C. Fluorescence lifetime imaging microscopy: fundamentals and advances in instrumentation, analysis, and applications. *J. Biomed. Opt.* **2020**, *25*, 1–43, doi:10.1117/1.JBO.25.7.071203.
91. Léonard, J.; Dumas, N.; Caussé, J.-P.; Maillot, S.; Giannakopoulou, N.; Barre, S.; Uhring, W. High-throughput time-correlated single photon counting. *Lab Chip* **2014**, *14*, 4338–4343, doi:10.1039/c4lc00780h.

92. Salthammer, T. Numerical simulation of pile-up distorted time-correlated single photon counting (TCSPC) data. *J. Fluoresc.* **1992**, *2*, 23–27, doi:10.1007/BF00866385.
93. Sato, D.; Shindo, T.; Mitsunaka, T.; Fujimoto, Y.; Iizuka, K.; Tago, S.; Takayama, Y.; Fujii, T.; Kim, S.H. Integrated Parallel Flow Cytometry Device with Time Gated Spads. In *2019 20th International Conference on Solid-State Sensors, Actuators and Microsystems & Eurosensors XXXIII (TRANSDUCERS & EUROSENSORS XXXIII).* 2019 20th International Conference on Solid-State Sensors, Actuators and Microsystems & Eurosensors XXXIII (TRANSDUCERS & EUROSENSORS XXXIII), Berlin, Germany, 23–27 Jun. 2019; IEEE, 2019 - 2019; pp 17–20, ISBN 978-1-5386-8104-6.
94. Zickus, V.; Wu, M.-L.; Morimoto, K.; Kapitany, V.; Fatima, A.; Turpin, A.; Insall, R.; Whitelaw, J.; Machesky, L.; Bruschini, C.; et al. Fluorescence lifetime imaging with a megapixel SPAD camera and neural network lifetime estimation. *Sci. Rep.* **2020**, *10*, 20986, doi:10.1038/s41598-020-77737-0.
95. Hwang, W.; Kim, D.; Moon, S.; Kim, D.Y. Achieving a high photon count rate in digital time-correlated single photon counting using a hybrid photodetector. *Opt. Express* **2021**, *29*, 9797–9804, doi:10.1364/OE.419896.
96. Suyama, M.; Kawai, Y.; Kimura, S.; Asakura, N.; Hirano, K.; Hasegawa, Y.; Saito, T.; Morita, T.; Muramatsu, M.; Yamamoto, K. A compact hybrid photodetector (HPD). *IEEE Trans. Nucl. Sci.* **1997**, *44*, 985–989, doi:10.1109/23.603790.
97. Isbaner, S.; Karedla, N.; Ruhlandt, D.; Stein, S.C.; Chizhik, A.; Gregor, I.; Enderlein, J. Dead-time correction of fluorescence lifetime measurements and fluorescence lifetime imaging. *Opt. Express* **2016**, *24*, 9429–9445, doi:10.1364/OE.24.009429.
98. Arlt, J.; Tyndall, D.; Rae, B.R.; Li, D.D.-U.; Richardson, J.A.; Henderson, R.K. A study of pile-up in integrated time-correlated single photon counting systems. *Review of Scientific Instruments* **2013**, *84*, 103105, doi:10.1063/1.4824196.
99. *A 256 x 256 SPAD array with in-pixel Time to Amplitude Conversion for Fluorescence Lifetime Imaging Microscopy;* Parmesan Luca; Neale Dutton; Nikola Krstajic; N. Calder; A. Holmes; Grant, L.A.; Robert Henderson, Eds., 2015.

100. *Flow Cytometry Protocols;* Hawley, T.S.; Hawley, R.G., Eds., 4th ed. 2018; Humana Press: New York, NY, 2018, ISBN 9781493973460.
101. Harris, C.M.; Selinger, B.K. Single-Photon Decay Spectroscopy. II. The Pile-up Problem. *Aust. J. Chem.* **1979**, *32*, 2111, doi:10.1071/CH9792111.
102. Turgeman, L.; Fixler, D. Photon efficiency optimization in time-correlated single photon counting technique for fluorescence lifetime imaging systems. *IEEE Trans. Biomed. Eng.* **2013**, *60*, 1571–1579, doi:10.1109/TBME.2013.2238671.
103. Zhang; Chung; Oldenburg. A Simple Statistical Parameter for Use in Evaluation and Validation of High Throughput Screening Assays. *J. Biomol. Screen.* **1999**, *4*, 67–73, doi:10.1177/108705719900400206.
104. Hill, E.K.; Mello, A.J. de; Birrell, H.; Charlwood, J.; Camilleri, P. Steady state and time-resolved fluorescence of 2-aminoacridone sugar derivatives. *J. Chem. Soc., Perkin Trans. 2* **1998**, 2337–2342, doi:10.1039/A806404K.
105. Wang, Y.; Peters, S.; Hammer, M.; Jiang, Y.; Kemerly, T.; Kompella, U.; Srinivas, S. Depth resolved fluorescence lifetime of fluorescein across the cornea. *Investigative Ophthalmology & Visual Science* **2013**, *54*, 2607.
106. Kristoffersen, A.S.; Erga, S.R.; Hamre, B.; Frette, Ø. Testing fluorescence lifetime standards using two-photon excitation and time-domain instrumentation: rhodamine B, coumarin 6 and lucifer yellow. *J. Fluoresc.* **2014**, *24*, 1015–1024, doi:10.1007/s10895-014-1368-1.
107. Przesmycki, R.; Nowosielski, L. USB 3.0 interface in the process of electromagnetic infiltration. In *2016 Progress in Electromagnetic Research Symposium (PIERS).* 2016 Progress in Electromagnetic Research Symposium (PIERS), Shanghai, China, 08–11 Aug. 2016; IEEE, 2016 - 2016; pp 1019–1023, ISBN 978-1-5090-6093-1.
108. Adams, K.E.; Ke, S.; Kwon, S.; Liang, F.; Fan, Z.; Lu, Y.; Hirschi, K.; Mawad, M.E.; Barry, M.A.; Sevick-Muraca, E.M. Comparison of visible and near-infrared wavelength-excitable fluorescent dyes for molecular imaging of cancer. *J. Biomed. Opt.* **2007**, *12*, 24017, doi:10.1117/1.2717137.
109. Li, B.; Yu, Q.; Duan, Y. Fluorescent labels in biosensors for pathogen detection. *Crit. Rev. Biotechnol.* **2015**, *35*, 82–93, doi:10.3109/07388551.2013.804487.

110. Cohen, D.; Dickerson, J.A.; Whitmore, C.D.; Turner, E.H.; Palcic, M.M.; Hindsgaul, O.; Dovichi, N.J. Chemical cytometry: fluorescence-based single-cell analysis. *Annu. Rev. Anal. Chem. (Palo Alto Calif)* **2008**, *1*, 165–190, doi:10.1146/annurev.anchem.1.031207.113104.
111. Myers, F.B.; Lee, L.P. Innovations in optical microfluidic technologies for point-of-care diagnostics. *Lab Chip* **2008**, *8*, 2015–2031, doi:10.1039/B812343H.
112. Haraguchi, T.; Shimi, T.; Koujin, T.; Hashiguchi, N.; Hiraoka, Y. Spectral imaging fluorescence microscopy. *Genes Cells* **2002**, *7*, 881–887, doi:10.1046/j.1365-2443.2002.00575.x.
113. Ma, G.; Fortier, S.; Jean-Jacques, M.; Mincu, N.; Leblond, F.; Ichalalene, Z.; Benyamin-Seeyar, A.; Khayat, M. Fluorescence lifetime estimation of multiple near-infrared dyes in mice. In *Multimodal Biomedical Imaging III.* Biomedical Optics (BiOS) 2008, San Jose, CA, Saturday 19 January 2008; Azar, F.S., Intes, X., Eds.; SPIE, 2008; p 685003.
114. Hanley, Q.S.; Arndt-Jovin, D.J.; Jovin, T.M. Spectrally Resolved Fluorescence Lifetime Imaging Microscopy. *Appl Spectrosc* **2002**, *56*, 155–166, doi:10.1366/0003702021954610.
115. Salthouse, C.D.; Reynolds, F.; Tam, J.M.; Josephson, L.; Mahmood, U. Quantitative Measurement of Protease-Activity with Correction of Probe Delivery and Tissue Absorption Effects. *Sens. Actuators B Chem.* **2009**, *138*, 591–597, doi:10.1016/j.snb.2009.02.037.
116. Raymond, S.B.; Boas, D.A.; Bacskai, B.J.; Kumar, A.T.N. Lifetime-based tomographic multiplexing. *J. Biomed. Opt.* **2010**, *15*, 46011, doi:10.1117/1.3469797.
117. Tolba, M.; Elmansi, H. Studying the quenching resulted from the formation of an association complex between olsalazine or sulfasalazine with acriflavine. *R. Soc. Open Sci.* **2021**, *8*, 210110, doi:10.1098/rsos.210110.
118. Arden-Jacob, J.; Drexhage, K.-H.; Druzhinin, S.I.; Ekimova, M.; Flender, O.; Lenzer, T.; Oum, K.; Scholz, M. Ultrafast photoinduced dynamics of the 3,6-diaminoacridinium derivative ATTO 465 in solution. *Phys. Chem. Chem. Phys.* **2013**, *15*, 1844–1853, doi:10.1039/C2CP43493H.

119. Becker, W.; Bergmann, A.; Koenig, K.; Tirlapur, U. Picosecond fluorescence lifetime microscopy by TCSPC imaging. In *Multiphoton Microscopy in the Biomedical Sciences.* BiOS 2001 The International Symposium on Biomedical Optics, San Jose, CA, Saturday 20 January 2001; Periasamy, A., So, P.T.C., Eds.; SPIE, 2001; p 414.
120. Akers, W.; Lesage, F.; Holten, D.; Achilefu, S. In Vivo Resolution of Multiexponential Decays of Multiple Near-Infrared Molecular Probes by Fluorescence Lifetime-Gated Whole-Body Time-Resolved Diffuse Optical Imaging. *Mol Imaging* **2007**, *6*, 7290.2007.00020, doi:10.2310/7290.2007.00020.
121. Bückers, J.; Wildanger, D.; Vicidomini, G.; Kastrup, L.; Hell, S.W. Simultaneous multi-lifetime multi-color STED imaging for colocalization analyses. *Opt. Express* **2011**, *19*, 3130–3143, doi:10.1364/OE.19.003130.
122. Paszke, A.; Gross, S.; Massa, F.; Lerer, A.; Bradbury, J.; Chanan, G.; Killeen, T.; Lin, Z.; Gimelshein, N.; Antiga, L.; et al. PyTorch: An Imperative Style, High-Performance Deep Learning Library. In *Advances in Neural Information Processing Systems 32*; Wallach, H., Larochelle, H., Beygelzimer, A., Alché-Buc, F.d.\t., Fox, E., Garnett, R., Eds.; Curran Associates, Inc, 2019; pp 8024–8035.
123. Smith, J.T.; Yao, R.; Sinsuebphon, N.; Rudkouskaya, A.; Un, N.; Mazurkiewicz, J.; Barroso, M.; Yan, P.; Intes, X. Fast fit-free analysis of fluorescence lifetime imaging via deep learning. *Proc. Natl. Acad. Sci. U. S. A.* **2019**, *116*, 24019–24030, doi:10.1073/pnas.1912707116.
124. Yao, R.; Ochoa, M.; Intes, X.; Yan, P. Deep compressive macroscopic fluorescence lifetime imaging. In *2018 IEEE 15th International Symposium on Biomedical Imaging (ISBI 2018).* 2018 IEEE 15th International Symposium on Biomedical Imaging (ISBI 2018), Washington, DC, 04–07 Apr. 2018; IEEE, 2018 - 2018; pp 908–911, ISBN 978-1-5386-3636-7.
125. Zhao, Z.-Q.; Zheng, P.; Xu, S.-T.; Wu, X. Object Detection With Deep Learning: A Review. *IEEE Trans. Neural Netw. Learn. Syst.* **2019**, *30*, 3212–3232, doi:10.1109/TNNLS.2018.2876865.
126. Demaret, J.; Varlet, P.; Trauet, J.; Beauvais, D.; Grossemy, A.; Hégo, F.; Yakoub-Agha, I.; Labalette, M. Monitoring CAR T-cells using flow cytometry. *Cytometry B Clin. Cytom.* **2021**, *100*, 218–224, doi:10.1002/cyto.b.21941.

127. Kennedy, D.; Wilkinson, M.G. Application of Flow Cytometry to the Detection of Pathogenic Bacteria. *Curr. Issues Mol. Biol.* **2017**, *23*, 21–38, doi:10.21775/cimb.023.021.
128. He, G.; Xu, D.; Qin, H.; Yang, S.; Xing, D. In vivo cell characteristic extraction and identification by photoacoustic flow cytography. *Biomed. Opt. Express* **2015**, *6*, 3748–3756, doi:10.1364/BOE.6.003748.
129. Tan, X.; Patil, R.; Bartosik, P.; Runnels, J.M.; Lin, C.P.; Niedre, M. In Vivo Flow Cytometry of Extremely Rare Circulating Cells. *Sci. Rep.* **2019**, *9*, 3366, doi:10.1038/s41598-019-40143-2.
130. Goddard, G.; Martin, J.C.; Naivar, M.; Goodwin, P.M.; Graves, S.W.; Habbersett, R.; Nolan, J.P.; Jett, J.H. Single particle high resolution spectral analysis flow cytometry. *Cytometry A* **2006**, *69*, 842–851, doi:10.1002/cyto.a.20320.
131. Mosiman, V.L.; Patterson, B.K.; Canterero, L.; Goolsby, C.L. Reducing cellular autofluorescence in flow cytometry: An in situ method. *Cytometry* **1997**, *30*, 151–156, doi:10.1002/(SICI)1097-0320(19970615)30:3<151:AID-CYTO6>3.0.CO;2-O.
132. Corsetti, J.P.; Sotirchos, S.V.; Cox, C.; Cowles, J.W.; Leary, J.F.; Blumburg, N. Correction of cellular autofluorescence in flow cytometry by mathematical modeling of cellular fluorescence. *Cytometry* **1988**, *9*, 539–547, doi:10.1002/cyto.990090606.
133. Steinkamp, J.A.; Crissman, H.A. Resolution of fluorescence signals from cells labeled with fluorochromes having different lifetimes by phase-sensitive flow cytometry. *Cytometry* **1993**, *14*, 210–216, doi:10.1002/cyto.990140214.
134. Gong, Y.; Fan, N.; Yang, X.; Peng, B.; Jiang, H. New advances in microfluidic flow cytometry. *Electrophoresis* **2018**, doi:10.1002/elps.201800298.
135. van der Pol, E.; Sturk, A.; van Leeuwen, T.; Nieuwland, R.; Coumans, F. Standardization of extracellular vesicle measurements by flow cytometry through vesicle diameter approximation. *J. Thromb. Haemost.* **2018**, *16*, 1236–1245, doi:10.1111/jth.14009.
136. Huh, D.; Gu, W.; Kamotani, Y.; Grotberg, J.B.; Takayama, S. Microfluidics for flow cytometric analysis of cells and particles. *Physiol. Meas.* **2005**, *26*, R73-98, doi:10.1088/0967-3334/26/3/R02.

137. Cossarizza, A.; Chang, H.-D.; Radbruch, A.; Acs, A.; Adam, D.; Adam-Klages, S.; Agace, W.W.; Aghaeepour, N.; Akdis, M.; Allez, M.; et al. Guidelines for the use of flow cytometry and cell sorting in immunological studies (second edition). *Eur. J. Immunol.* **2019**, *49*, 1457–1973, doi:10.1002/eji.201970107.
138. Tuchin, V.V.; Tárnok, A.; Zharov, V.P. In vivo flow cytometry: a horizon of opportunities. *Cytometry A* **2011**, *79*, 737–745, doi:10.1002/cyto.a.21143.

List of Abbreviations

Abbreviation	Meaning
ADC	Analog to digital converter
Ag	Antigen detection
ANN	Artificial neural networks
CMOS	Complementary metal–oxide–semiconductor
DCR	Dark count rate
DIG	Digoxigenin
ELISA	Enzyme-linked immunosorbent assay
FF	Fill factor
FL	Fluorescence lifetime
FLIM	Fluorescence lifetime imaging microscopy
FPGA	Field programmable gate array
HRP	Horseradish peroxidase
LiDAR	Light detection and ranging
LOD	Limit of detection

LS	Weighted nonlinear least square
MSELoss	Mean square error loss function
PBST	Phosphate buffer saline tween
PCB	Printed circuit board
PDMS	Polydimethylsiloxane
PEEK	Polyether ether ketone
PMT	Photo multiplier tube
PoC	Point-of-care
PS	Polystyrene
RDT	Rapid diagnostic tests
ReLU	Rectified linear unit
RNA	Ribonucleic acid
RT-PCR	Reverse transcription polymerase chain reaction
SARS-CoV-2	Severe acute respiratory syndrome coronavirus 2
SPAD	Single photon avalanche diode
SSC	Saline-sodium citrate
ssDNA	Single strand deoxyribonucleic acid
TAC	Time to analog converter
TCSPC	Time-correlated single-photon counting
TDC	Time to digital converter
WHO	World health organization

Formula Symbol

Latin characters

Symbol	Unit	Meaning
$< N_{\mathrm{c}} >_{\mathrm{w}}$	-	Mean photon counts per measurement cycle
A_{K}	m^2	Spherical area
A_{O}	m^2	Area of the spherical segment
b	m	Diameter
c	M	Concentration
c_{v}	-	Precision of FL acquisition
d	m	Distance
d_{Pixel}	m	Pixel diameter
d_{rate}	bit/s	Data readout rate
f	-	Percentage of emitted photons from the fluorophore
h	m	Height
I	-	Intensity
LOD	copies/ml	Limit of detection
N_{c}	-	Photon counts
N_{Pixel}	-	Number of pixel
n_{w}	-	Number of measurement cycles
P	-	Fractional contribution
r	m	Radius
t	s	Time
t_{res}	s	Time resolution

t_{w}	s	Measurement duration of one cycle
V_{ex}	V	Excess-bias voltage
Z'	-	Quantitative value for separation of two distributions

Greek characters

Symbol	Unit	Meaning
α	-	Pre-exponential factor
$\Delta\tau$	ns	Difference between two fluorescence lifetimes
$\delta\tau$	-	Accuracy of FL acquisition
σ	ns	Standard deviation
τ	s	Fluorescence lifetime

Appendix

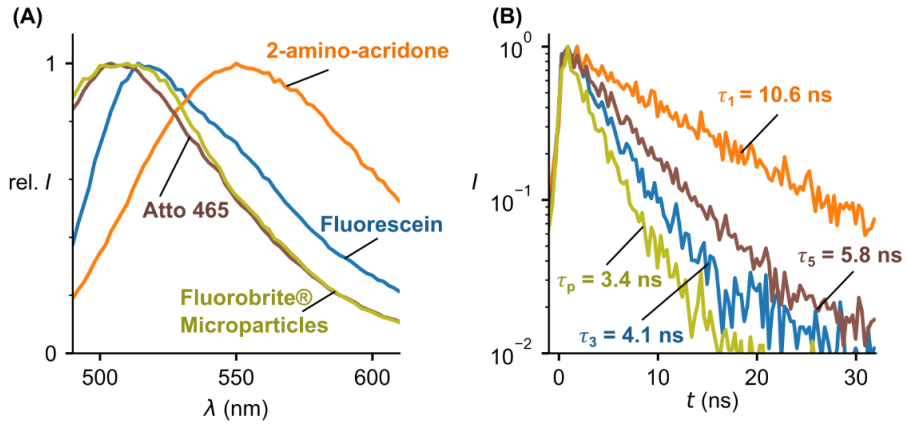

Figure A.1: Differentiation of particles. (A) Spectral differentiation of particles using optical filters is not possible due to the superposition of spectra. **(B)** Differentiation of particles is possible because of different FLs.

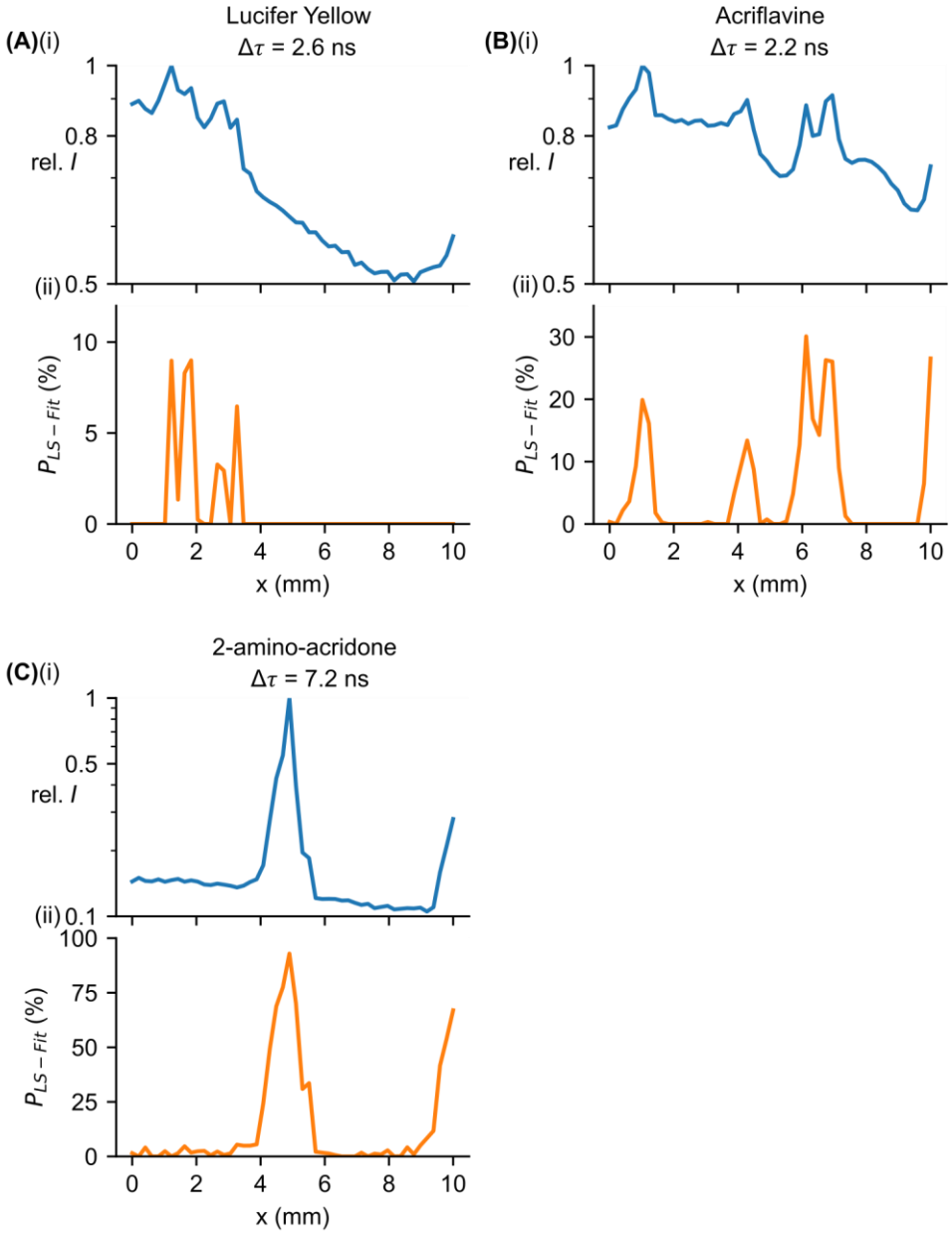

Figure A.2: Differentiation of microparticles with fluorescent background. Microparticles are in a solution containing a fluorophore (**(A)** lucifer yellow, **(B)** acriflavine and **(C)** 2-amino-acridone) with a fluctuating (i) fluorescence intensity. Determination of the (ii) fractional contribution of the microparticles allows for intensity-independent differentiation.

List of Figures

List of Tables

Conferences and Publications

Published:

- Netaev, A.; Karaduman, B.D.; Sheikh, M.A.; Schierbaum, N.; Seidl, K., “pH-and oxygen sensors based on fluorescent nanoparticles for Lab-on-Chip applications.” *Biomedical Engineering / Biomedizinische Technik* **2020**, *65*, 296–300, doi:10.1515/bmt-2020-6051.

- Netaev, A.; Karaduman, B.D.; Sheikh, M.A.; Schierbaum, N.; Seidl, K. “Single photon avalanche diode (SPAD)-based sensor system for measuring the fluorescence lifetime of functionalized silica-nanoparticles.” *Mikro-Nano-Integration - 8. GMM-Workshops* **2020**.

- Netaev, A.; Schierbaum, N.; Seidl, K. “Advantages and Limitations of Fluorescence Lifetime Measurements Using Single-Photon Avalanche Diode (SPAD) Array Detector: A Comprehensive Theoretical and Experimental Study.” *MDPI Sensors* **2022**

Submitted:

- Netaev, A.; Schierbaum, N.; Seidl, K. “Artificial neural network (ANN)-based determination of fractional contributions from mixed fluorophores using fluorescence lifetime measurements.” *Journal of Fluorescence* **2023**

Danksagung

An erster Stelle möchte ich mich bei Prof. Dr. Karsten Seidl bedanken. Seinem großen Engagement ist es zu verdanken, dass ich meine Dissertation am Fraunhofer IMS absolvieren konnte. Mein Dank gilt auch Prof. Dr. Sven Ingebrandt, der freundlicherweise das Zweitgutachtens übernommen hat. Ein besonderer Dank geht an Nicolas Schierbaum für seine hervorragende Betreuung. Durch seine fachkundigen Ratschläge war es mir möglich, eine strukturierte und nachvollziehbare wissenschaftliche Arbeitsweise zu erlernen und diese in meiner Dissertation anzuwenden.
Meinen Kollegen aus der ehemaligen MNS-Arbeitsgruppe, der BMS-Arbeitsgruppe und auch der OS-Arbeitsgruppe danke ich für den wissenschaftlichen Diskurs, der hilfreichen Ratschläge und das angenehme Arbeitsklima. Mein Dank gilt auch den Absolventen Eric Guthmann, Mohammed Ali Sheikh, Birvan Dogan Karaduman und Stefan Krüger für die Durchführung ihrer Abschlussarbeiten.
Aus tiefstem Herzen danke ich meiner Mutter Vinera Netaeva. Von ihr lernte ich den Einblick in die Naturwissenschaften und die damit verbundene Neugierde. Mein besonderer Dank gebührt meiner Freundin Han-Tung Wu, die mir während dieser schwierigen Reise zur Seite stand und mir immer den Rücken freihielt.

DOI: 10.17185/duepublico/77455
URN: urn:nbn:de:hbz:465-20230504-140125-7